

NOV 13 1990

Arthur D Little

**A Novel GaAs-
Based IR Detector**

Phase I

CONFIDENTIAL AND PROPRIETARY
ARDEC DIVISION

**Final Report to
U.S. Army Research,
Development and
Engineering Command
(ARDEC)
Picatinny Arsenal,
New Jersey 07806-5000**

**Contract No.
DAAA21-88-C-0215**

Project No. BAA ARDEC 87-5

November 8, 1990

APPROVED FOR PUBLIC RELEASE;
DISTRIBUTION UNLIMITED.

19960126 006

DTIC QUALITY INSPECTED 1

Arthur D. Little, Inc.
Acorn Park
Cambridge, Massachusetts
02140-2390

Reference 62409

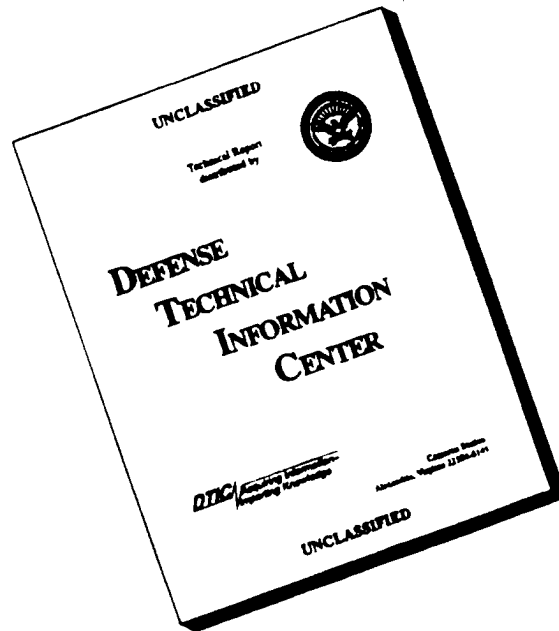
0180,000

19960126 006

**PER PATRICIA AYS AT ARMY RESEARCH,
DEVELOPMENT AND ENGINEERING COMMAND
(ARDEC) PICATINNY ARSENAL, NEW JERSEY.
HER COPY IS ALSO MISSING PAGES 3-12 & 3-20
AND WE WILL NOT BE ABLE TO GET THEM
BECAUSE OF LACK OF FUNDS AND CLOSURE
OF CONTRACT.**

FEBRUARY 22, 1996

DISCLAIMER NOTICE



**THIS DOCUMENT IS BEST
QUALITY AVAILABLE. THE
COPY FURNISHED TO DTIC
CONTAINED A SIGNIFICANT
NUMBER OF PAGES WHICH DO
NOT REPRODUCE LEGIBLY.**

A NOVEL GaAs-BASED IR DETECTOR

FINAL REPORT
Phase-I

November 1, 1990

Submitted to
U.S. Army Research, Development and Engineering Command
[ARDEC]
Picatinny Arsenal, NJ 07806-5000

Contract No. DAAA21-88-C-0215
Project No. BAA ARDEC 87-5

By

Arthur D. Little, Inc.
Acorn Park, Cambridge, MA 02140

62409

MATERIAL INSPECTION AND RECEIVING REPORT		1. PROC. INSTRUMENT IDEN (CONTRACT) DAAA21-88-C-0215		5. INVOICE NO. 0 DATE		PAGE 1 1 ACCEPTANCE POINT	
2. SHIPMENT NO. 0001Z		3. DATE SHIPPED NOV 8 1990		4. B/L MAIL		6. DISCOUNT TERMS N/A	
9. PRIME CONTRACTOR CODE 75629 Arthur D. Little, Inc. Acorn Park Cambridge, MA 02140-2390				10. ADMINISTERED BY CODE DCMAO/Boston 495 Summer Street Boston, MA 02110-2138			
11. SHIPPED FROM (OF OR BY) CODE See Block 9				12. PAYMENT WILL BE MADE BY CODE DCASR/Boston 495 Summer Street Boston, MA 02110-2184			
13. SHIPPED TO CODE Commander US Army Armament Research Development & Engineering Center (ARDEC) Picatinny Arsenal, NJ 07806-5000				14. MARKED FOR CODE			
15. ITEM NO.	16. STOCK/PART NO. <small>(Indicate number of shipping containers - type of container - container number)</small>	17. DESCRIPTION		18. QUANTITY SHIP'D/REC'D*	19. UNIT	20. UNIT PRICE	21. AMOUNT
		Design, fabricate and test a GaAs Based Infra-Red Detector - FINAL REPORT/PHASE I -					
22. PROCUREMENT QUALITY ASSURANCE <div style="display: flex; justify-content: space-between;"> <div style="width: 45%;"> <input type="checkbox"/> POA <input type="checkbox"/> ACCEPTANCE of listed items has been made by me or under my supervision and they conform to contract, except as noted herein or on supporting documents. DATE _____ SIGNATURE OF AUTH GOVT REP _____ TYPED NAME AND OFFICE _____ </div> <div style="width: 45%;"> <input type="checkbox"/> POA <input type="checkbox"/> ACCEPTANCE of listed items has been made by me or under my supervision and they conform to contract, except as noted herein or on supporting documents. DATE _____ SIGNATURE OF AUTH GOVT REP _____ TYPED NAME AND TITLE _____ </div> </div>				23. RECEIVER'S USE Quantities shown in column 17 were received in apparent good condition except as noted. DATE RECEIVED _____ SIGNATURE OF AUTH GOVT REP _____ TYPED NAME AND OFFICE _____ <small>*If quantity received by the Government is the same as quantity shipped, indicate by (X) mark. If different, enter actual quantity received below quantity shipped and encircle.</small>			
24. CONTRACTOR USE ONLY							

Table of Contents

		<u>page</u>
1.0	Executive Summary	1-1
1.1	Program Status	1-1
1.2	Program Achievements	1-2
1.3	Conclusions	1-7
2.0	Measurements and Device Design	2-1
2.1	Optical Measurements	2-1
2.1.1	Absorption Measurements	2-1
2.1.1.1	Single Pass Measurement	2-4
2.1.1.2	Multipass Edge Insertion Measurement	2-4
2.1.1.3	Multipass Face Insertion Measurement	2-10
2.2	Electrical Measurements	2-16
2.2.1	Methodology	2-16
2.2.2	Noise Measurement of EG&G HgCdTe Detector and PA-100 Voltage Preamplifier	2-26
2.3	Device Design	2-28
2.3.1	Excitation to Band Edge	2-31
2.3.2	Excitation to a Resonant State	2-32
2.4	Coupler (Transformer) Design	2-33
3.0	Optical and Electrical Characterizations of the Quantum Well Detectors	3-1

List of Figures

<u>Figure No.</u>	<u>page</u>
1.1	1-4
1.2	1-5
1.3	1-6
1.4	1-8
2.1	2-2
2.2	2-3
2.3	2-5
2.4	2-6
2.5	2-7
2.6	2-8
2.7	2-9
2.8	2-11
2.9a	2-12
2.9b	2-13
2.9c	2-14
2.9d	2-15
2.9e	2-16
2.10	2-18
2.11a	2-20
2.11b	2-21
2.12a	2-22
2.12b	2-23
2.13	2.24
2.14	2.25
2.16	2.31
2.17	2-31
2.18	
2.19	2-38
2.20	2-41
2.21	2-44
2.22	2-47
3.1	3-2
3.2	3-3
3.3	3-4
3.4	3-6
3.5	3-7
3.6	3-8

3.7	Absorbance Calculated from p-s Polarizations for Sample #890901	3-9
3.8a,b	Absorbance for p and s Polarizations for Sample #890915	3-10
3.8c	Absorbance Calculated from p-s Polarizations for Sample #890915	3-11
3.9a	Absorbance Spectra for Sample #890920	3-13
3.9b	Absorbance Spectra for Sample #890920	3-14
3.9c	Absorbance Spectra for Sample #890920	3-15
3.10	Photoconductivity Observed with He-Ne Laser at $f=1000\text{Hz}$ Chopping on #890915	3-16
3.11	Photoconductivity Observed through a Si Filter which Rules Out Across The Gap Photoconduction	3-18
3.12	Output on mV Versus Chopping Frequency	3-19
3.13abc	Voltage Output Versus Frequency Observed on #890920	3-20
3.13def	Voltage Output Versus Frequency Observed on #890920	3-21
3.13g	Voltage Output Versus Frequency Observed on #890920	3-22
3.14	Output in mV Versus Chopping Frequency with Different Filters for #890920	3-23
3.15	Output in V Versus Chopping Frequency with for HgCdTe Detector,	3-24
3.16a-c	Modulated Output Versus Bias Current for #890920	3-25-26
3.17	Modulated Output Versus Bias Current for #890920	3-27
3.18	Transmission Characteristics of The High Pass Filter Used on Detectivity Measurement	3-29
3.19	Modulated Output with And Without Filter	3-30-31
3.20	Approximately Equal s and p Responses	3-31
3.21-3.28	Various Modulated Output	3-34-36
3.29	p-Polarization Response for #890921	3-37
3.30	s-Polarization Response for #890921	3-37
3.31	p-s Response Difference for #890921	3-38

Glossary of Terms

EFF	Equivalent fill factor
FPA	Focal-plane-array
FPE	Fabry-Perot etalon
FTIR	Fourier-transform infrared..
GaAs	Gallium-Arsenide
HCT	Mercury-Cadmium-Telluride (HgCdTe)
MQW	Multi-quantum-well
MLD	Multilayer dielectric
NEP	Noise equivalent power
p-polatization	Polarized in the plane-of-incidence
QW	Quantum-well
s-polarization	Polarized normal (senchrecht) to the plane of incidence

1.0 Executive Summary

Under Contract to the U.S. Army ARDEC, Arthur D. Little, Inc. undertook a two phased program to first design, fabricate, and characterize a single element, GaAs based, quantum-well infrared detector to operate at 10 μm and, later, to implement a 2 by 2 focal plane array prototype.

This is the final report for the first phase of this program, the object of which is to fabricate and evaluate demonstrate a single element detector.

1.1 Program Status

The objective of the first program was to produce an optimized style element detector. While the device was demonstrated, there was not enough time for optimization: Funding for the Phase II of this program was not available and Arthur D. Little decided to continue the program with internal funds towards optimization until further funds could be found to continue with the program.

During the development stage of the device, two new schemes were identified and developed to enhance the coupling of the IR photon to the device cavity. This is an area on which other groups working on similar structures have utilized either simple solutions that do not lend themselves to focal-plane array (FPA) implementation or techniques which are alien to GaAs semiconductor processing technology.

Within a detector which works with quantum-well (QW) confined electrons, optical absorption takes place only when the electric polarization vector of the incoming photon has a significant component perpendicular to the quantum-well i.e., the surface of the substrate. This means that the photons have to be introduced at a large angle of incidence which is a serious disadvantage because it renders impossible the placement of all the elements of the FPA on one monolithic GaAs substrate.

In order to solve this problem, firstly we chose to place the quantum-wells within a Fabry-Perot etalon (FPE). This means that, through an effective wave-guiding action, photons make many passes through the QW's improving the quantum efficiency. The reflectors of the FPE were designed as multilayer dielectric (MLD) reflectors. (We used "rugates," smoothly varying index single crystal structures we have developed on behalf of the Air Force.)

Secondly, in order to allow normal incidence (actually $F=1$ optics was assumed as the working configuration), the devices were designed to be under faceted pyramids which bent the light rays into the device.

Our accomplishments included the following:

1. Fabrication of rugate-cladded multi - quantum well structures,
2. Observation of optical absorption with edge insertion by means of [FTIR] spectrometry,
3. Observation of enhanced optical absorption with rugate cladding and face insertion,
4. Observation of photoconductivity,
5. Development of the transformer concept, theory, and design principles,
6. Demonstration of transformer fabrication process,

1.2 Program Achievements

By September 1, 1989, the official end of the Phase I, our samples were consistently too conductive, giving rise to high dark currents. Since then, we identified the cause of this phenomenon and rectified it.

At the end of Phase I we reported a detectivity of $1.43 \times 10^4 \text{ cm}\sqrt{\text{Hz/W}}$ which could not be repeated. Since then we fabricated a second batch of devices on which we repeatably observed an estimated detectivity of $2.79 \times 10^6 \text{ cm}\sqrt{\text{Hz/W}}$. Although this is 3600 times less than what was reported by Levine et al. at $8.2 \text{ }\mu\text{m}$, we are confident that when we include all

our design improvements, we will reach the optimal value. (We should also point out that 8.2 μm and 10 μm performances could not be compared directly.)

We have been working on two different device configurations:

1. Devices for edge insertion (Fig. 1.1)
2. Devices with rugates for face insertion. (Fig. 1.2)

The first type of device configuration is the only one upon which we have evaluated electrical performance. These devices are somewhat lossy because the inserted light gets absorbed by the thick, doped substrate and that portion which is not impinging on the undoped portion is expected to be absorbed.

The second type of devices were evaluated only for their optical absorption. The experiment designed for this purpose can be immediately appreciated by observing Fig. 1.3. Here the transmission data for light impingement at various angles of incident on an FTIR is shown. Since the peaks of the rugates shift equally for S and P polarization, a peak in the difference spectrum which does not coincide with the rugate peaks shows absorption due to the QW structure. One also observes that the absorption is a maximum for the Brewster's angle, as expected.

Face insertion configuration shown in Fig. 1.2 is unique to our design. This concept, coupled with faceted pyramids etched into the substrate, allow

1. Enhanced coupling efficiency
2. Near normal face insertion.

PROTOTYPE DEVICE FOR EDGE INSERTION

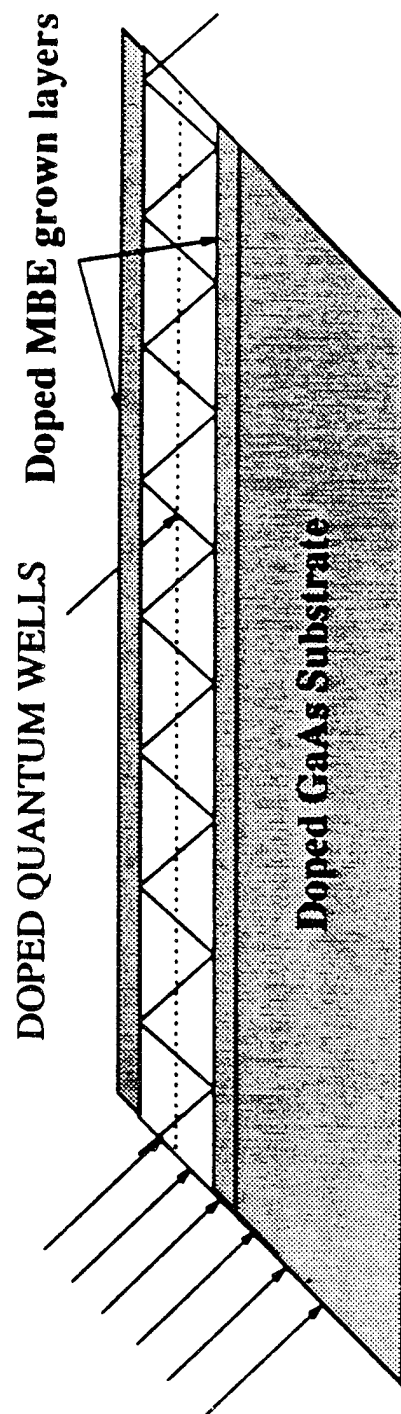


Fig. 1.1.1 Prototype Device for Edge Insertion

PROTOTYPE DEVICE FOR FACE INSERTION

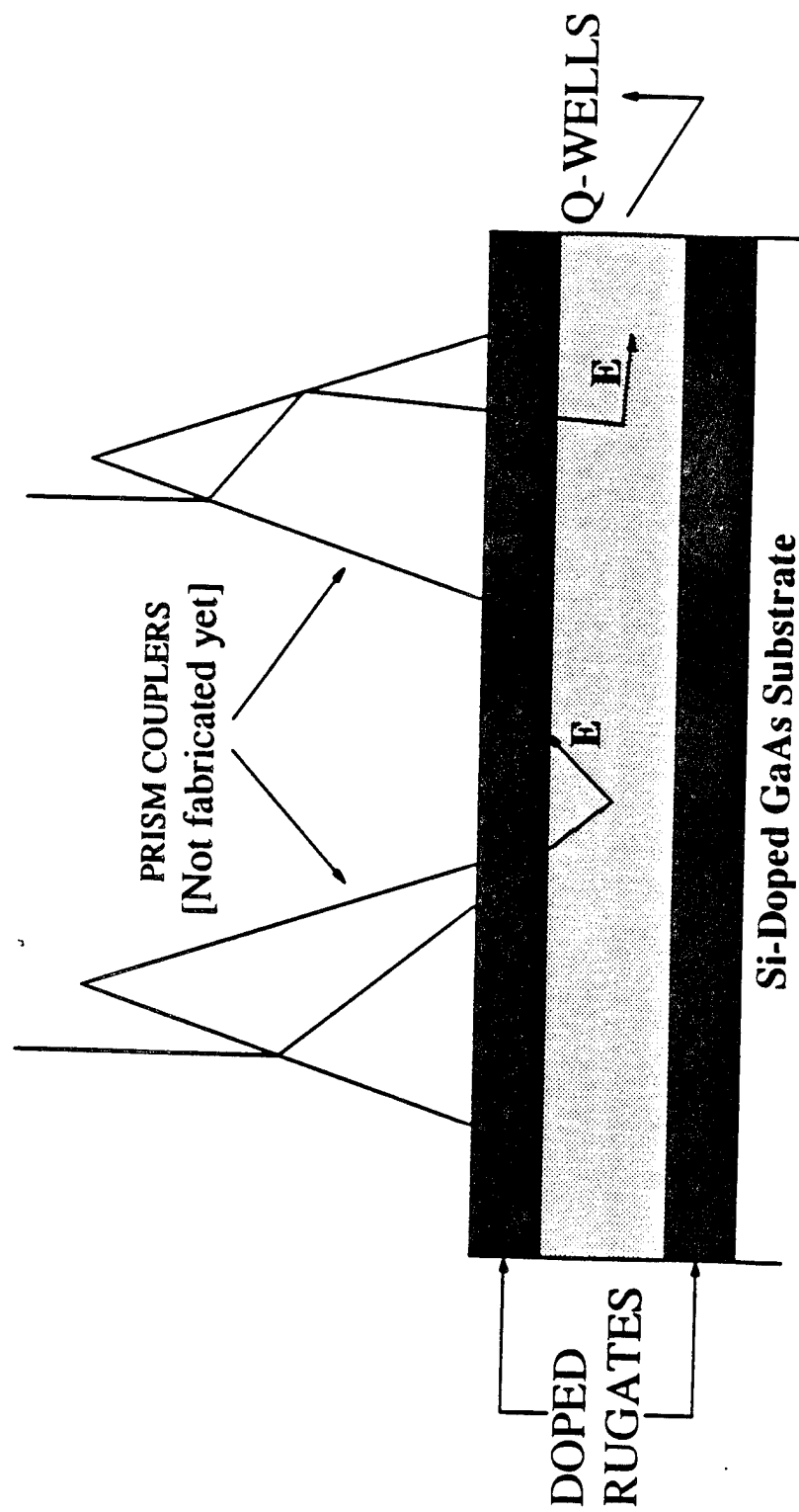
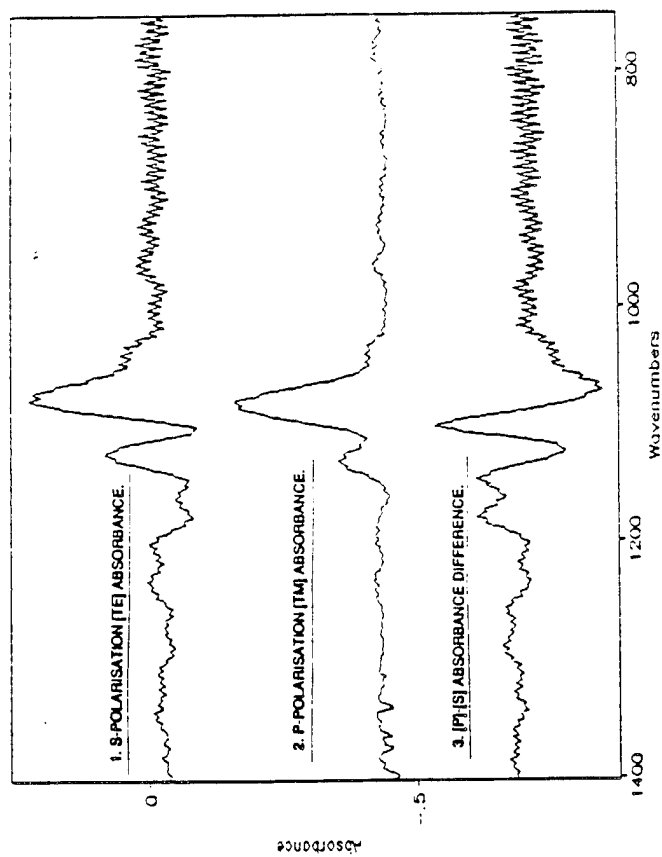


Fig. 1.2 Prototype Device for Face Insertion

ABSORBANCE AS A FUNCTION OF ANGLE AND POLARISATION WITH FACE INSERTION IN FABRY-PEROT CONFIGURATION.

METHOD: FTIR SPECTROSCOPY. [Continued]



1. S-POLARISATION [TE] ABSORBANCE.
2. P-POLARISATION [TM] ABSORBANCE.
3. [P]-[S] ABSORBANCE DIFFERENCE.

Fig. 1.3 Absorbance As A Function of Angle and Polarization

In preparation for the fabrication of the second configuration, we have completed the calculation of the coupling efficiency. This is discussed under the subject of transformer design. In the experimental side, we developed the capability to etch 45° pyramids using a sulfuric acid etch (Figure 1.4).

In the areas of electrical characterization, we established procedures for and performed responsivity, electrical noise, and baseline detectivity in a commercial HgCdTe detector.

At present we are getting ready for the third iteration for device optimization process.

1.3 Conclusions

An algorithm for designing quantum-wells has been prepared, coded, and tested.

The theory for the coupling of photons to the device with near normal insertion by means of optical transformers has been developed results are fabricated.

Two iterations on devices with edge insertion have been accomplished and a detectivity of $2.79 \cdot 10^6 \text{ cm}\sqrt{\text{Hz/W}}$ has been observed.

A third iteration to reach a detectivity of order of magnitude of $10^{10} \text{ cm}\sqrt{\text{Hz/W}}$ is being implemented.

An FP configuration for our detector is also being developed.

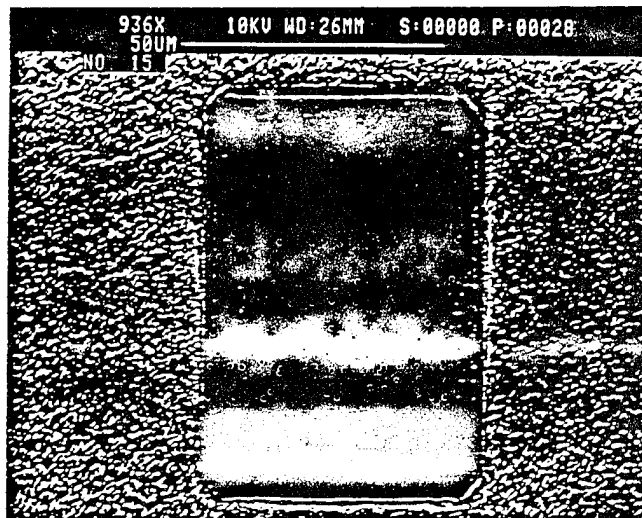


Fig. 1.4 Etched Beveled Pyramid Structure

2.0 Measurements and Device Design

Two kind of measurements were carried out: optical and electrical.

The optical measurements involved: absorption and response. The electrical measurements included material characterization, noise measurements and, of course, responsivity (detectivity) measurements.

2.1 Optical Measurements

We will start with the optical absorption measurements.

2.1.1 Absorption Measurements

Our experimental procedure to detect unambiguously the absorption of the quantum wells involves two independent techniques. These differ in the manner that light is inserted into the cavity. They involve using samples both sides of which have been polished, with:

1. 45° degree beveled edges employed in the edge-insertion configuration (Fig. 2.1), or
2. parallel faces employed in the face-insertion configuration at Brewster angle (Fig. 2.2).

In the second type of samples, the quantum-well collection is placed in between two multilayer dielectric reflectors grown monolithically on the substrate. The two types are similar except for the dielectric reflectors. This is because in the edge insertion, if there is a Fabry-Perot etalon near the top surface, only a small portion of the edge inserted light actually goes into the etalon.

PROTOTYPE DEVICE FOR EDGE INSERTION

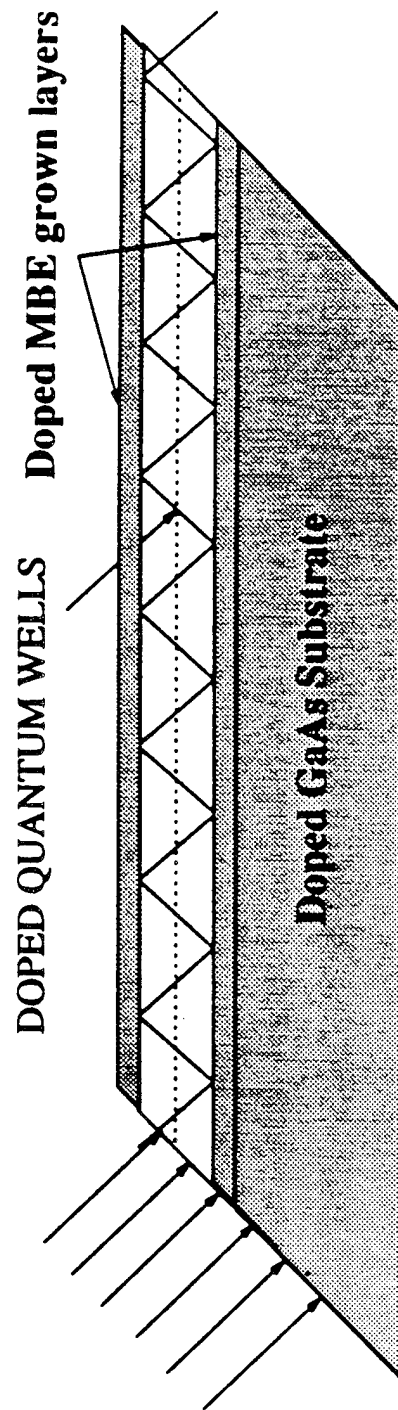


Fig. 2.1 Prototype Device for Edge Insertion

PROTOTYPE DEVICE FOR FACE INSERTION

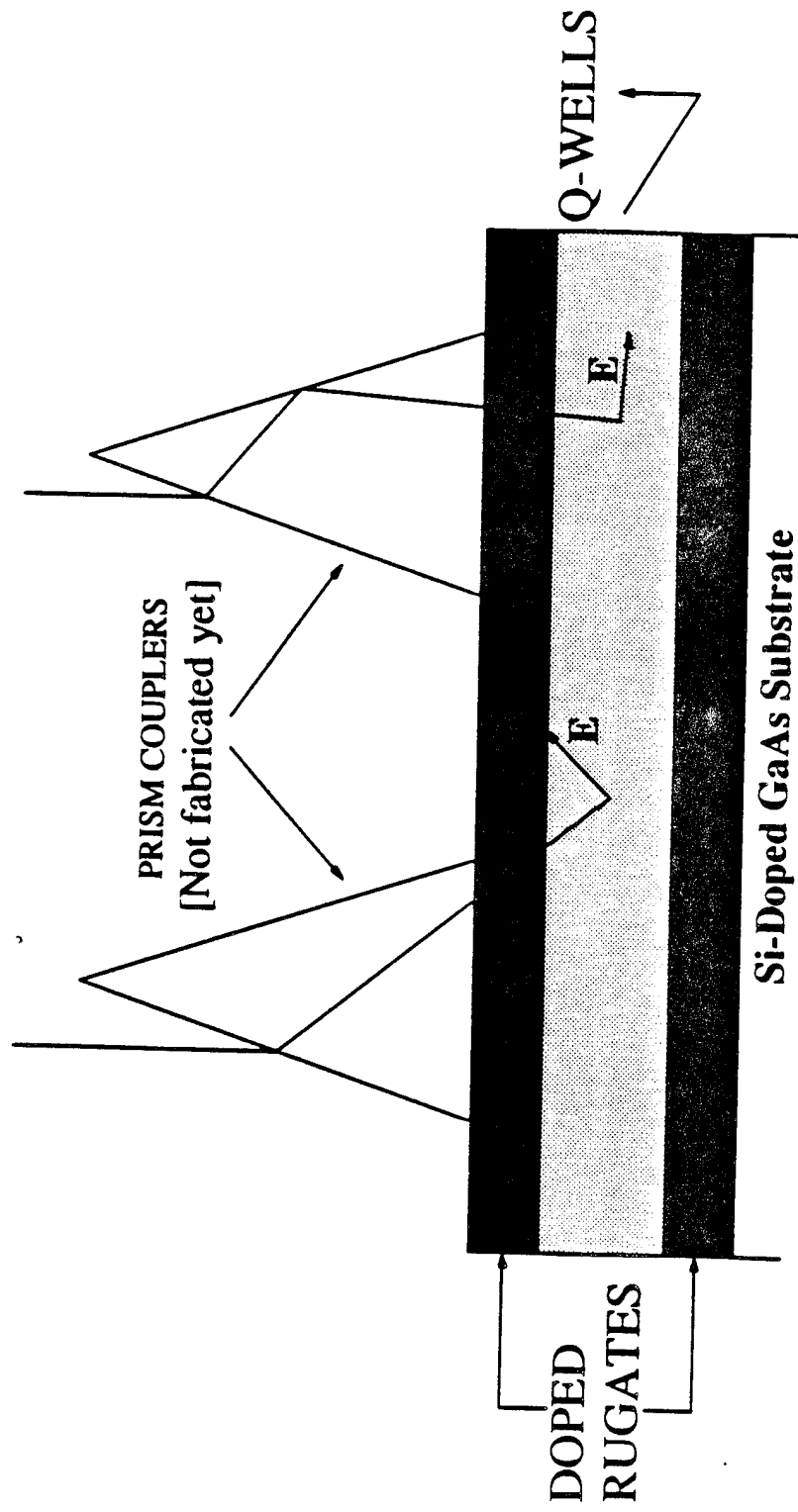


Fig. 2.2 Prototype Device for Face Insertion

2.1.1.1 Single Pass Measurement

In the single-pass configuration the absorption is quite weak. Fig. 2.3 shows the normal incidence (0°) data wherein the difference spectrum between the p- and s-polarizations is without any peaks. Figs. 2.4 and 2.5 show the spectra associated with 45° and 73° angles of incidence, respectively. The difference spectrum at 73° displays the most pronounced peaks in good agreement with the placement of the edge insertion peaks.

2.1.1.2 Multipass Edge Insertion Measurement

A typical measurement of this type was carried out on a beveled sample with a Fourier transform IR spectrometer. The measurement geometry is shown in Fig. 2.6.

The IR beam was polarized by means of a wire grid polarizer built on a ZnS window. Two measurements were performed: signal polarized in the plane of incidence (quantum-well absorption is possible if k is not normal to the QW-plane), signal polarized perpendicular to the plane of incidence (the polarization vector is in the plane of QW for all angles of incidence). The first case, simply referred to as the p-polarization, absorption is expected except only for nonvanishing angles of incidence. For the s(senkrecht)-polarization, absorption is not possible. By taking transmission spectra with p- and s-polarization with $\theta = 45$ and forming a ratio at the former to latter, we expect to remove the material related structure and leave only the QW absorption.

Figure 2.7 shows this spectrum. The broad peak centered around 850 cm^{-1} represents the absorption of the quantum well. The well designed for absorption at $10\text{ }\mu\text{m}$, absorbed at $11.8\text{ }\mu\text{m}$, some 18% off from the design wavelength.

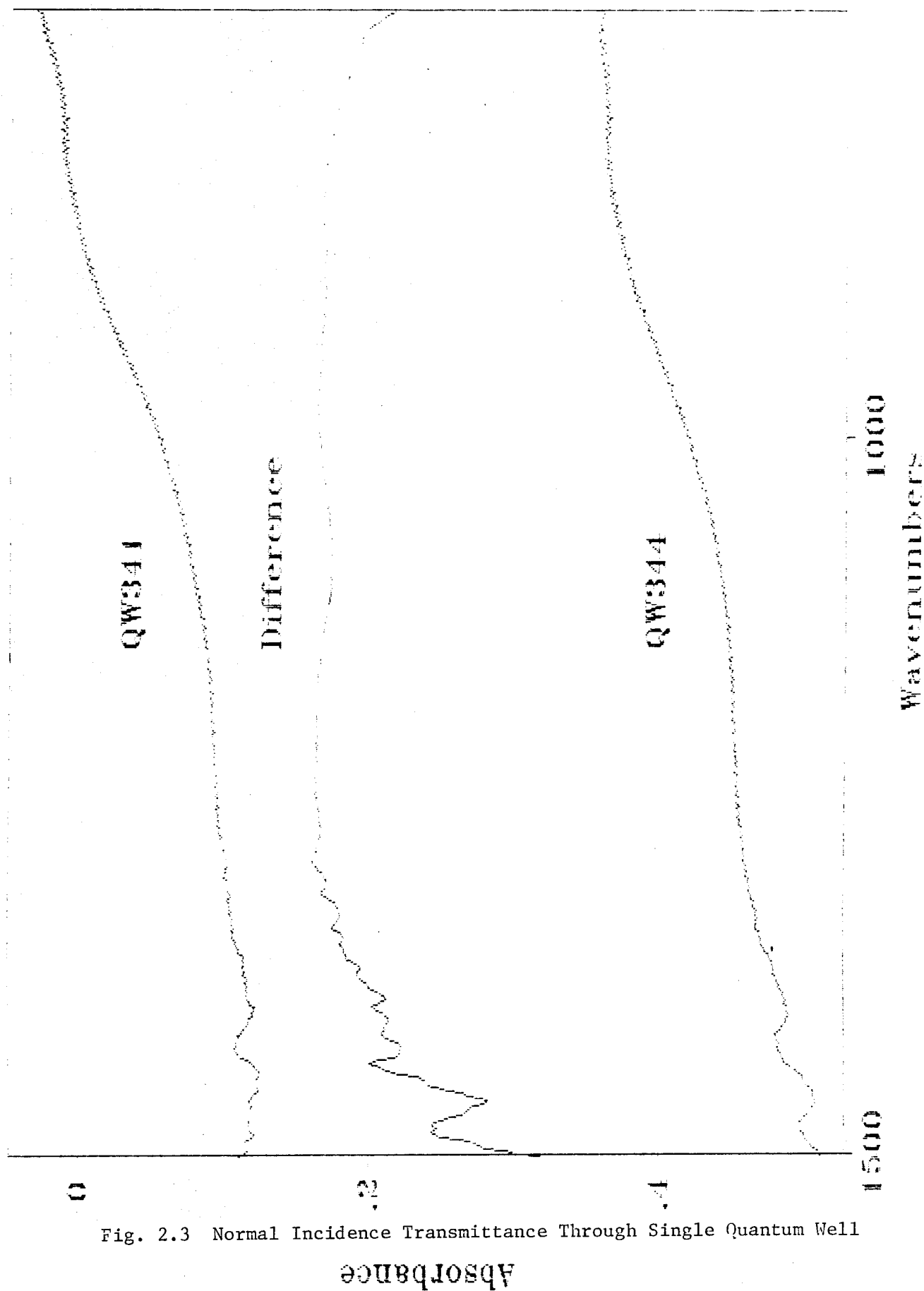


Fig. 2.3 Normal Incidence Transmittance Through Single Quantum Well

QW341 Res = 4.0 cm⁻¹ 07/26/89 10:33

All spectra are smoothed (Savitsky-Golay 25)

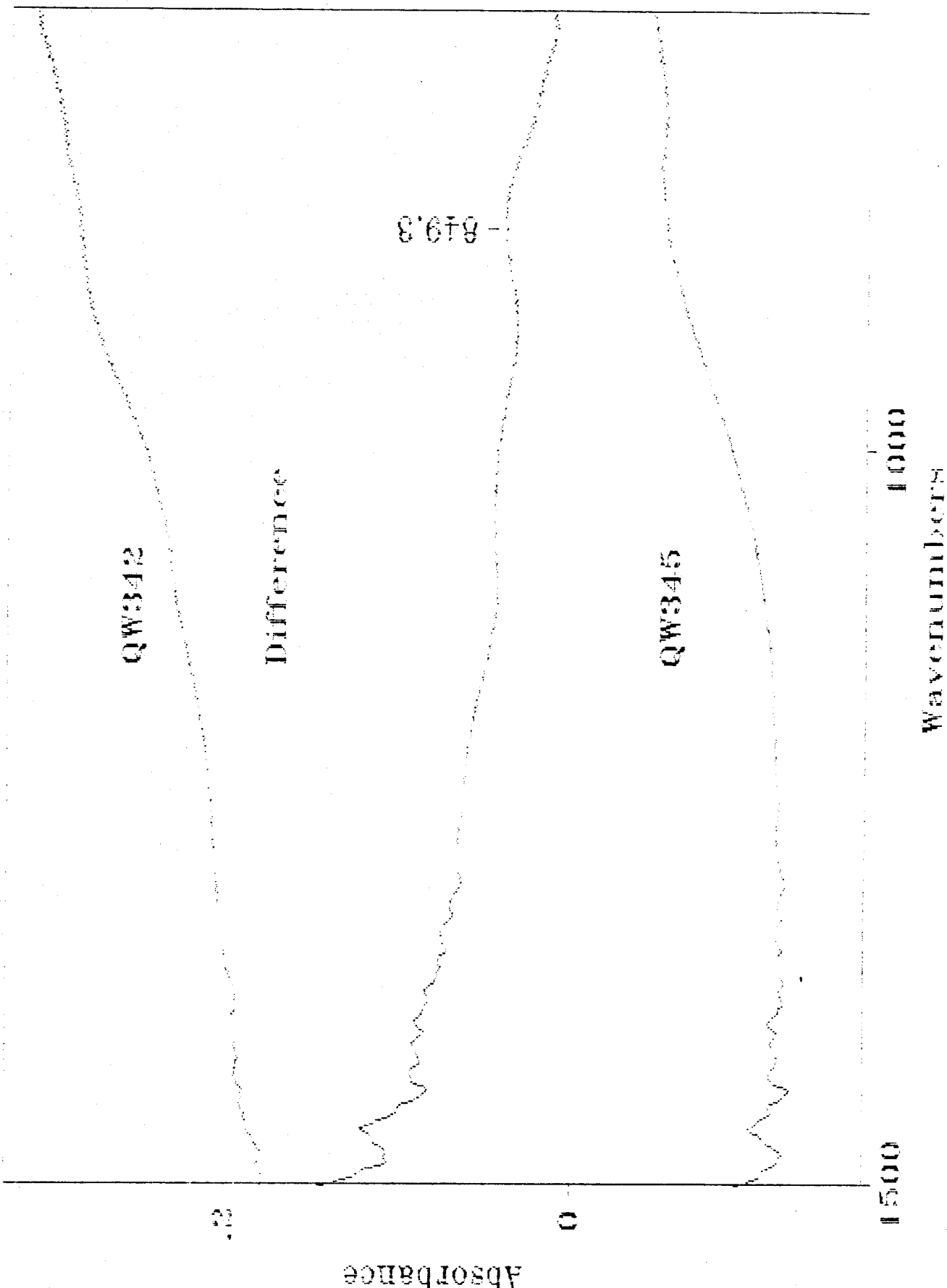


Fig. 2.4 $\theta = 45$ Incidence Transmittance

QW345 Res= 4.0 cm-1 07/26/89 10:39
 All spectra are smoothed (Savitsky-Golay 25)
 Fig. 3

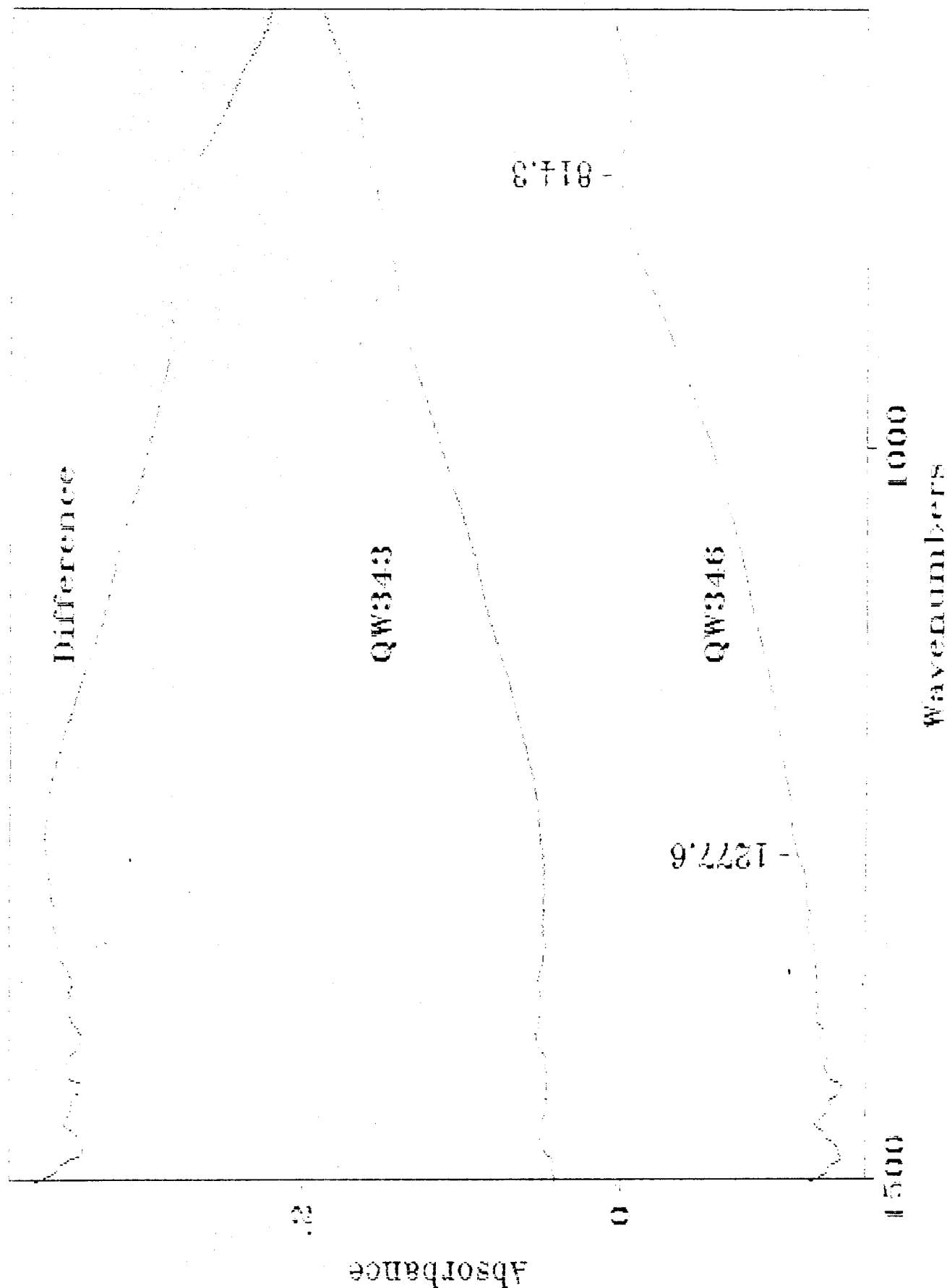


Fig. 2.5 $\theta = 73$ Incidence Transmittance

QW346 Res = 4.0 cm-1 07/26/89 10:29

All spectra are smoothed (Savitsky-Golay 25)

Fig. 4

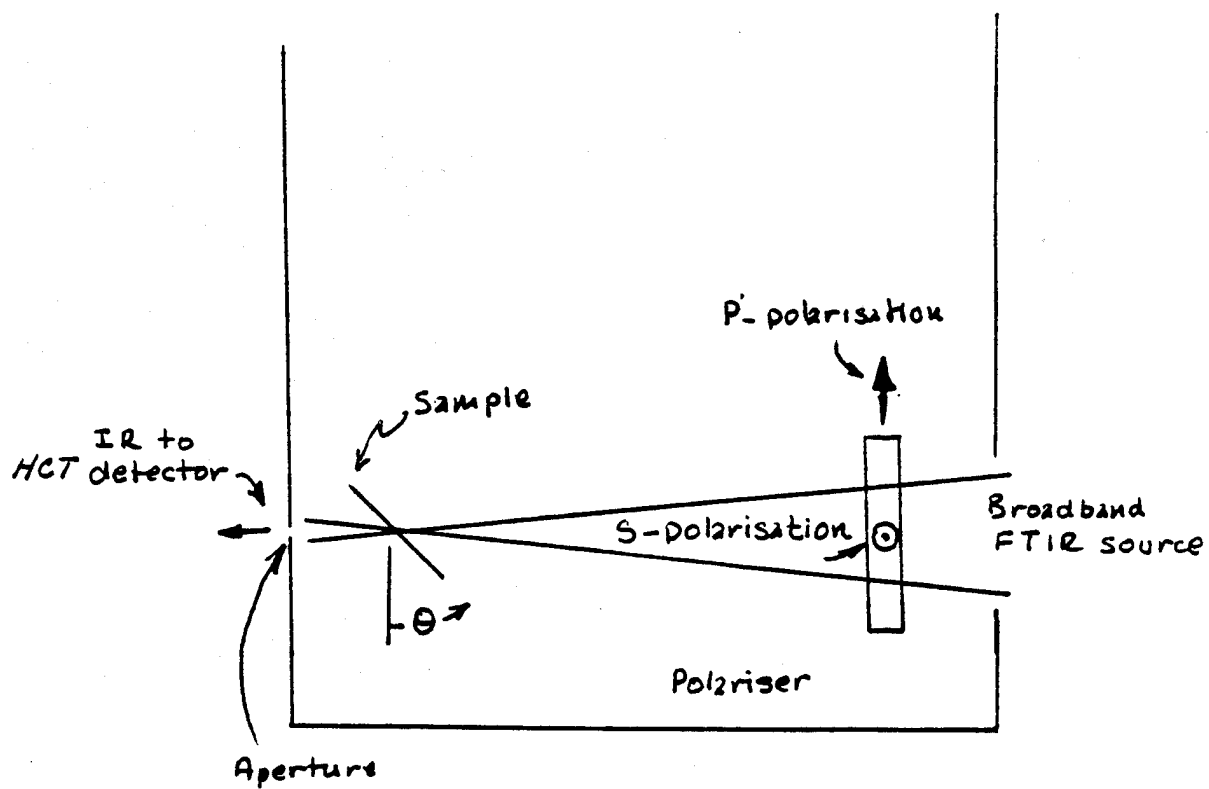
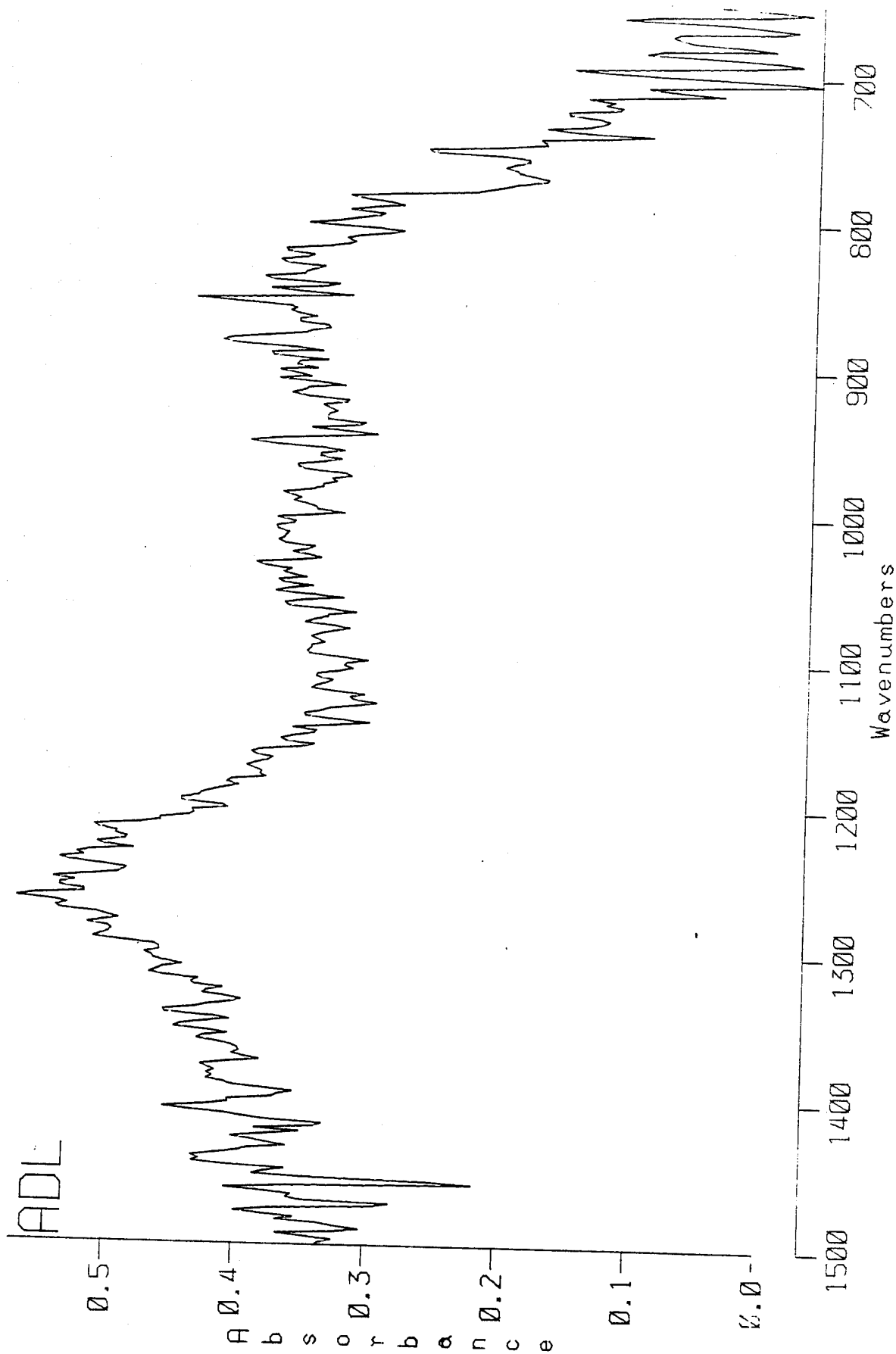


Fig. 2.6 A.D. Little Sample Holder Design

Fig. 2.7 P-S Difference Transmission Spectrum₁ With Edge
Insertion. OW Absorbion at 850 cm



QW126A
P-S FOR #890712 BY EDGE INSERTION EXPERIMENT
RES=4.0

2.1.1.3 Multipass Face Insertion Measurement

Next, measurements on the QW embedded in an AlGaAs waveguide enclosed in dielectric reflectors will be discussed. This Fabry-Perot structure is used to increase gain (hence detectivity) at the expense of bandwidth.

The most desirable mode of operation of a Fabry-Perot resonator type device embodiment is to have the light impinge on it at the Brewster angle. This permits the entire p-polarized impinging energy to be introduced into the cavity. On the contrary, the Attenuated Total Reflection (ATR) measurement technique which we have used so far with end insertion of light to the device is not very suitable. This is because the active cavity is about $4\mu\text{m}$ deep from the front surface of a 25 mil thick substrate. Most of the light focussed at the end simply would not see the quantum-well and be guided outside the active layer as shown in Fig. 2.8

First the FPQW substrate was placed on the FTIR in the ATR configuration. Data were taken with polarizer at $\theta=0^\circ$ (s-polarization); $\theta=30^\circ$, 45° , 60° and 90° (p-polarization). Maximum absorbance is expected to be observed with the electric field parallel to the plane of incidence (p-polarization). The absorbance spectra are shown in Figs. 2.9a-e. The absorbance data measured relative to the left minimum of the left maximum are shown in Table I.

TABLE 2.1

Polarization Angle (Degrees)	Location of Peak (μm)	Peak/Foot (unitless) ,
0 (s-polarization)	8.7	0.860
30	8.7	0.86
45	8.7	1.04
60	8.7	1.03
90 (p-polarization)	8.7	1.04

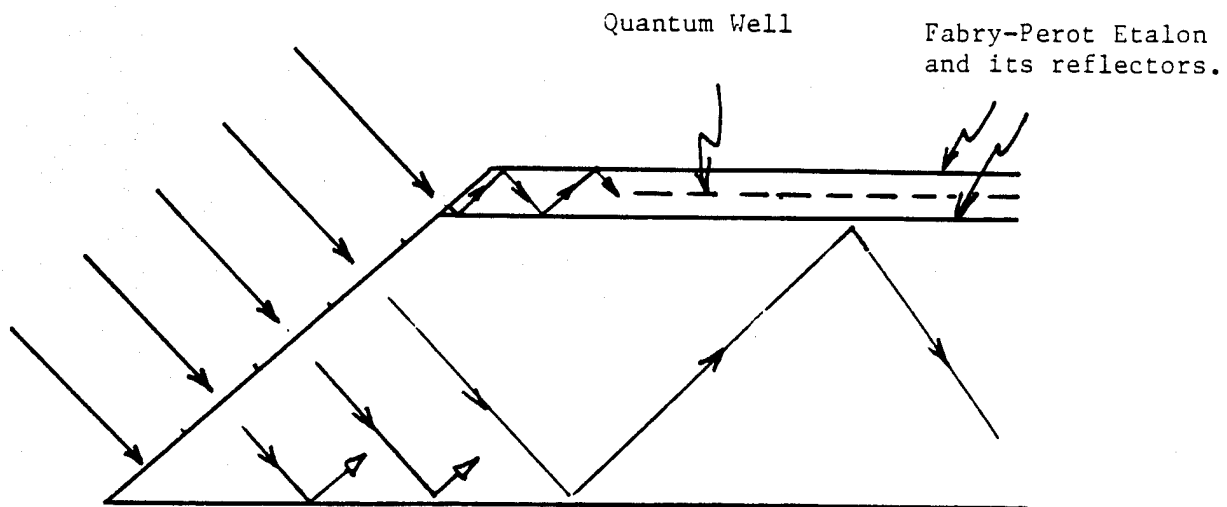


Fig. 2.8 Restricted Energy Insertion To An Etalon
From Its Edge

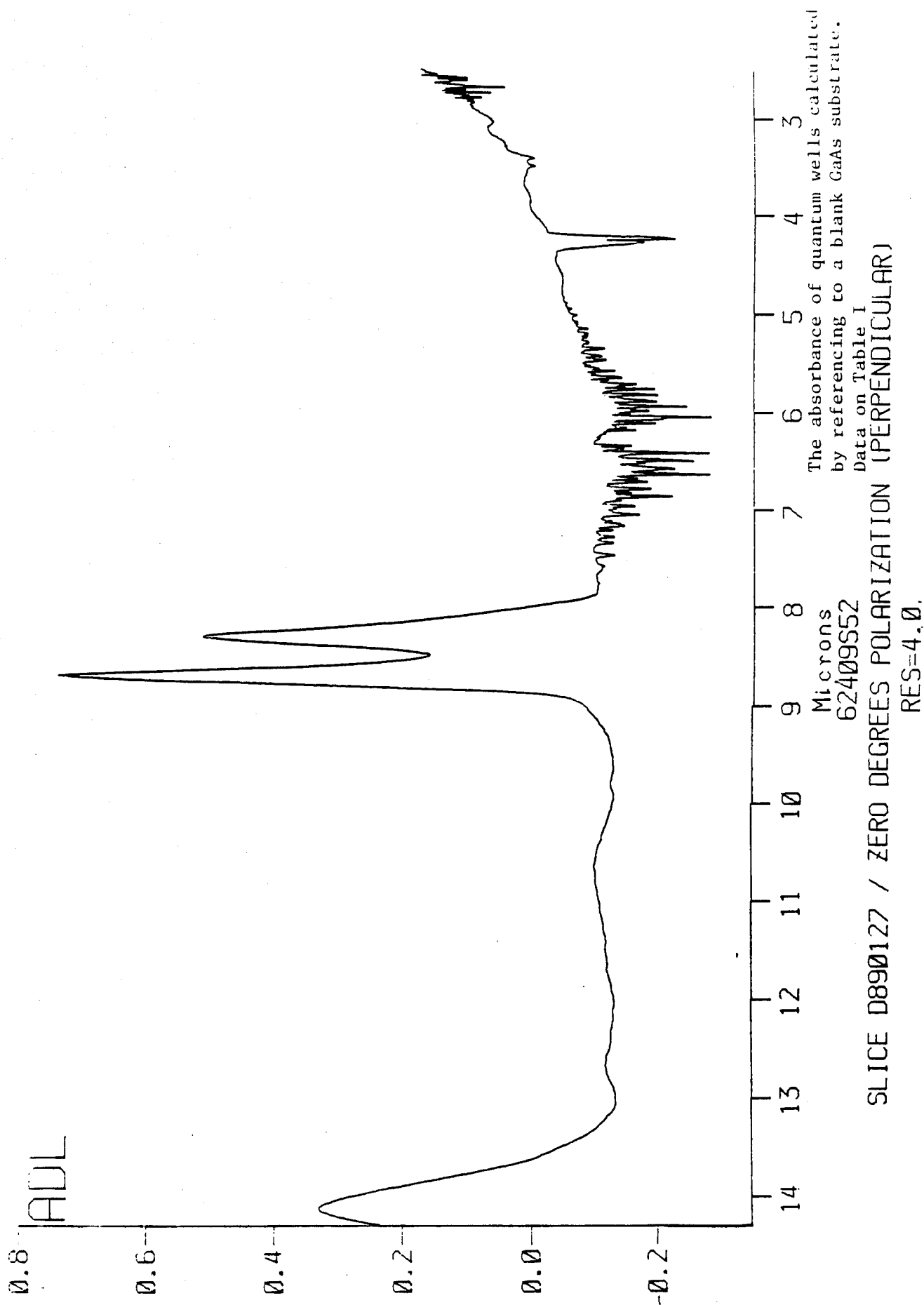
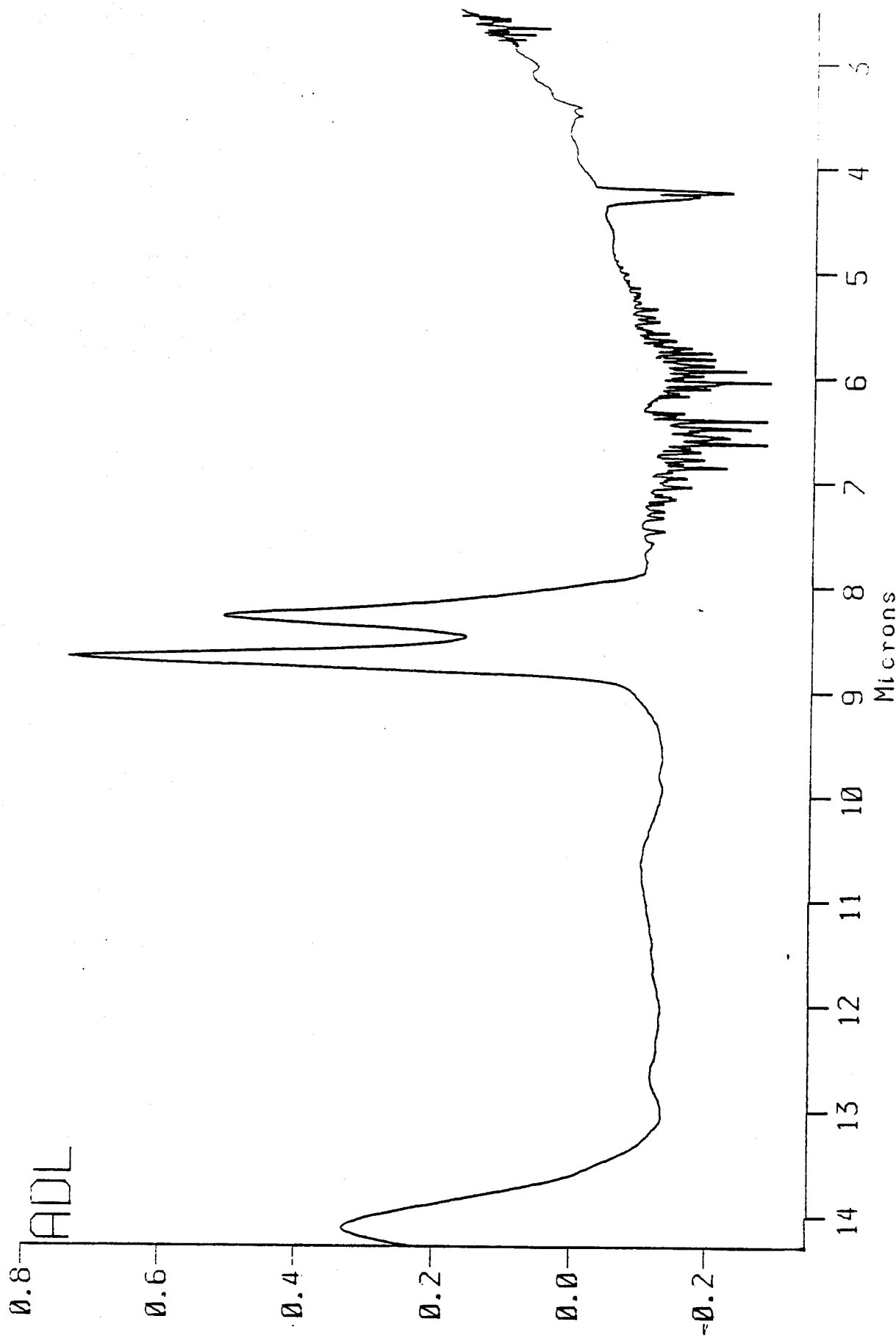
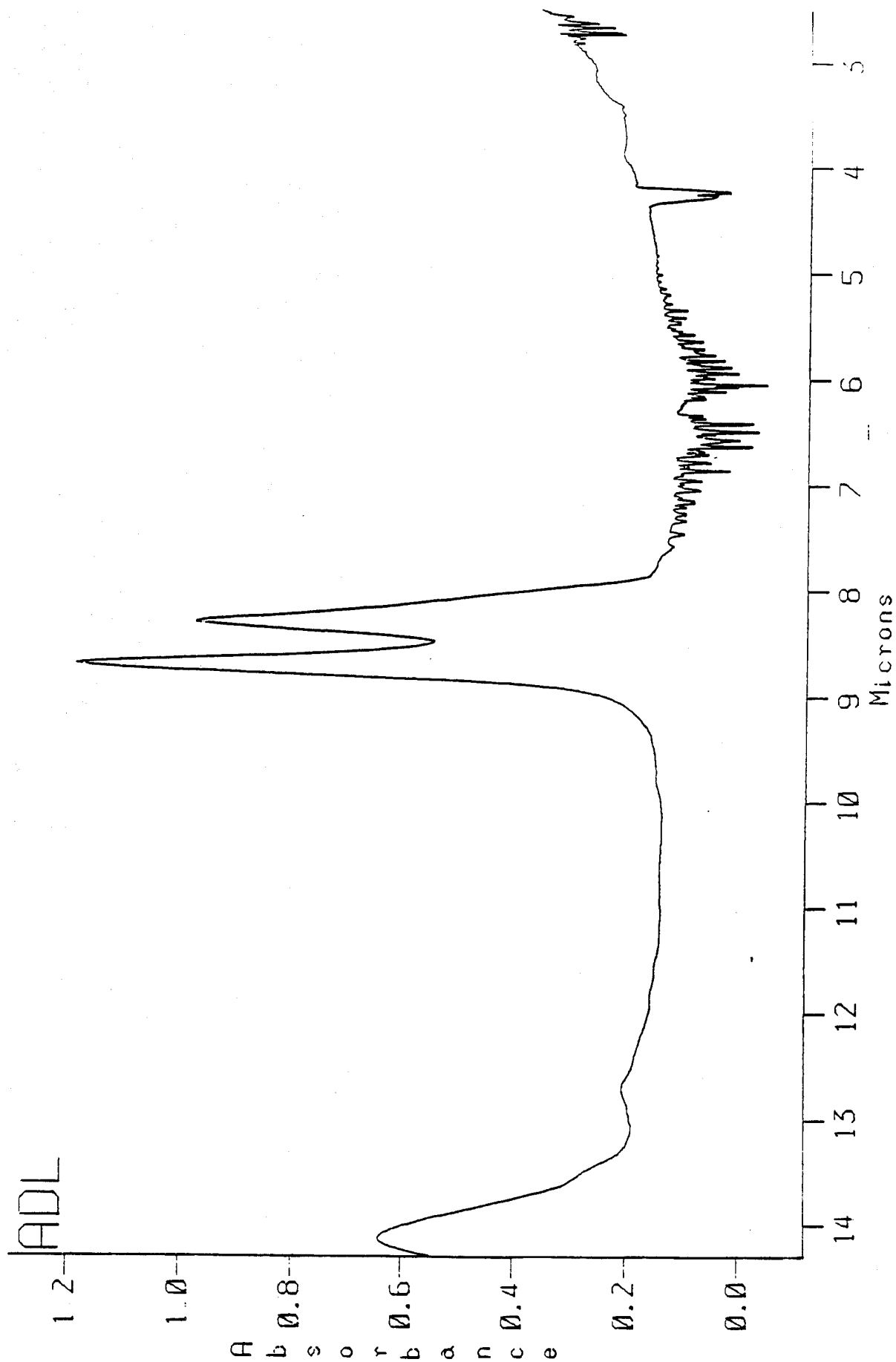


Fig. 2.9a Absorbance of Quantum Wells in a FT Etalon Polarization
Angle = 0 (s-polarization)



SLICE D890127 / 30 DEGREES POLARIZATION
 62409S53
 RES=4.0

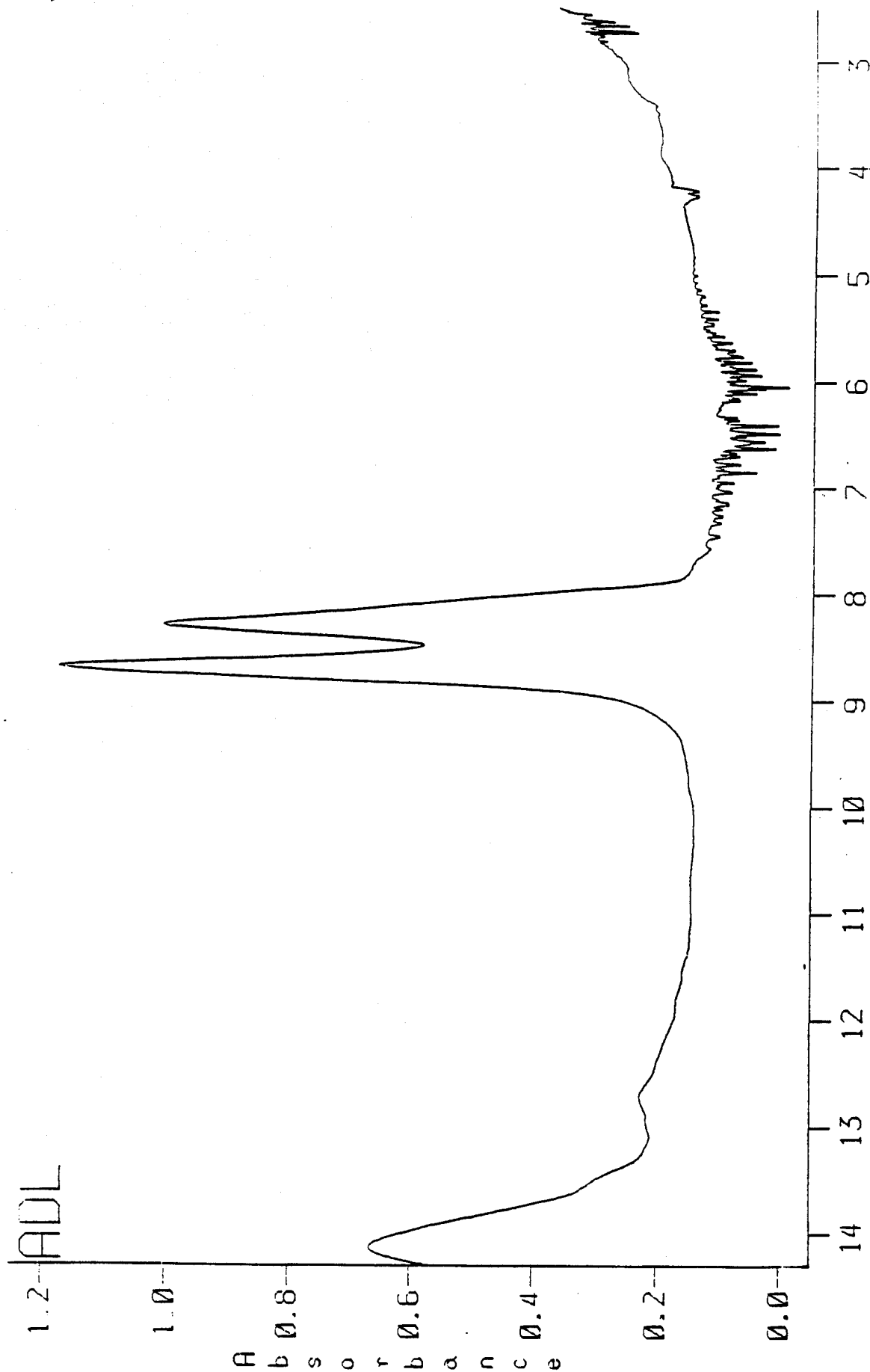
Fig. 2.9b Polarization Angle = 30°



62409554

SLICE D890127 / 45 DEGREES POLARIZATION RES=4.0

Fig. 2.9c Polarization Angle = 45°



SLICE D890127 / 60 DEGREES POLARIZATION
 RES=4.0
 62409555

Fig. 2.9d Polarization Angle = 60°

ADL

1.2

1.0

0.8

0.6

0.4

0.2

0.0

Arthur D Little

Ab sorban e

14

13

12

11

10

9

8

7

6

5

4

3

Microns

62409S56

SLICE D890127 / 90 DEGREES POLARIZATION (PARALLEL)

RES=4.0

Fig. 2.9e Polarization Angle 90° (p-polarization)

Although the trend of increasing absorbance as $\Theta \rightarrow 90^\circ$ is correct a lack of clear $\cos^2\Theta$ dependence seemed not satisfactory.

The polarizer used in this measurement is an old Perkin-Elmer device and may have lost its polarization efficiency. (This was later determined to be 62%.) A new polarizer was obtained from Cambridge Consultants Limited (CCL), an Arthur D. Little subsidiary, to repeat these measurements. In addition, a new sample holder was designed and fabricated to facilitate slanted incidence transmission measurements. The details of these measurements and the sample holder will be discussed in the following paragraphs.

In order to study the sample in a manner maximizing the benefit of the Fabry-Perot resonator, the sample holder shown in Fig. 2.10 was fabricated. Using this sample holder and the CCL polarizer, the QW fabricated between dielectric-high-reflectivity structures with sinusiodally varying index (Rugates) have been evaluated. In addition, the contrast of the old polarizer was evaluated and compared to the new polarizer.

The evaluation of the old polarizer shed light on the puzzling aspects of the results shown in Fig. 2.9. The contrast of the old polarizer has been determined to be 62%. Such poor selectivity may provide the explanation for the rather surprising low and erratic angular dependence of absorbance. In contrast, the polarizing efficiency of the new polarizer has been determined to be 85%.

As a further search into the causes of above mentioned inconsistency, careful measurements of the polarization state of the FTIR were carried out as a function of wavelength.

Unfortunately, the analysis is rather tedious and not of general interest.

Using the new sample holder, the transmission spectra of the FP structure was analyzed at Brewster angle (73°), 45° and at normal incidence. In this report the raw data will be shown.

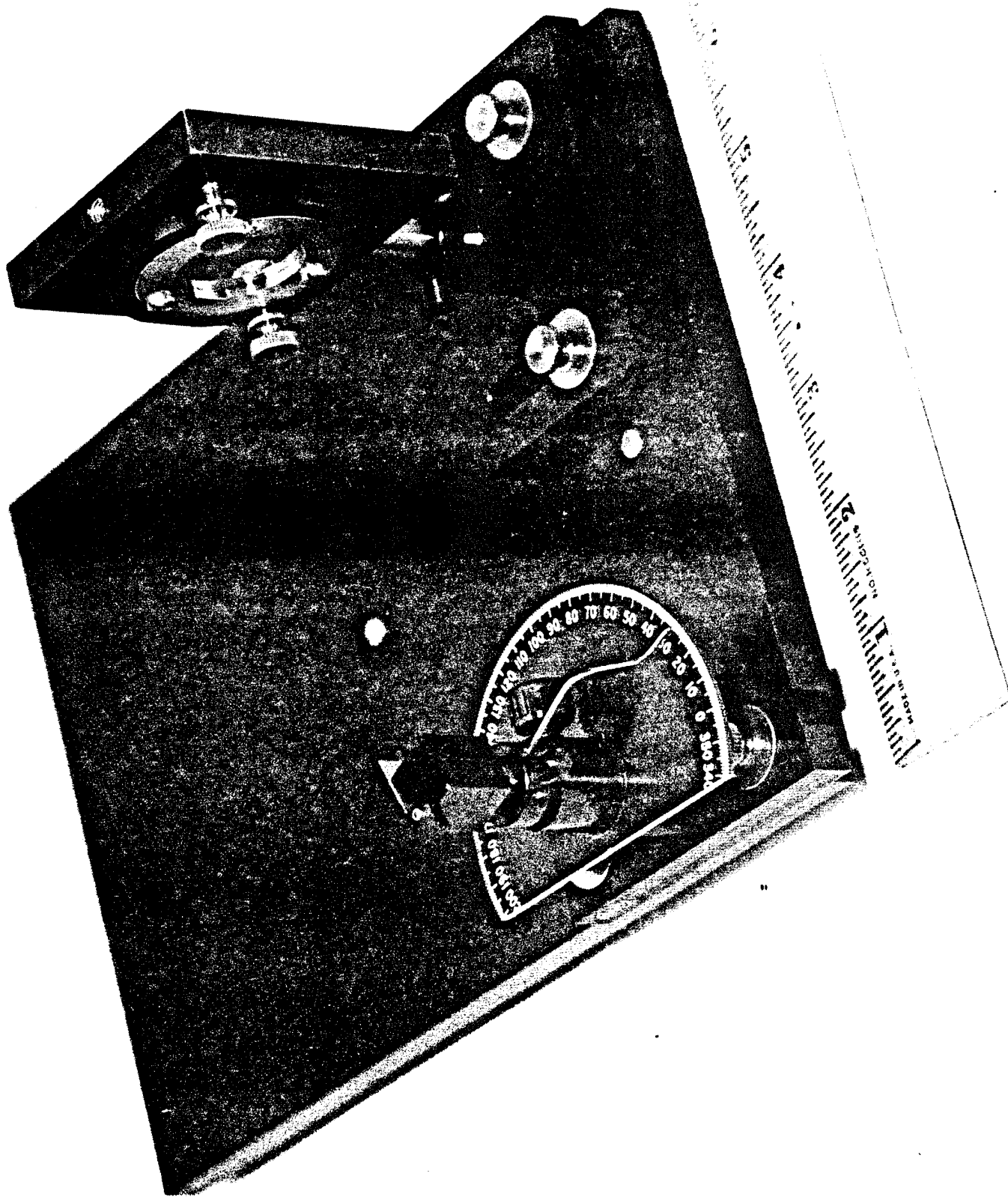


Fig. 2.10 Sample Holder for Variable Angle Transmission Measurements Utilizing a Polarizer

At 45° angle of incidence, s and p polarization data are shown in Fig. 2.11. The Fabry-Perot oscillations between the back and the front rugates are clearly seen at low wavenumbers. The effect of the rugate reflection peak and the QW absorption overlap between 1000 cm^{-1} and 1200 cm^{-1} is shown in Fig. 2.12, the same data at Brewster angle are shown. The reflectivity of the rugate for p-polarization at steep angles sharply drop, therefore, in the p-polarization FP fringes are not existent. This is also when QW absorption is maximum which should appear as a double-humped dip in transmittance which one can see above 1000 cm^{-1} . The identification of these with the previously observed double peaked absorbance maxima around 8.7 μm as reported on Table I will be subject to further data processing.

To sum up, the report on the QW structure and in the current results, the following similarities are seen. QW absorption peak location are both located approximately at 8 μm . The absorption peaks are doublets indicating either a nonuniformity of the QW width or the location of the final states to be out of tune with the first resonant continuum state. The breadth of the peaks, about a micrometer, is similar to previously reported structures.

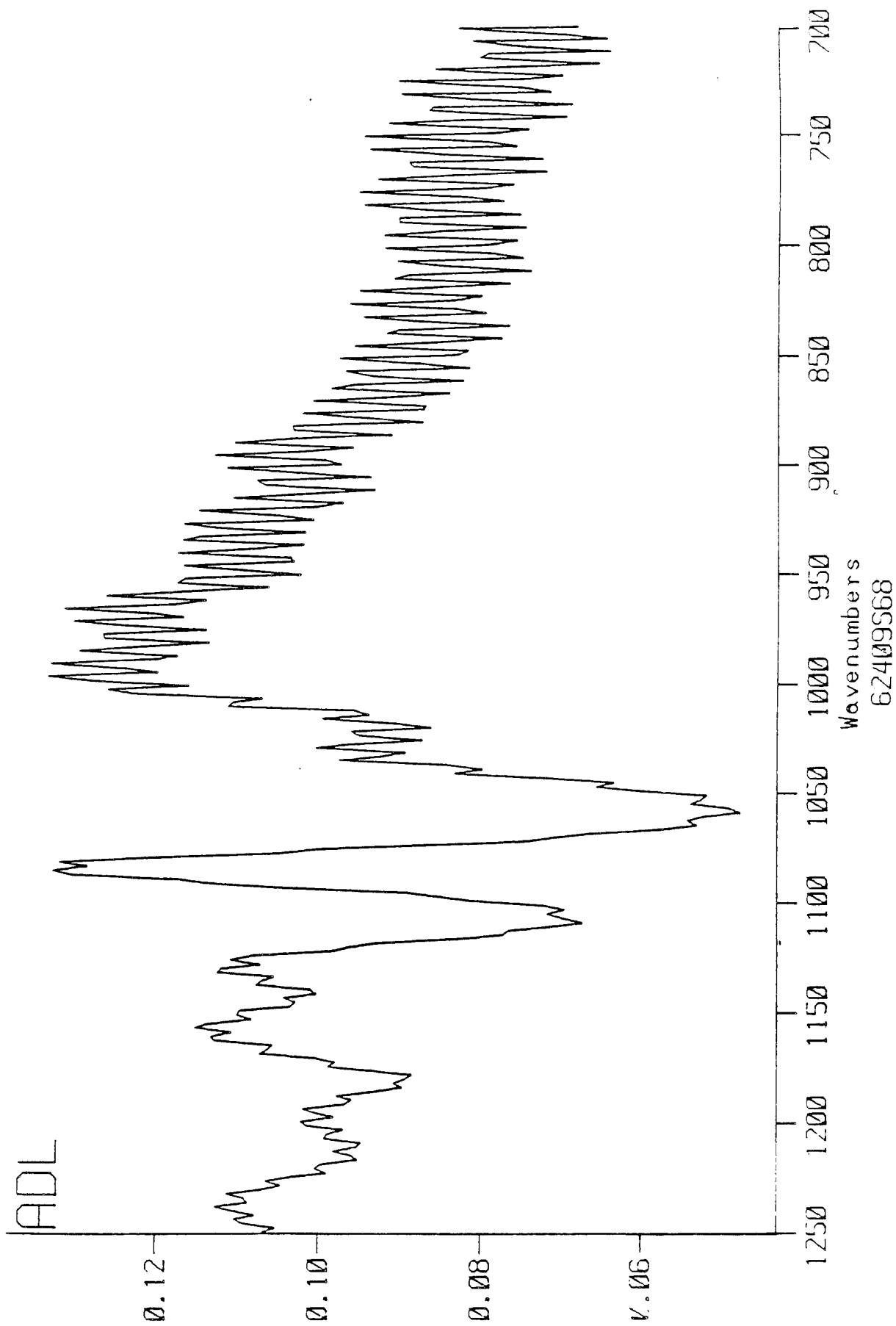
2.2 Electrical Measurements

2.2.1 Methodology

The IR Sensor/Amplifier noise measurements have a twofold objective, i.e.,

- the determination of the sensor NEP
- the selection/matching of an input amplifier to the sensor for minimizing the total system noise.

Fig. 2.13 presents a schematic of the IR Sensor/Amplifier network. A noise model of this circuit is shown in Fig. 2.14. E_n and I_n are noise sources associated with the amplifier. I_{mp} is due to R_p and E_{ns} represents the total sensor noise including the contribution from its internal resistance R_s .



RES-4.0

Fig. 2.11a s-Polarization Transmission Through the QW at 45

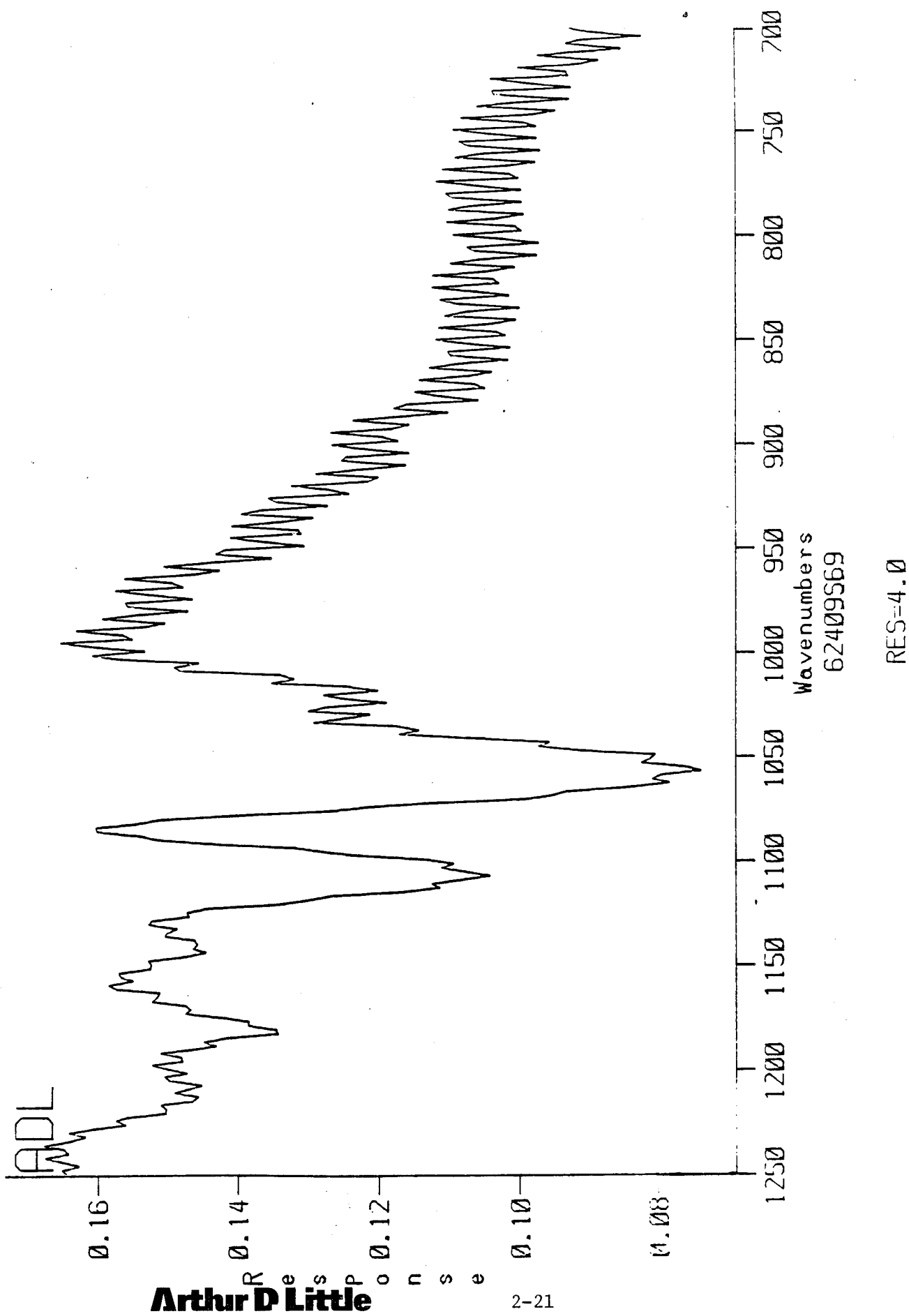
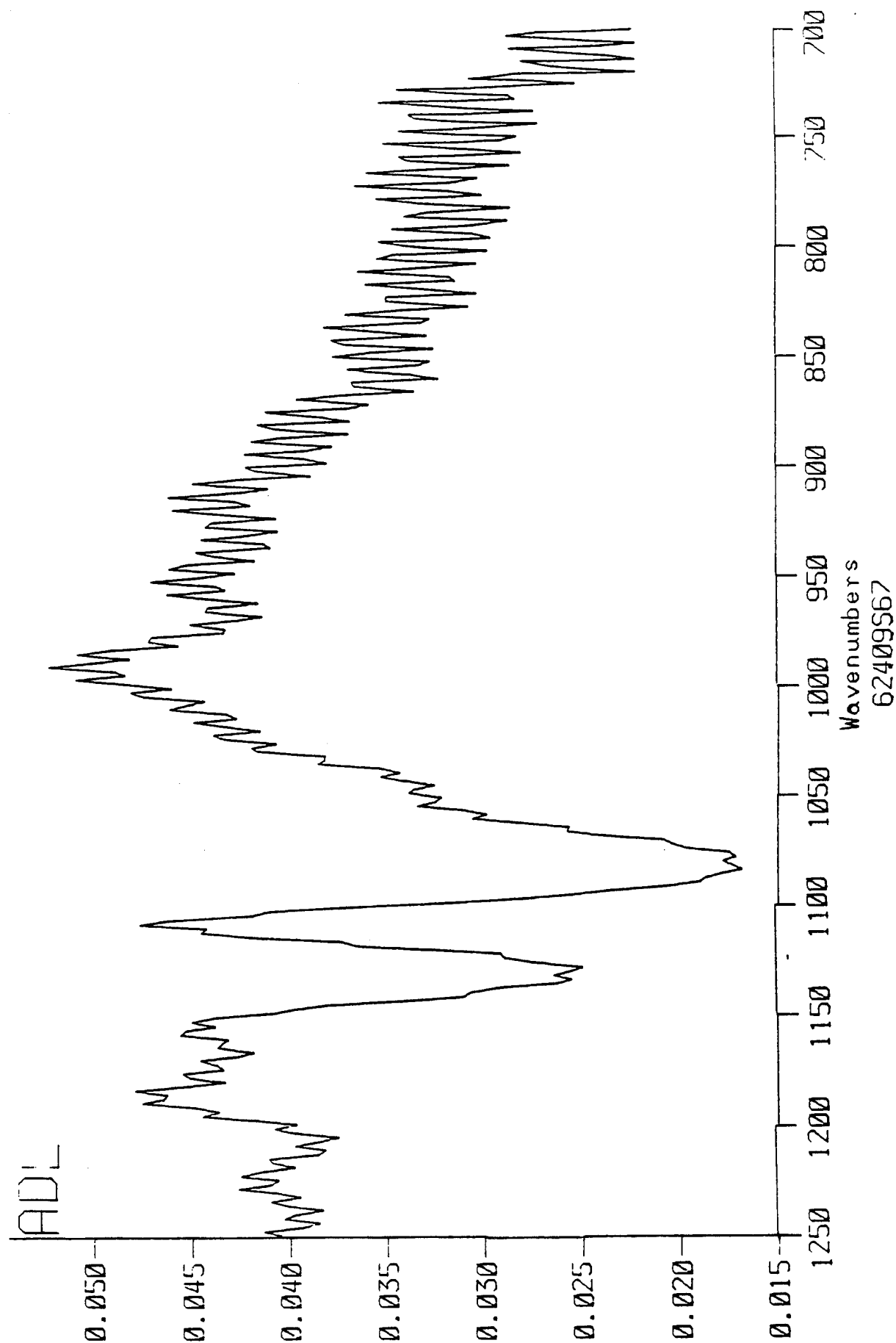


Fig. 2.11b p-Polarization Transmission Through the QW at 45



RES=4.0

Fig. 2.12a s-Polarization Transmission Through The QW at Brewster Angle

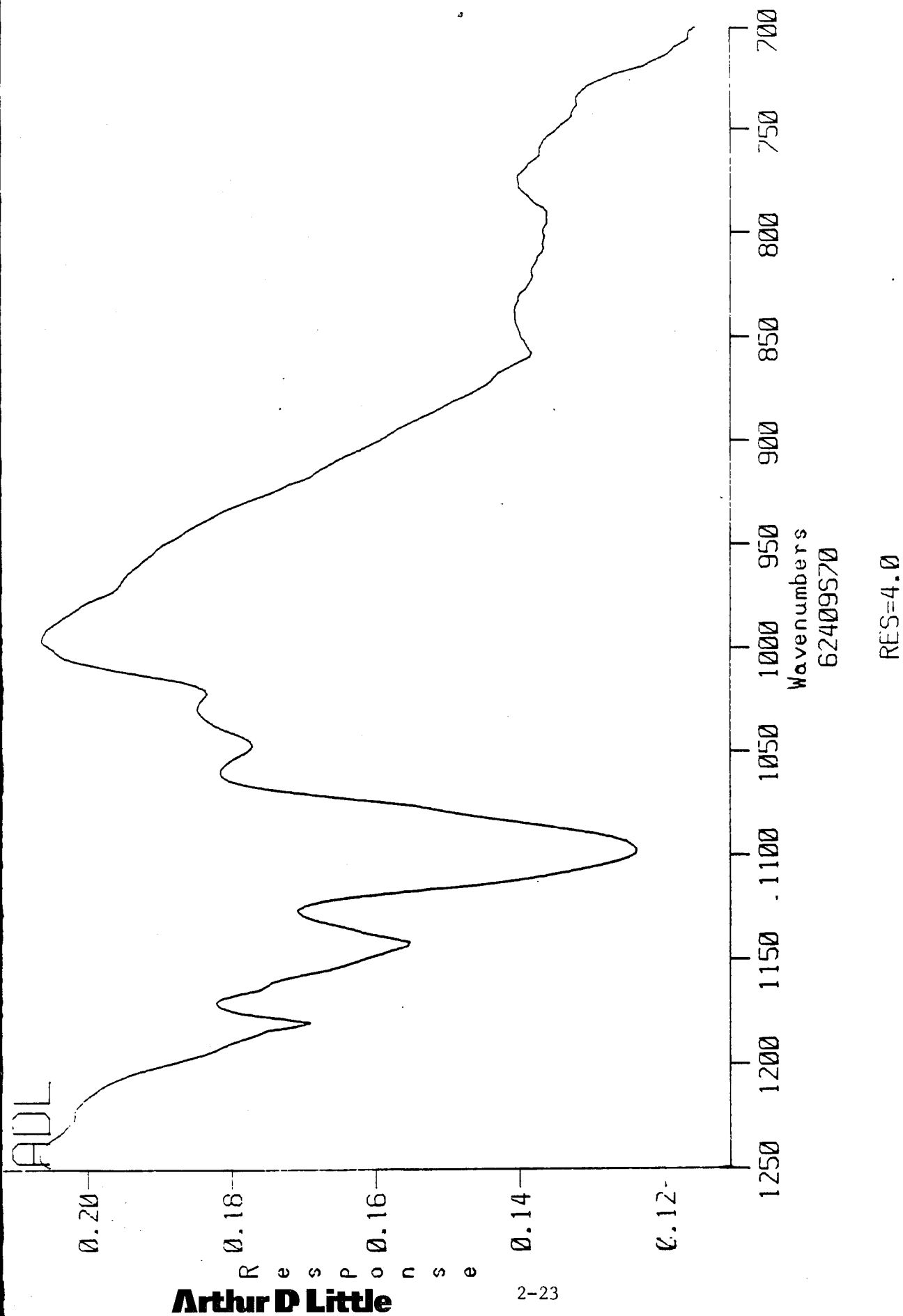


Fig. 2.12b p-Polarization Transmission Through The QW at Brewster Angle

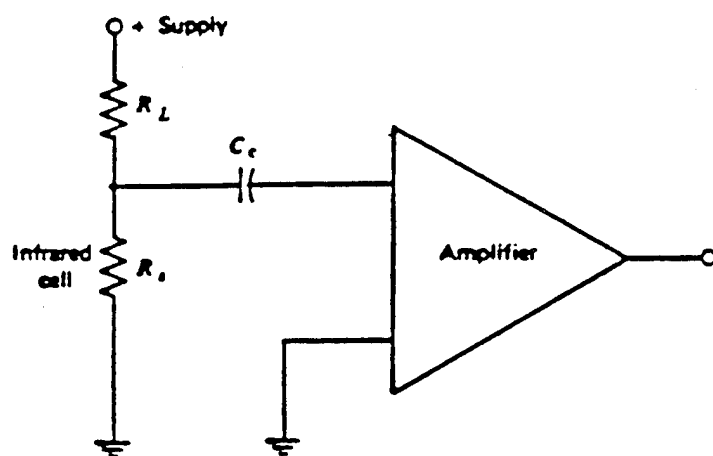


Fig. 2.13 IR Sensor and Amplifier Equivalent Circuit

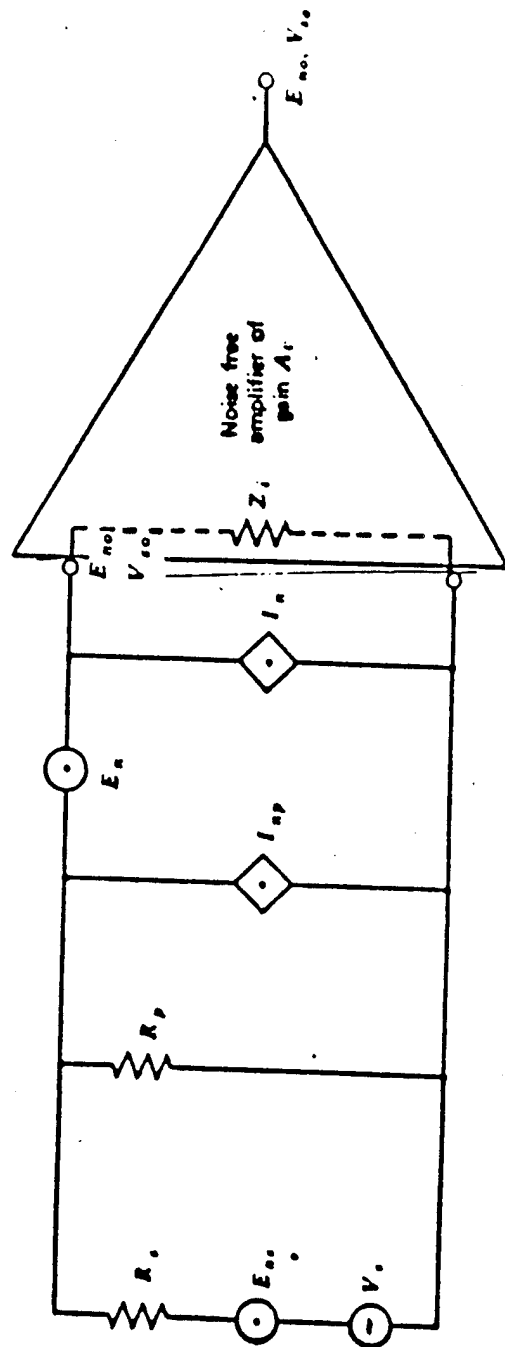


Fig. 2.14 Noise Model of IR Sensor

The sensor NEP is given by

$$\text{NEP} = \frac{\text{Noise Current (A/Hz}^{1/2}\text{)}}{\text{Responsivity (A/W)}} \quad (2.1)$$

$$= \frac{E_{ns}/R_s}{\text{Responsivity}} \quad (2.2)$$

The system noise performance is characterized by the noise factor

$$F = \frac{\text{Output Signal to Noise Ratio}}{\text{Input Signal to Noise Ratio}} \quad (2.3)$$

which, for Fig. 2.14, becomes

$$F = 1 + \frac{E_n^2}{E_{ns}^2 K_t^2} + \frac{(I_n^2 + I_{np}^2) R_s^2}{E_{ns}^2} \quad (2.4)$$

where K_t = transfer function from sensor to output

$$K_t = \frac{V_{out}}{V_{in}} = \frac{Z}{R_s + Z} A_v \quad (2.5)$$

where $Z = \left(\frac{1}{R_p} + \frac{1}{Z_i} \right)^{-1}$

Z_i = noiseless amplifier input impedance

and

A_v = amplifier voltage gain (a noise-free value)

The ideal situation is, of course to have $F=1$, but this is achieved only with $R_p \rightarrow \infty$ and a noiseless amplifier, i.e., I_n and $E_n = 0$. In practice, this objective can often be closely approached by making $R_p \gg R_s$ and by matching R_s to the noise impedance of the amplifier, $R_o = E_n/I_n$. The condition

$$R_s = R_o = E_n/I_n \quad (2.6)$$

can be shown to minimize the total equivalent input noise of the IR Sensor/Amplifier system.

Measurements

All of the noise parameters given above are frequency sensitive and must be measured over the appropriate band. For our chopper tuned set-up, the measurements can be limited to the chopper frequency.

I. Determination of I_n and E_n

For characterization of the PA-100 preamplifier, let us consider R_p as part of the amplifier since it is inadvisable to detach it.

The total equivalent amplifier input noise is then

$$E_{ni}^2 = E_R^2 + E_n^2 + I_n^2 R_s^2 + 2 C E_n I_n R_s \quad (2.7)$$

where

$$E_R^2 = 4k TR \Delta f \quad (2.8)$$

and C = Correlation coefficient between I_n and E_n (assume $C = 0$).

The noise out of the amplifier is

$$E_{no}^2 = K_t^2 E_{ni}^2 \quad (2.9)$$

where

$$K_t = \frac{A_v Z_i}{R_s + Z_i} \quad (2.10)$$

$$\text{If } R_s \rightarrow 0, K_t \rightarrow A_v \quad (2.11)$$

$$\text{and } E_{ni}^2 = E_n^2 = E_{no}^2 / A_v^2 \quad (2.12)$$

$$\text{If } R_s \rightarrow \infty, E_{ni}^2 \rightarrow I_n^2 R_s^2 \quad (2.13)$$

$$\text{and } I_n^2 = E_{no}^2 / K_t^2 R_s^2 \quad (2.14)$$

$$\text{and } Z_i = K_t R_s / A_v \quad (2.15)$$

Therefore, the amplifier can be fully characterized by the following measurements.

1. Determine

Then find A_v and E_n for equation (2.12).

2. Determine

Then find I_n from equation (2.14) and Z_i from equation 2.15.

II. Determination of Sensor Noise

With the sensor added to the preamplifier, the total input noise becomes

$$E_{ni}^2 = E_s^2 + E_R^2 + E_n^2 + I_n R_s^2 \quad (2.16)$$

To find E_s

1. Measure

$$\text{Then } E_{ni}^2 = E_{no}^2 / K_t^2$$

$$\text{And } E_R^2 = 4kT\Delta f$$

and since all other parameters in Eq. 2.15 have been found, E_s can be determined.

2.2.2 Noise Measurement of EG&G HgCdTe Detector and PA-100 Voltage Preamplifier

In order to develop our ability to measure detectivities and to help us in the evaluation of our own MQW-IR detector, a commercial HgCdTe detector was acquired. Our HgCdTe detector is an intrinsic photoconductor. The basic working principle of this detector is to create electrons and holes simultaneously across-the-gap transition. The J15D12 series EG&G HgCdTe detector is designed to operate at the peak efficiency at 11 μm . The normal operating range with optimum parameters is in the 8 to 12 μm wavelength region with high responsivity. The detector is mounted in a metal dewar with a ZnSe (uncoated) window, transparent up to 14 μm . This detector is a low impedance device, typically 10 to 150 Ω with a low voltage noise preamplifier.

We also acquired the EG&G PA-100 voltage preamplifier which is designed to match with J15D12 series HgCdTe detectors and has a bandwidth from 5 Hz to 1 MHz.

In addition to the electrical noise of the HgCdTe detector, the preamplifier itself is the source of additional noise. This noise is minimized when the internal resistance R_s of the detector is equal to the equivalent input noise resistance of the amplifier. In order to find the actual detector internal resistance R_s which gives the best gain in the preamplifier output the following experiment was conducted. The schematic diagram of the experimental set-up is shown in Fig. 2.16.

This experiment was carried out to find the resistor value which empirically gives the best gain in the preamplifier output and it was found to be around 70-100 Ω . The next step is to find the actual noise associated with the preamplifier. In order to perform the noise measurement of the preamplifier, a 200 Ω wire wound (WW) resistor is used and the experiment is conducted at room temperature (300K) and also at liquid nitrogen temperature (77K). From the initial measurements it seems that noise contributed by the preamplifier is

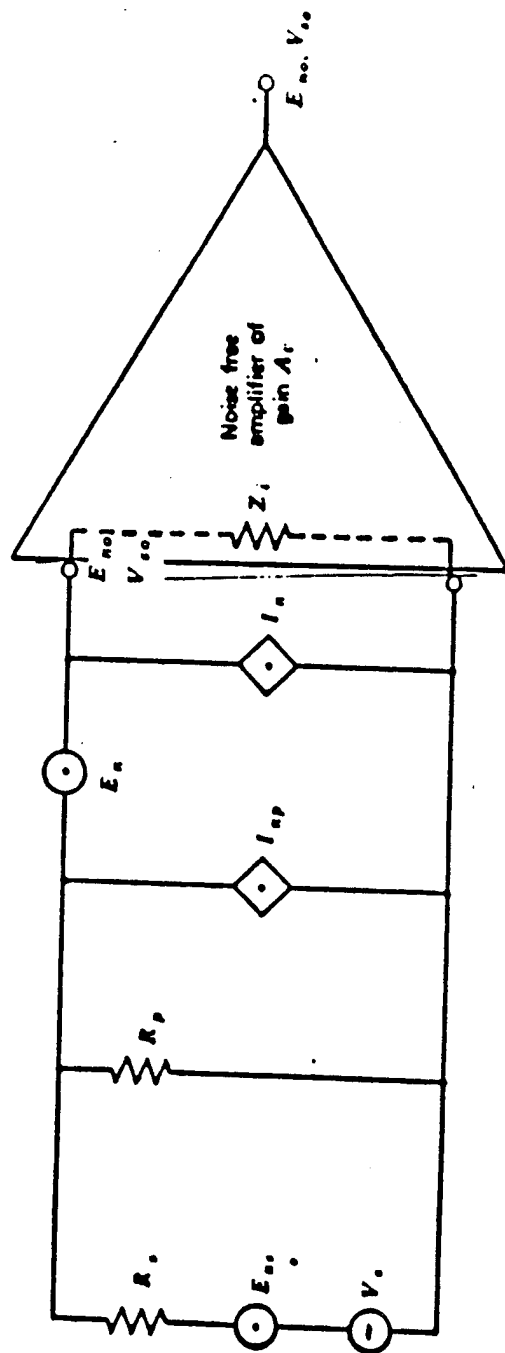


Fig. 2.16 Schematic Diagram of the Equivalent Circuit

negligible in the higher frequency range but at low frequency $1/f$ noise dominates. The signal to noise ratio as a function of frequency for a 200Ω WW resistor at 300K and 77°K temperatures are shown in Figs. 2.17. Having concluded the noise analysis in connection with the preamplifier, we then measured the noise equivalent power (NEP) of the HgCdTe detector. The experimental set-up for the determination of the detector NEP is shown in Fig. 2.18.

2.3 Device Design

Device design was carried out using Schiff's formulation of the physics of quantum wells.

Start with Schiff's definitions.

$$\beta = \left\{ \frac{2m}{\hbar^2} (V_o - E) \right\}^{1/2} \text{ and } \alpha = \left\{ \frac{2m}{\hbar^2} E \right\}^{1/2} , \quad (2.17)$$

where E is the energy of the confined electron and V_o is the potential well "height."

Construct dimensionless variables by:

$$\eta = a\beta \text{ and } \xi = a\alpha , \quad (2.18)$$

where a is half the width of the quantum well.

Schiff shows that:

$$\xi \tan \xi = \eta . \quad (2.19)$$

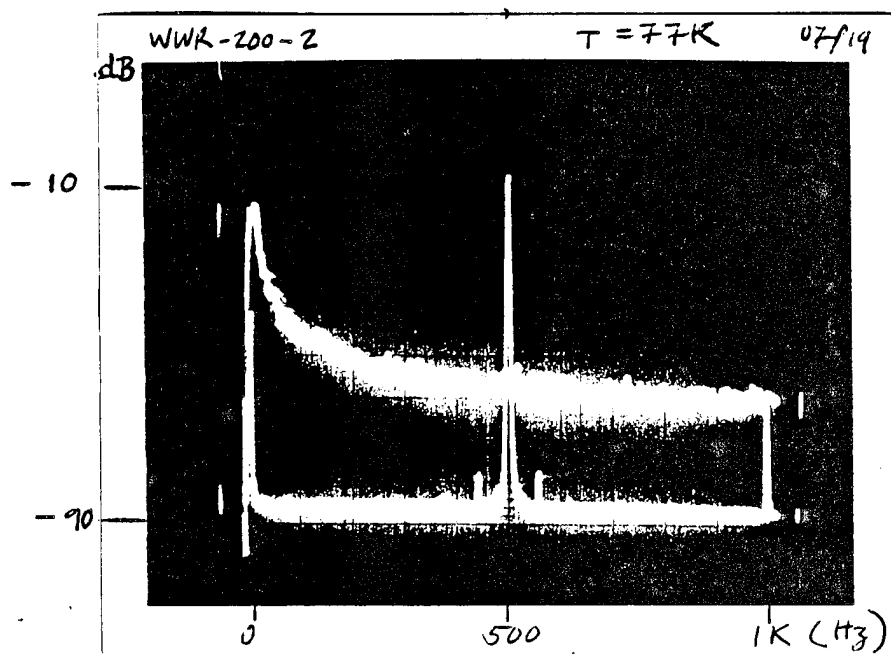
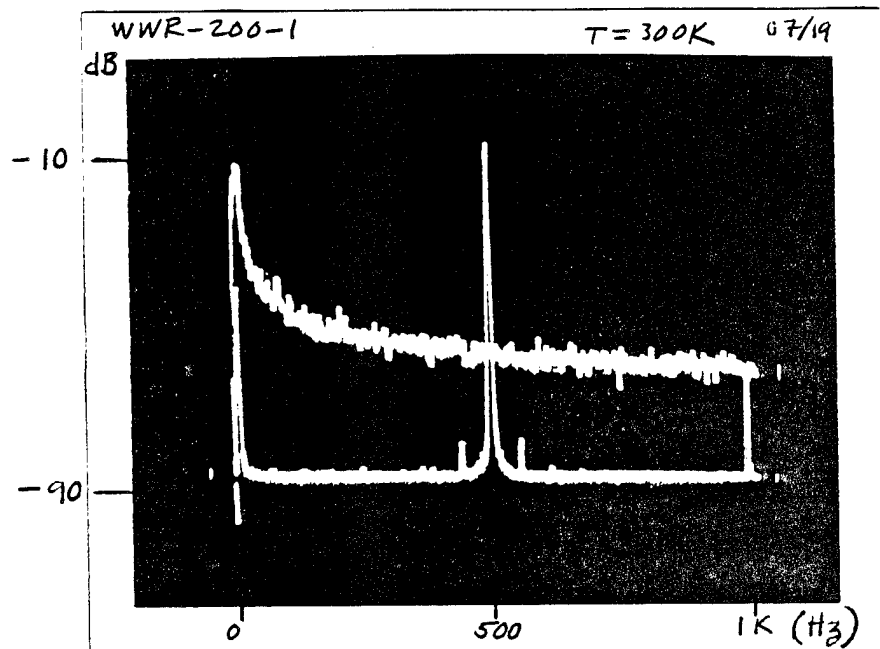
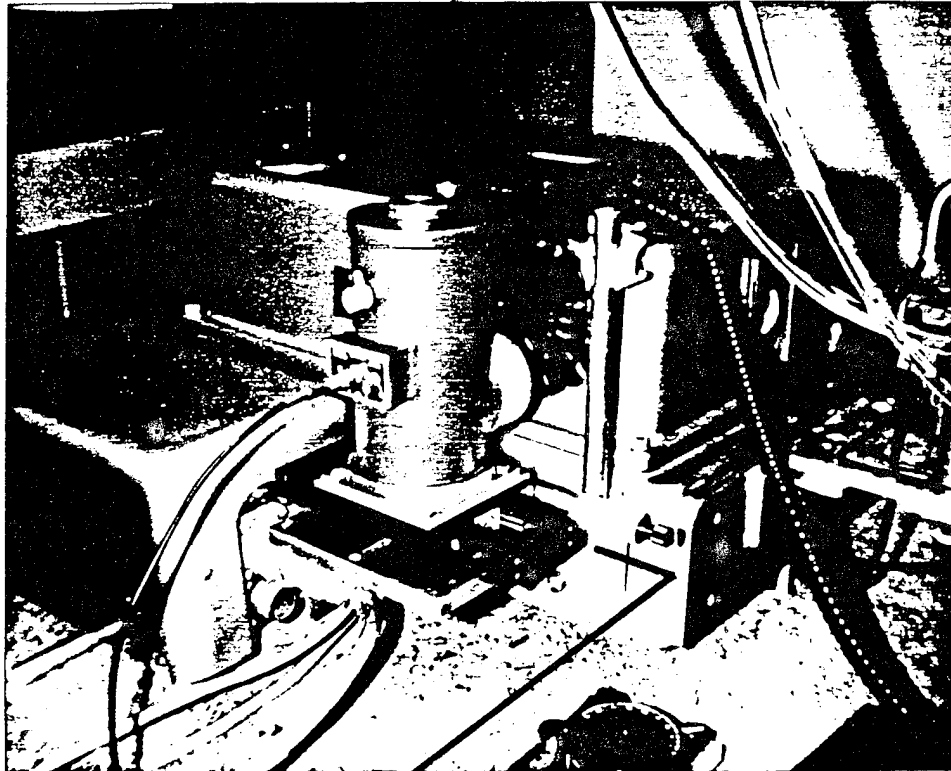


Fig. 2.17 Signal and Noise Measurements Result

Chopper Covering
a ZnSe lens



xy-stage (only
x-micrometer
adjusted) carrying
the HgCdTe detector

Sample holder for
room temperature
measurement

Fig. 2.18 Experimental Set-up

Also observe that

$$\xi^2 + \eta^2 = \rho^2 \quad (2.20)$$

where
$$g^2 = \frac{2ma^2}{\hbar^2} V_o \quad (2.21)$$

If we plot Eq. 2.19 and 2.21, we see that the solutions are the intersections of the Eq. 2.19 and the family of curves generated by Eq. 2.21.

We use two design principles: excitation to band edge, and excitation to a resonance level.

2.3.1 Excitation to Band Edge

Here the rule is

$$\hbar\omega = V_o - E. \quad (2.22)$$

This is equivalent to

$$\eta^2 = g^2 \frac{1.24}{v_o} \frac{1}{\lambda_o} \quad (2.23)$$

where v_o , the potential well height in electron volts and λ is the design wavelength in microns.

Eqs. 2.19 and 2.20 can be used to obtain

$$\rho = \xi / \cos \xi \quad (2.24)$$

Using Eq 2.23, we can recast Eq. 2.19 as

$$\xi = \sin^{-1} \left(\frac{1.114}{\sqrt{V_o \lambda_o}} \right) \quad (2.25)$$

The design algorithm is as follows:

1. Choose V_o and λ .
2. Calculate ξ with Eq. 2.25.
3. Calculate ρ with Eq. 2.24.
4. Calculate a with Eq. 2.21.
5. Reiterate 1-4 till a satisfactory pair of V_o and a are obtained.

2.3.2 Excitation to a Resonant State

If an electron in the conduction band with kinetic energy ϵ passes over a quantum well V_o deep, the transmission probability is one when the wavelength λ satisfies $\lambda=4a$ where a is half the well width. To excite an electron to this resonance state, we must have

$$\frac{\hbar^2}{2m} \left(\frac{\pi}{2a} \right)^2 + (V_o - E) = \hbar \omega \quad (2.26)$$

This modifies 2.23 to read

$$\eta^2 = s^2 \frac{1.24}{V_o \lambda_o} - \frac{\pi^2}{4} \quad (2.27)$$

Using 2.19 and 2.24 along with 2.26, one can get

$$\frac{\xi^2}{\cos^2 \xi} \left(\frac{1.24}{V_o \lambda_o} - \sin^2 \xi \right) = \frac{\pi^2}{4} \quad (2.28)$$

The design algorithm is the same as the one given at the end of Section 2.3.1

2.4 Coupler (Transformer) Design

A planar multiple quantum well, MQW, structure must be obliquely illuminated in order to orient the E vector of the incident radiation for interaction with the bound charges in the wells. However, the optics of focal plane arrays are designed to produce normal incidence for the central ray. Therefore, some sort of input transformer is needed to interface a planar MQW structure with focal plane optics.

This section describes one approach to such a transformer and evaluates it on the basis of an Equivalent Fill Factor, EFF, which is defined here as that fraction of the total input radiation which is delivered to the MQW with an E-vector orientation appropriate for interaction. The configuration is that of Fig. 2.19 where square-based pyramids of index, n , sit on the substrate containing the planar MQW structure

The E-vector component of interest is that which lies normal to the MQW in the GaAs substrate. Such a component can only be produced by the parallel polarization component of the input radiation. Thus for non-polarized illumination it may be important to maximize the capture of the useful 50% of the input radiation by orienting the transformer surface so as to produce Brewster angle incidence of the central ray. This will be the starting point of the analysis to follow which will consider only central ray illumination of the transformer. The only variable will be the refractive index of the transformer, which will determine the pyramid angle θ , and the object of the analysis will be to find the EFF vs. n relationship so that the transformer may be optimized for maximum EFF.

The procedure to be followed will be one of ray tracing wherein the rays will be subdivided into groups that undergo one, two, etc. internal reflections before incidence on the substrate. For each ray group we must calculate the transformer surface area through which the rays

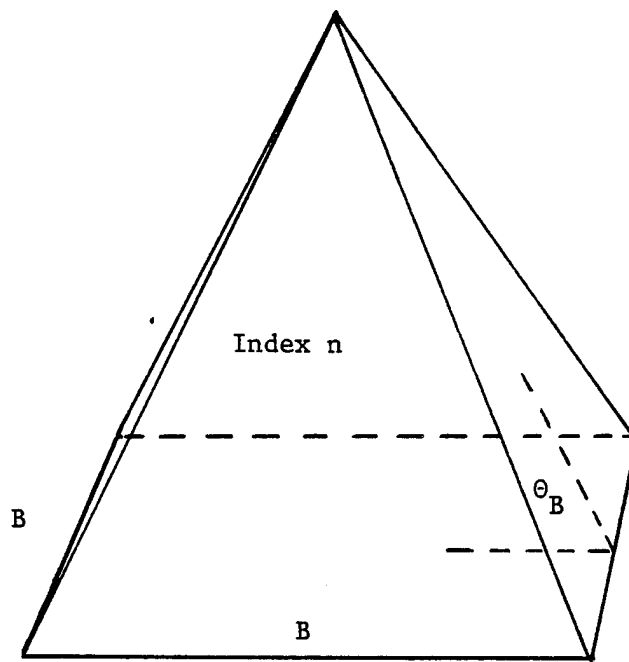


Fig. 2.19 Pyramid Structure to Couple Near Normal Rays

enter, the reflection loss at the transformer/substrate boundary, and the ray angle in the substrate with respect to the plane of the MQW. Then EFF may be obtained from the following expression.

$$\text{EFF} (n) = 1/A \sum_j A_j (1-R_j) \sin \alpha_{rj} \quad (2.29)$$

where A = total transformer surface area

A_j = surface area for ray group j

R_j = transformer/substrate reflection loss for ray group j

α_{rj} = angle of refraction in the substrate (angle between the ray and the normal to the MQW plane) of ray group j

From the Fresnel equations

$$R_j = \frac{\tan^2 (\alpha_{ij} - \alpha_{rj})}{\tan^2 (\alpha_{ij} + \alpha_{rj})} \quad (2.30)$$

where α_{ij} = angle of incidence at the substrate for ray group j

Fig. 2.20 shows the path followed by a ray which undergoes no internal reflections before reaching the substrate. This, we will call a group O-ray. The angles are then

$$\begin{aligned}\theta_B &= \tan^{-1} n, \\ \theta_B - \alpha_{io} &= \sin^{-1} \frac{\sin \tan^{-1} n}{n}\end{aligned}\tag{2.31}$$

$$\text{and } \sin \alpha_{ro} = \frac{n \sin \alpha_{io}}{3.4}\tag{2.32}$$

The quantity $\sin \alpha_{ro}$ is just the projection of the O-ray vector on the normal to the MQW and is the value needed for the EFF calculation.

If the transformer index is such that

$$\alpha_{io} \leq \theta_B - \alpha_{io}, \text{ or } 2\alpha_{io} \leq \theta_B$$

then all rays will be O-rays.

Since $2\theta_B - \alpha_{io} = 90^\circ$, (the Brewster condition) the maximum θ_B for which all the O-ray condition can be satisfied is

$$\alpha_B = 60^\circ$$

which corresponds to

$$n = 1.73$$

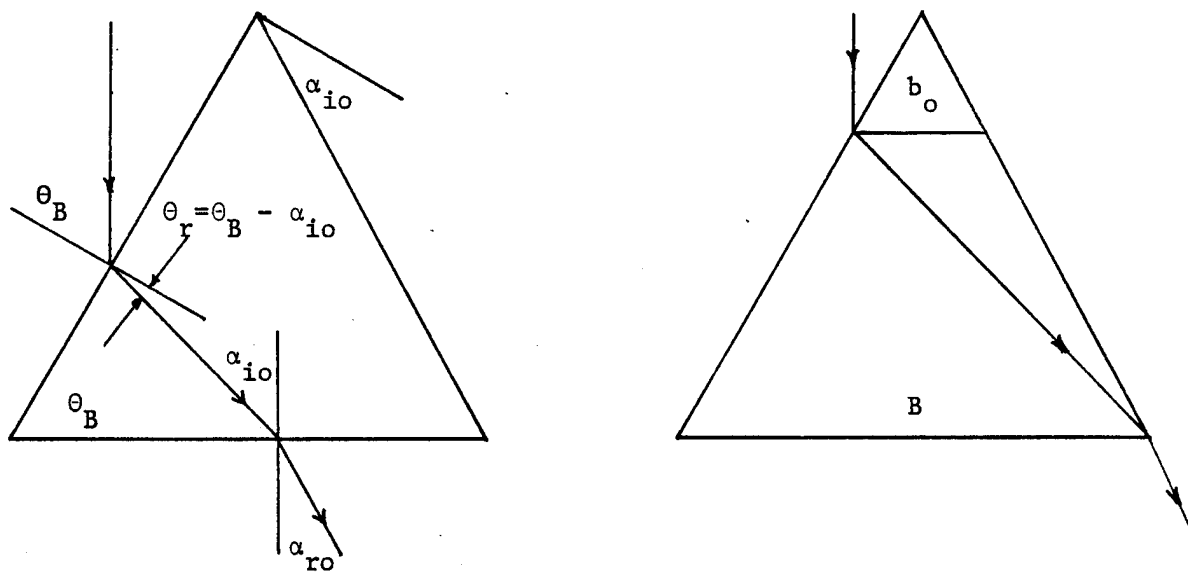


Fig. 2.20 Group O-Ray Traces

Thus for transformers with indices ranging from 1 to 1.73, only O-rays will be present and the EFF calculation is quite simple. For

$$\begin{aligned}n &= 1.73 \\ \alpha_{io} &= 30^\circ \\ \alpha_{ro} &= 15^\circ \\ \sin \alpha_{ro} &= .25 \\ R_o &= .069 \\ \text{EFF}_o(1.73) &= .23\end{aligned}$$

For $n > 1.73$, only a fraction of the rays incident on the transformer will be O-rays. These will be the rays that enter the lower part of the transformer with a projected area $B^2 - b_o^2$.

Now

$$A_o/A = 1 - b_o^2/B^2 \quad (2.33)$$

$$\text{and } b_o = B \frac{\tan \theta_B \tan \alpha_{io} - 1}{\tan \theta_B \tan \alpha_{io} + 1}$$

giving

$$\frac{A_o}{A} = 1 - \frac{\tan \theta_B \tan \alpha_{io} - 1}{\tan \theta_B \tan \alpha_{io} + 1}^2 \quad (2.34)$$

$$\text{for } \theta_B \geq 60^\circ$$

For $n = 3.4$

$$\begin{aligned}\theta_B &= 73.6^\circ \\ \alpha_{i0} &= 57.2 \\ \alpha_{r0} &= 57.2 \\ \sin \alpha_{r0} &= .841 \\ R_o &= 0 \\ A_o/A &= .536 \\ \text{EFF}_o(3.4) &= .45\end{aligned}$$

Thus EFF is considerably improved by increasing the index beyond 1.73 even though less of the transformer area is available for O-ray production. Since the higher number ray groups can only add to the EFF value, it would seem that the choice of a high index transformer is desirable. However, the higher the index, the taller the pyramid, and it is possible to reach a height that will result in adjacent pyramids intercepting light meant for their neighbors, which would reduce resolution. Fig. 2.21 shows the problem, and it can be seen that in order to forestall shadowing, the value of θ_B must be limited so that

$$\theta_B \leq \tan^{-1} 2F, \text{ or } n \leq 2F \quad (2.35)$$

where F = F-number of the focal plane optics.

Thus, the lowest F number compatible with a Brewster angle transformer with $n = 3.4$ would be $F = 1.7$. Similarly, if $F = 1$, then $n = 2$ is the maximum transformer index allowed.

These conditions seem too restrictive and it may be appropriate to relax the condition that the pyramid angle be equal to the Brewster angle.

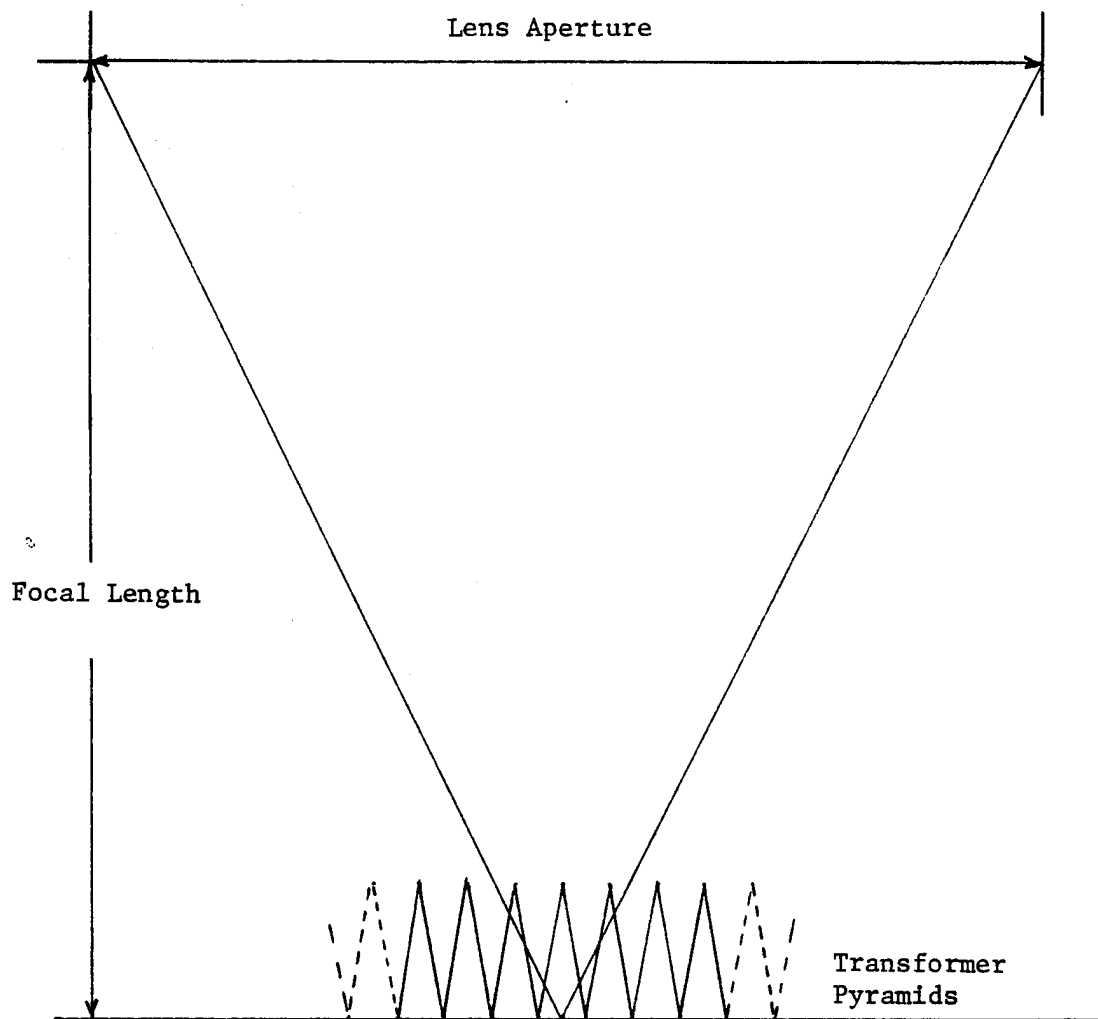


Fig. 2.21 Adjacent Pyramid Shading at Low F-Number

The detector design principle can be generalized to be able to pick the base angle of the pyramids to be independent of the index. A further restriction can be placed upon the pyramids so that one pixel will not shadow the adjacent ones. Thus, the base angle θ must satisfy the expression

$$\theta \leq \tan^{-1} 2F \quad (2.36)$$

where F = optical system F-number.

Fig. 2.21 defines the angles and ray path for the group O-rays.

As before, the equivalent fill factor is given by

$$EFF(n) = 1/A \sum_0^j A_j T_j \sin \alpha_{rj} \quad (2.37)$$

where A = total transformer surface area
 A_j = surface area for ray group j
 T_j = interface transmission factor
 α_{rj} = substrate refraction angle

$$\text{Now } T_j = T_1 T_{2j} \text{ where} \quad (2.38)$$

$$T_1 = 1 - \frac{\tan^2(\theta - \theta_r)}{\tan^2(\theta + \theta_r)}, \quad \text{and} \quad (2.39)$$

$$T_{2j} = 1 - \frac{\tan^2(\alpha_{ij} - \alpha_{rj})}{\tan^2(\alpha_{ij} + \alpha_{rj})} \quad (2.40)$$

For the O-ray group

$$\theta_r = \sin^{-1} \frac{\sin \theta}{n} \quad (2.41)$$

$$\alpha_{io} = \theta - \theta_r \quad (2.42)$$

$$\alpha_{ro} = \sin^{-1} \frac{n \sin \alpha_{io}}{3.4} \quad (2.43)$$

and

$$\frac{A_o}{A} = 1 \quad \text{for } \alpha_{ro} \leq 90^\circ - \theta \quad (2.44)$$

$$= 1 - \frac{\tan \theta \tan \alpha_{ro} - 1}{\tan \theta \tan \alpha_{ro} + 1} \quad \text{for } \alpha_{ro} > 90^\circ - \theta \quad (2.45)$$

Figs. 2.22a, and b define the angles and ray path for the group 1 rays and O-rays respectively.

For 1 rays:

$$\Phi = 2\theta - \theta_r - 90^\circ \quad (2.46)$$

$$\alpha_{r1} = 3\theta - \theta_r - 180^\circ \quad (2.47)$$

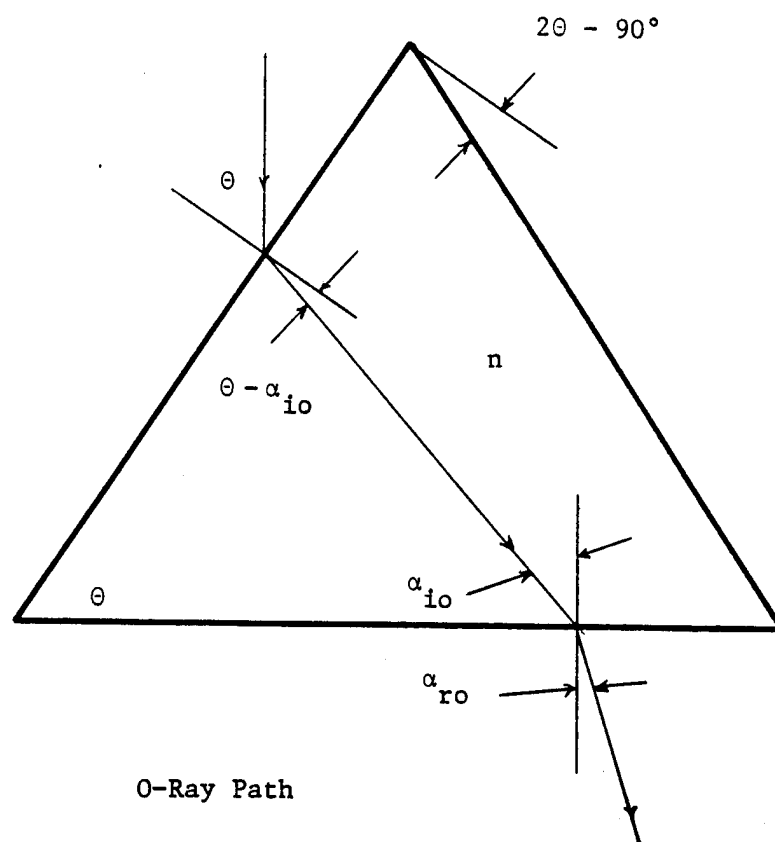
$$\alpha_{r1} = \sin^{-1} \frac{n \sin \alpha_i}{3.4} \quad (2.48)$$

and

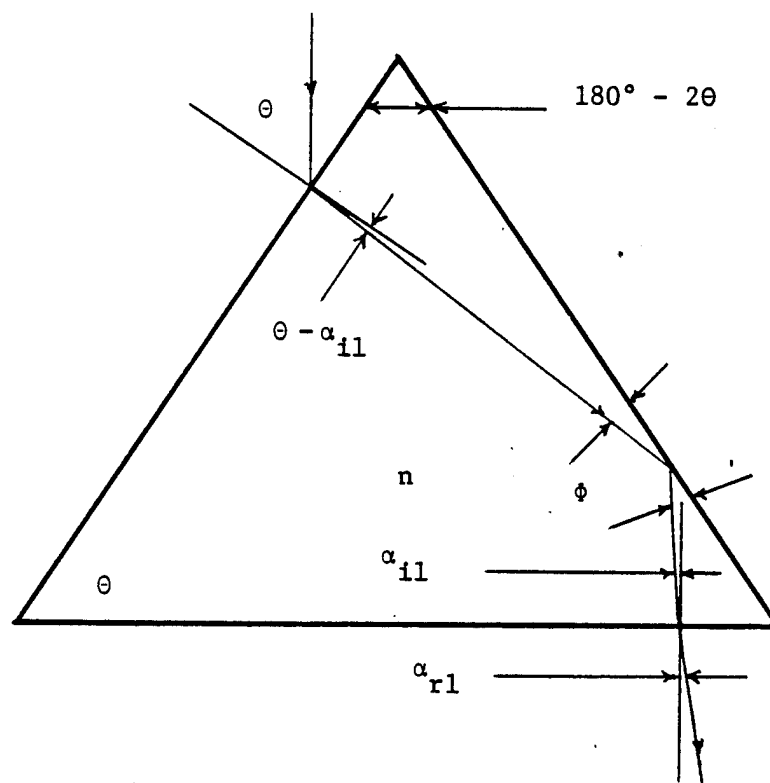
$$\frac{A_1}{A} = 1 - \frac{A_o}{A} \quad \text{if there are no ray groups} \quad (2.49)$$

higher than 1, a condition which is satisfied if

$$\Phi \leq 180 - 2\theta \quad (2.50)$$



O-Ray Path



l-Ray Path

Fig. 2.22 O-Ray and l-Ray Paths

Actually, the group 2 rays will be internally reflected within the transformer only if Φ satisfies the condition

$$\Phi < 90^\circ - \sin^{-1} 1/n \quad (2.51)$$

and such reflection is of course necessary for the group 1 rays, or any higher order group, to contribute to the EFF.

Table 2.2 shows the various angles and related EFF parameters for a number of transformer examples. If these are to be used with a F-1 optical system then

$$\theta_{\max} = 63.4^\circ,$$

a condition satisfied by all but the last example.

The table evidences the need for a transformer index of at least 3.4, and shows that even higher values may be better. The table also shows the benefit of making the base angle as large as possible, subject to the F-number limit.

TABLE 2.2
TRANSFORMER EXAMPLES

θ	n	θ_r	α_{10}	α_{r0}	ϕ^{**}	α_{il}	α_{rl}	T_1	T_{20}	T_{21}	A_0/A	A_1/A	Σ_0	Σ_1	EFF
45	3.4	12	33	33	-	-	-	.82	1	-		0	.45	0	.45
60	1.73	30	30	14.7	-	-	-	1	.92		1	0	.23	0	.23
60	3.4	14.8	45.2	45.2	15.2	-14.8	-14.8	.93	1	1	.93	.07	.61	.02	.63
60	4.0	12.5	47.5	60.2	17.5	-12.5	-14.8	.88	.99	.99	.91	.09	.69	.02	.71
63	3.4	15.2	47.8	47.8	20.8	-6.2	-6.2	.95	1	1	.86	.14	.61	.02	.63
74*	3.4	16.4	57.6	57.6	25.6	25.6	25.6	1	1	1	.52	.48	.44	.21	.65

*Exceeds Shadowing Criteria

**All examples satisfy equations (15) and (16)

3.0 Optical and Electrical Characterizations of the Quantum Well Detectors

We will report in detail devices fabricated as the second iteration during September 1989. Multiquantum well samples have been grown with different growth conditions. The growth specifications of the samples are given below:

<u>Sample No.</u>	<u>Si Temperature (°C)</u>	<u>Characteristics</u>
890901	1250	Si doped buffer, MQW and cap layer
890913	600	Not doped anywhere
890915	1050	Si doped buffer, MQW and cap layer
890919	1050	MQW not doped, doped buffer and cap layer
890920	1100	Si doped buffer, MQW and cap layer
890921	1150	Si doped buffer, MQW and cap layer

These samples were sent to Semiconductor Processing Corporation (SPC) for polishing. Ohmic contacts were vacuum deposited and diffused into the sample by annealing in a forming gas/atmosphere. These samples were further processed to make two types of sample: one with two opposing sides bevelled at 45 degree for the absorption measurement using FTIR, and another one as 3x3 mm pieces with one side bevelled at 45 degree for the electrical measurements. So far measurements have been made on the samples 890901, 890915, 890920 and 890921. The dark I-V characteristics of the samples 890915, 890920 and 890921 are shown in Figs. 3.1, 3.2, and 3.3 respectively. These results show clearly that the sample 890915 is much more resistive than the other two samples which is in agreement with the previous resistivity measurements using one four probe technique. The slope of the curves for the sample 890920, 890921 indicate fairly good ohmic contacts.

OCT. 24 89

SAMPLE # 890915
(One side beveled)
1st piece

○ REVERSE
• FORWARD

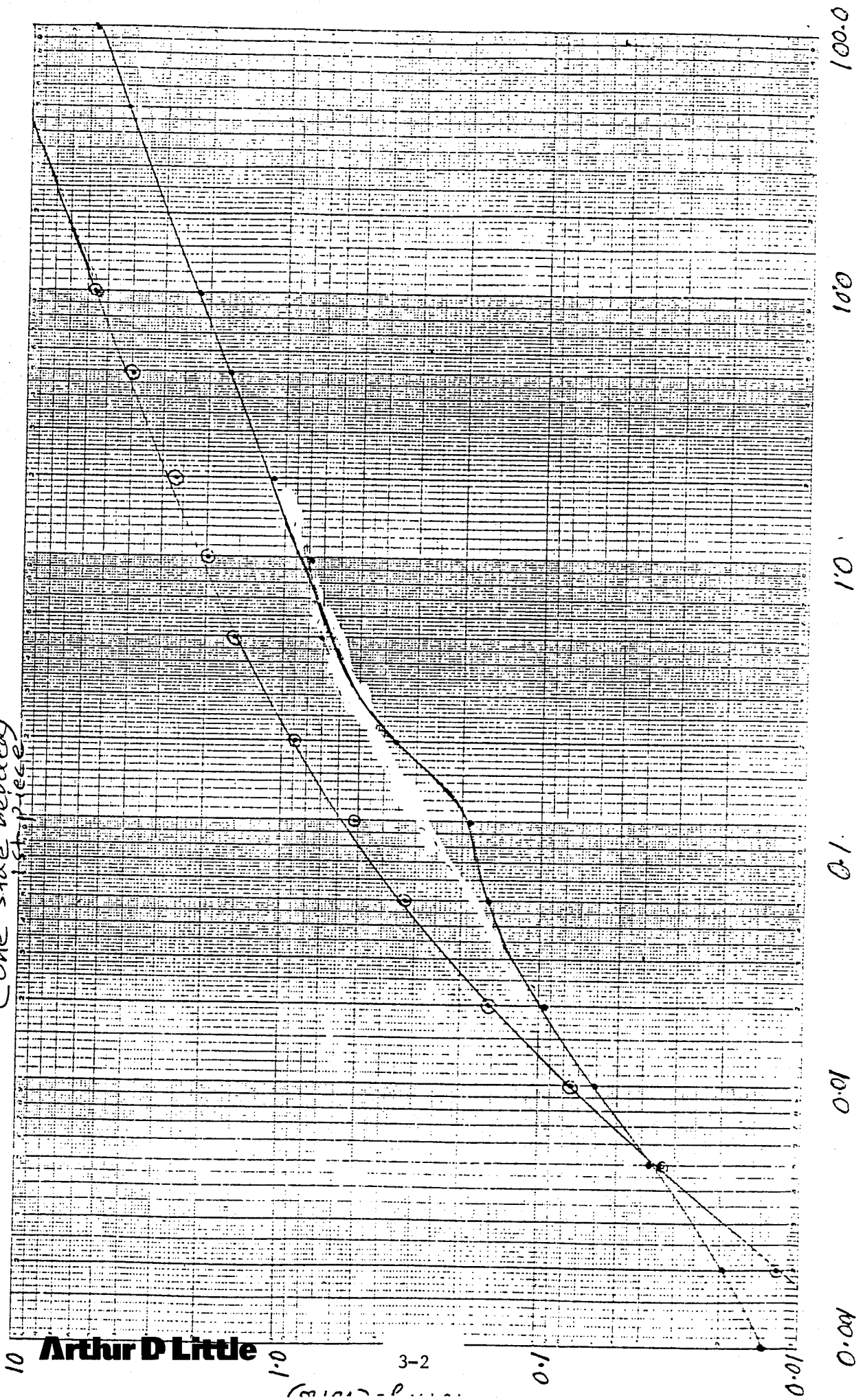


Fig. 3.1 Current vs Voltage for Sample #89015

DARK I-V CHARACTERISTICS

SAMPLE #890920

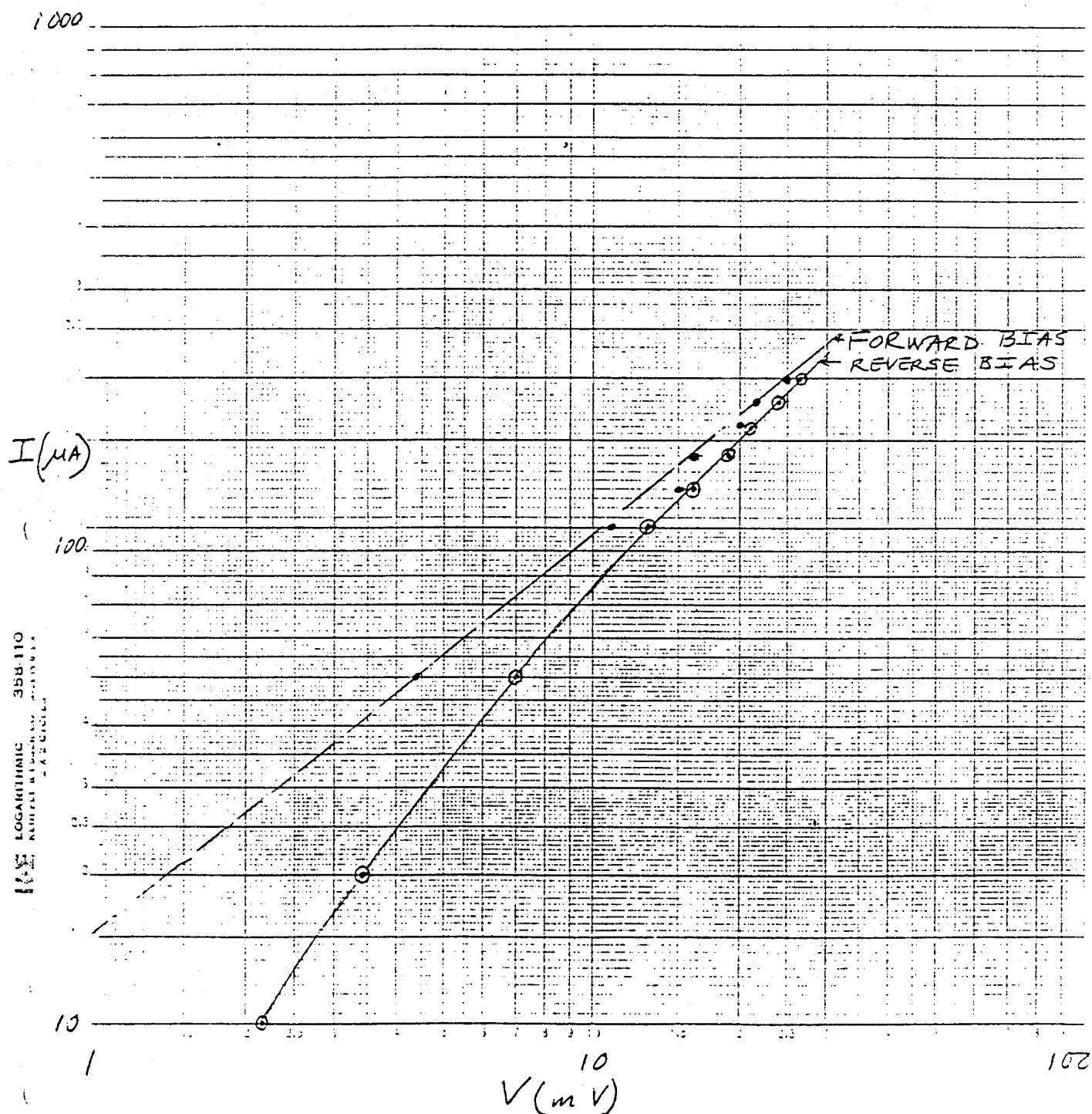


Fig. 3.2 Current vs. Voltage for Sample #890920

DARK I-V CHARACTERISTICS
SAMPLE #890921 AT $T=300^{\circ}\text{K}$

- FORWARD BIAS
- REVERSE BIAS

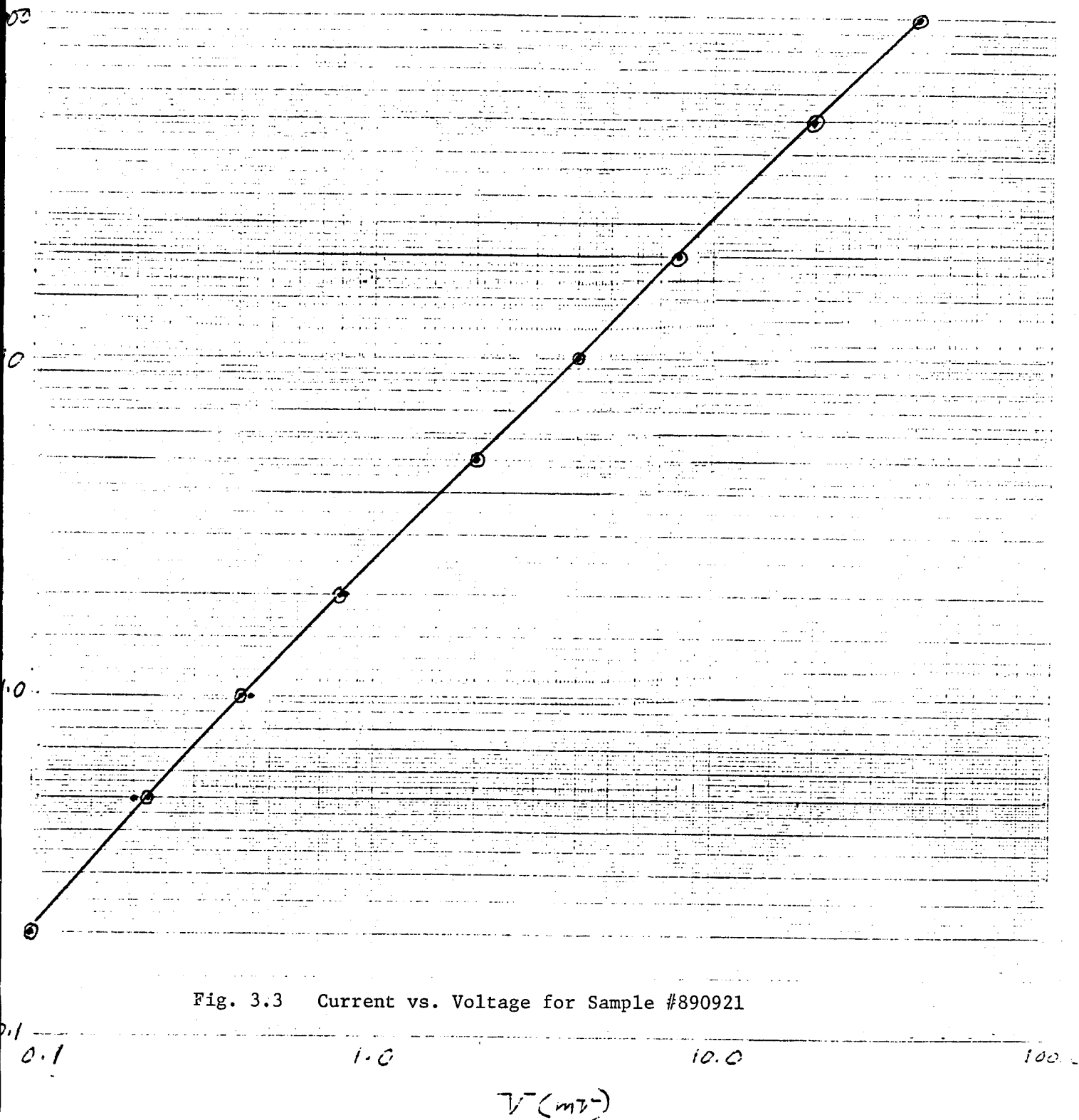


Fig. 3.3 Current vs. Voltage for Sample #890921

Following these measurements, absorption measurements using FTIR were carried out on the samples 890901, 890905 and 890920. In this experiment a polarizer (IGP-226) was used to align the electric vector of the optical field parallel and perpendicular to the quantum well planes. The transmission spectra for the parallel and perpendicular polarizations are shown in Fig. 3.4 and also for comparison the spectra provided by the manufacturer are shown in Fig. 3.5. The p and s polarizations were compared by taking transmission spectra for a GaAs sample at the Brewster's angle. From Fig. 3.6, one can see that only the p-component of the incident light passed through. After confirming the orientations of the polarizer for proper polarizations, the next step was to perform the absorption measurements on the samples. The absorption spectra were taken for both the samples and were normalized with respect to a blank GaAs whose opposing sides were similarly beveled at 45 degree. The absorption spectra as a function of the wavenumber are shown in Figs. 3.7a-c, Figs. 3.8a-c and Figs. 3.9a-c for the 890901, 890915 and 890920 samples respectively. From these figures quantum well absorption is not clearly seen for the samples 890920 and 890915. However, for 890915, it looks there is a little absorption peak at the desired wavelength i.e., at $\lambda=10.6\mu\text{m}$. The quantum well absorption peak for the sample 890901 was clearly seen in Fig. 3.9. The absorption of the sample 890921 has not been measured yet.

A series of photoconductivity measurements were performed using He-Ne and globar light sources with two different types of amplifiers. A He-Ne laser beam was chopped with a frequency of 1000 Hz and the output of the illuminated sample 890915 was measured using spectrum analyzer as well as oscilloscope and the results are shown in Figs. 3.10a-b respectively. In this measurement an EG&G PA-7 transimpedance amplifier was used and the sample was biased with a power supply. The response was purely due to across the band gap excitation of electrons in or within a diffusion length of the semiconductor depletion layer. In order to observe the response of the quantum well detector, a light source with maximum emission at $10.6\mu\text{m}$, the wavelength for which the detector is designed to respond, is essential. A globar light source can be used with an appropriate filter which can allow the

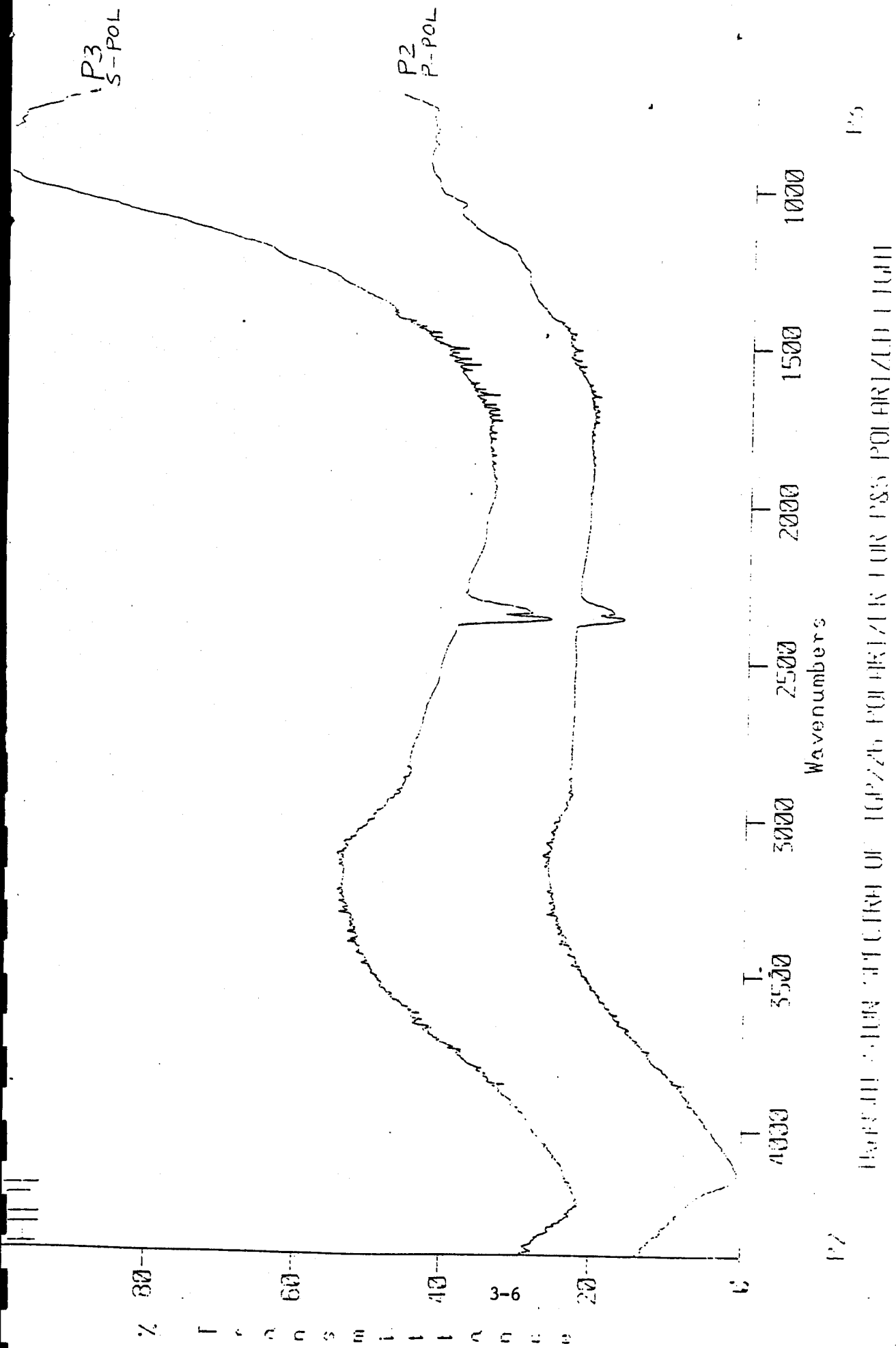
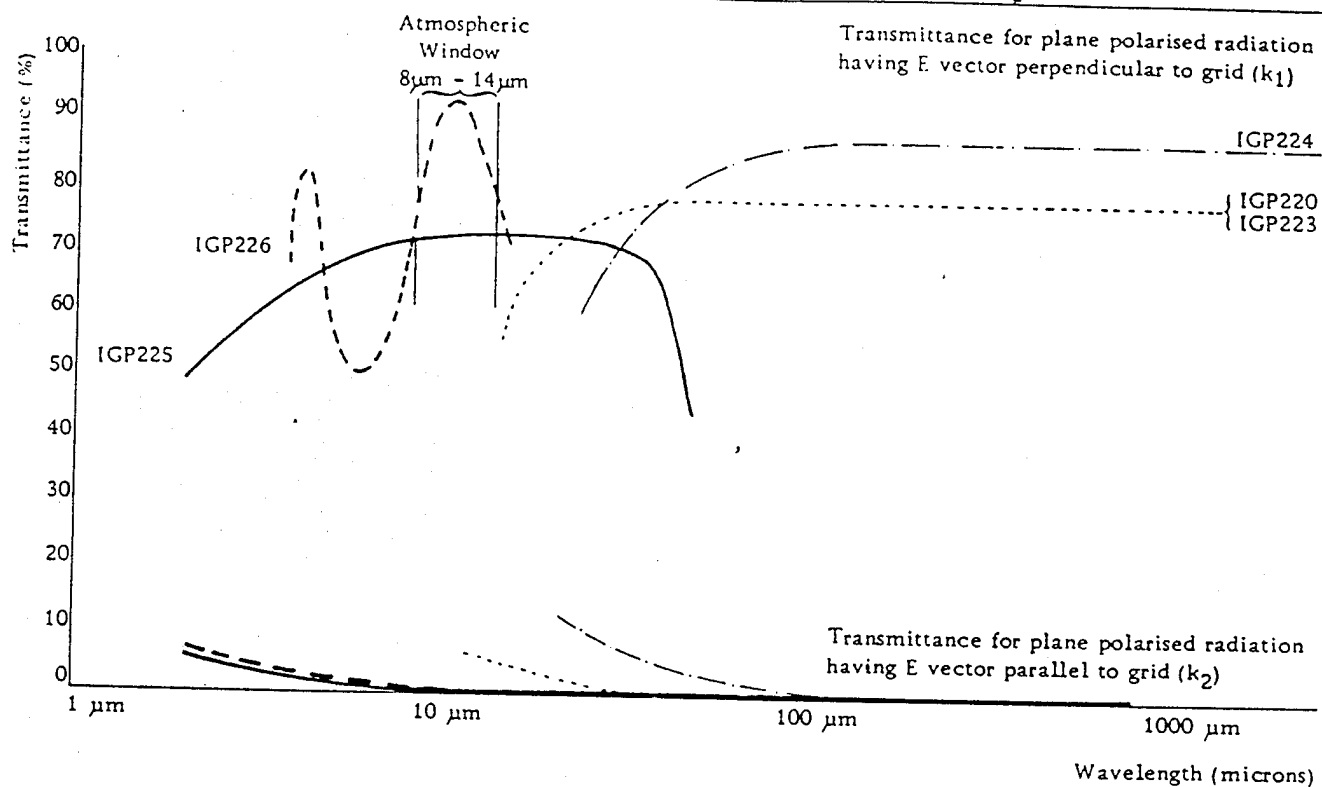


Fig. 3.4 Transmission Spectra with s and p Polarizations



Specification

IGP 225

Wavelength range

Transmission efficiency
Transmission of unwanted polarisation
Degree of polarisation

Power rating

Dimensions
Working aperture
Holder diameter
Holder thickness

2 microns to 35 microns

The upper wavelength is limited by an absorption band in the KRS-5 substrate
60-70%

4% at 3 microns, 0.25% at 10 microns

Better than 88% at 3 microns,
99% at 10 microns

10 watt per cm² for continuous use
40 watt per cm² maximum for short periods

25.4mm (1") diameter
41.3mm (1 $\frac{5}{8}$ ")
6.4mm ($\frac{1}{4}$ ")

IGP 226

Wavelength range

Transmission efficiency
Transmission of unwanted polarisation
Degree of polarisation
Power rating

Dimensions
Working aperture
Holder diameter
Holder thickness

8 microns to 14 microns

Typically 85% at 10 microns

0.25% at 10 microns

Better than 99% at 10 microns

10 watt per cm² for continuous use

40 watt per cm² maximum for short periods

25.4mm (1") diameter
41.3mm (1 $\frac{5}{8}$ ")
6.4mm ($\frac{1}{4}$ ")

Fig. 3.5 Polarizer Data

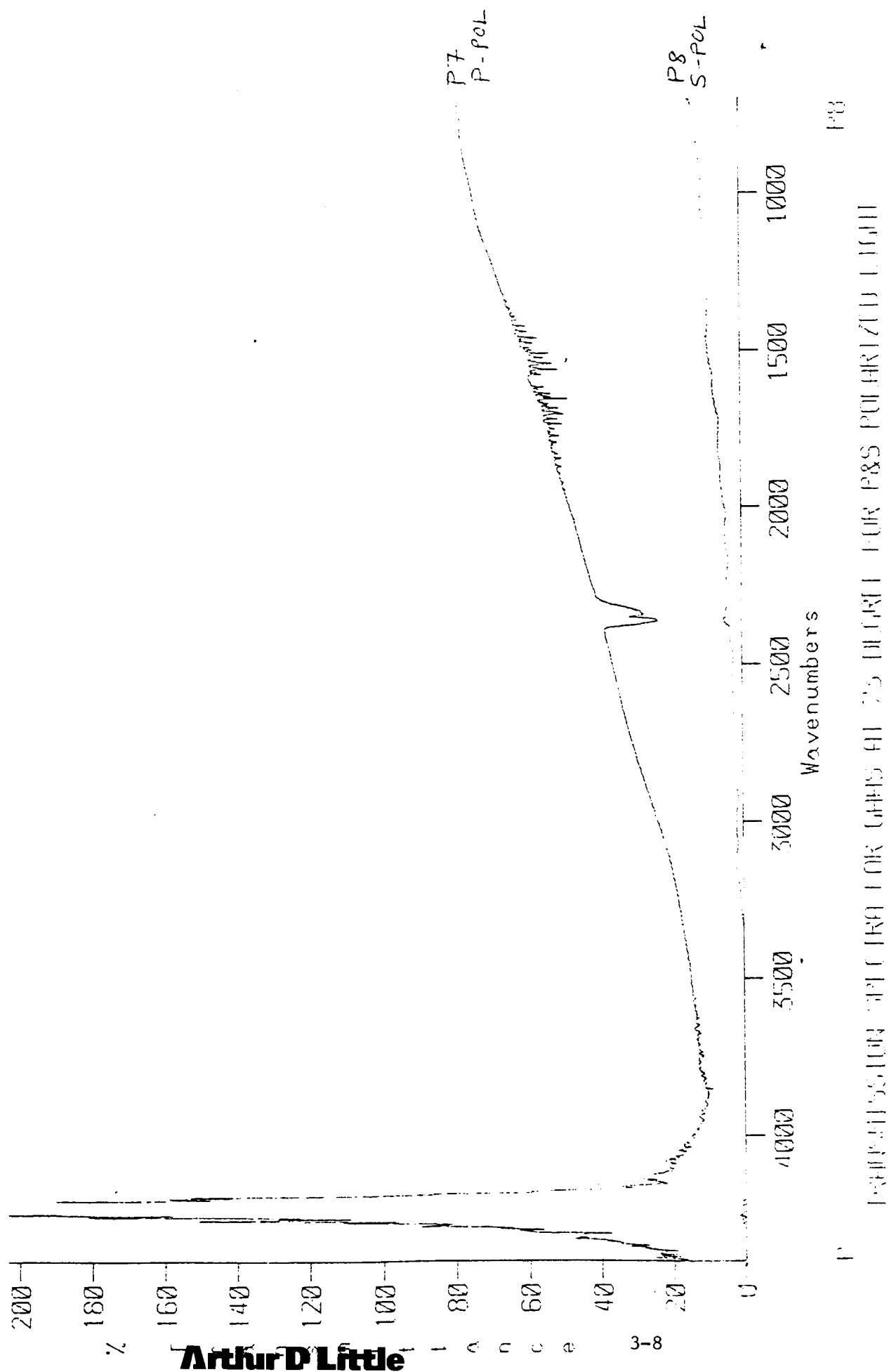


Fig. 3.6 Brewster Angle Transmission Measurements

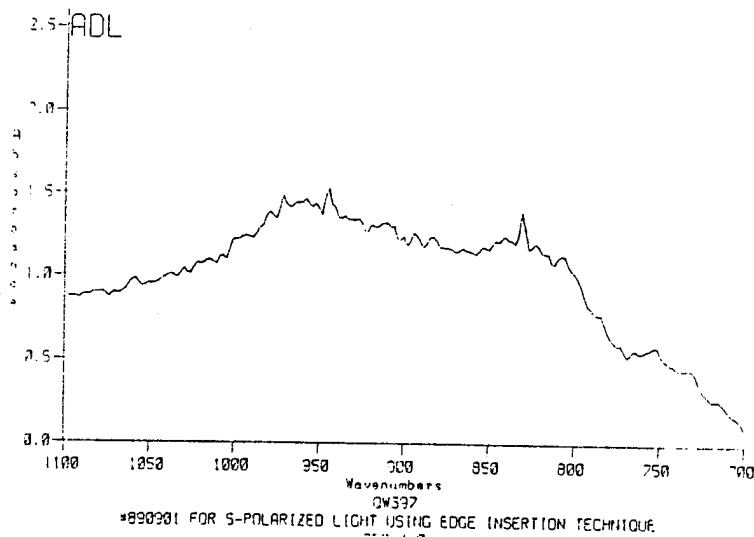
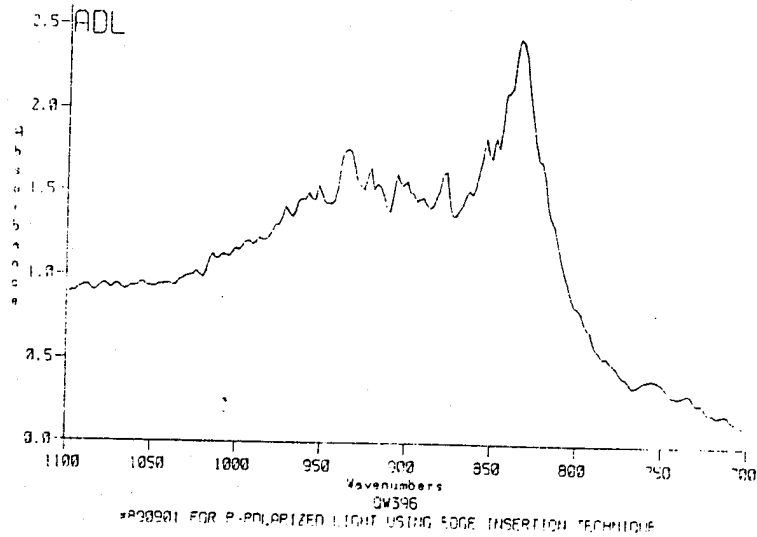
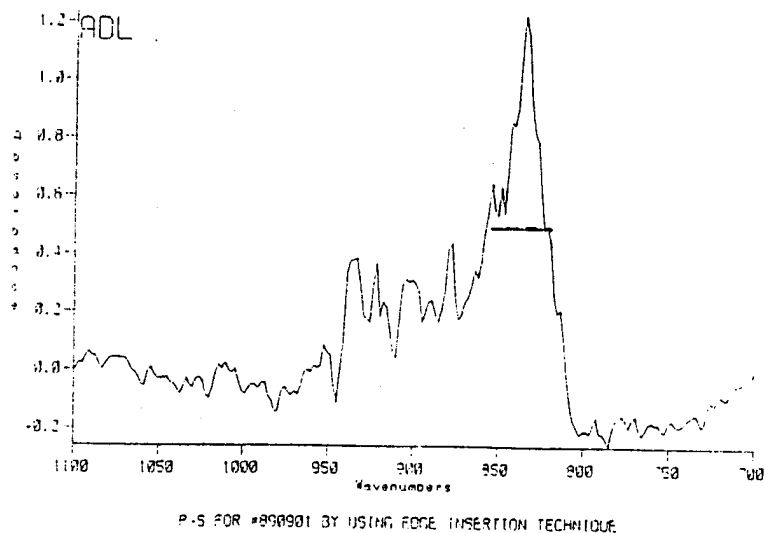


Fig. 3.7 Absorbance Calculated from p-s Polarizations for Sample #890901



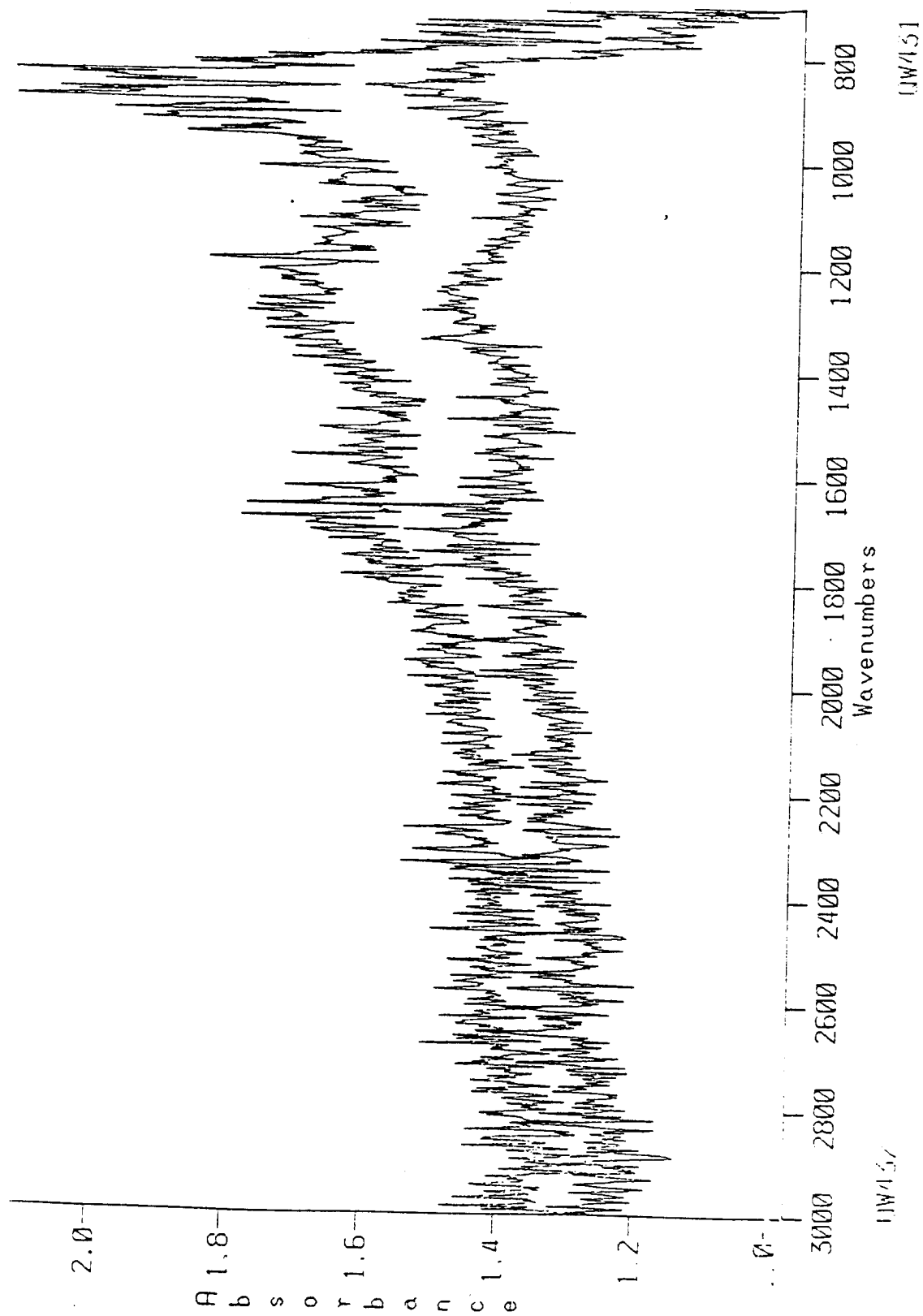


Fig. 3.8a,b Absorbance for p and s Polarizations for Sample #890915

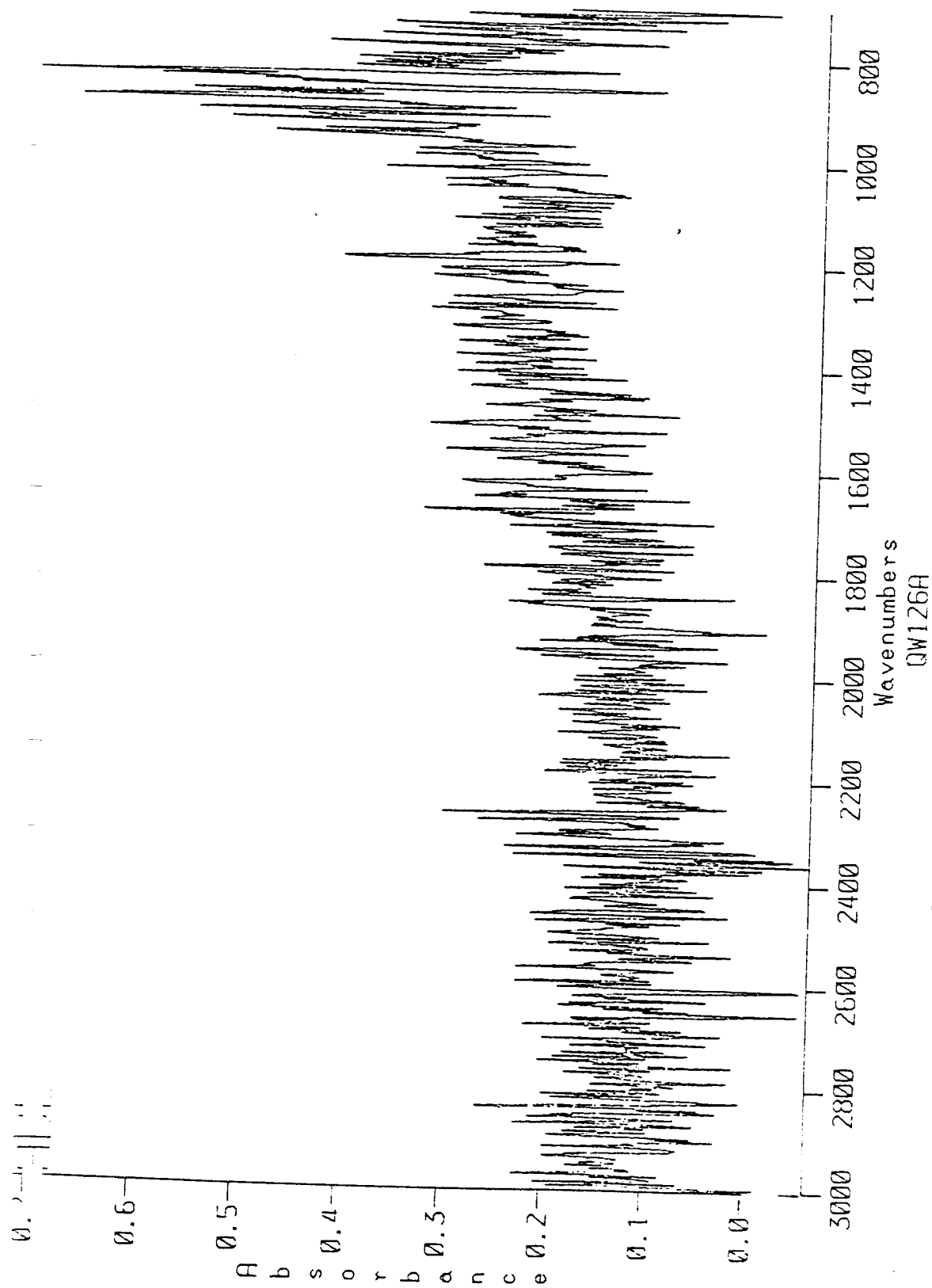


Fig. 3.8c Absorbance Calculated From p-s Polarizations for
Sample #890915
QW126A

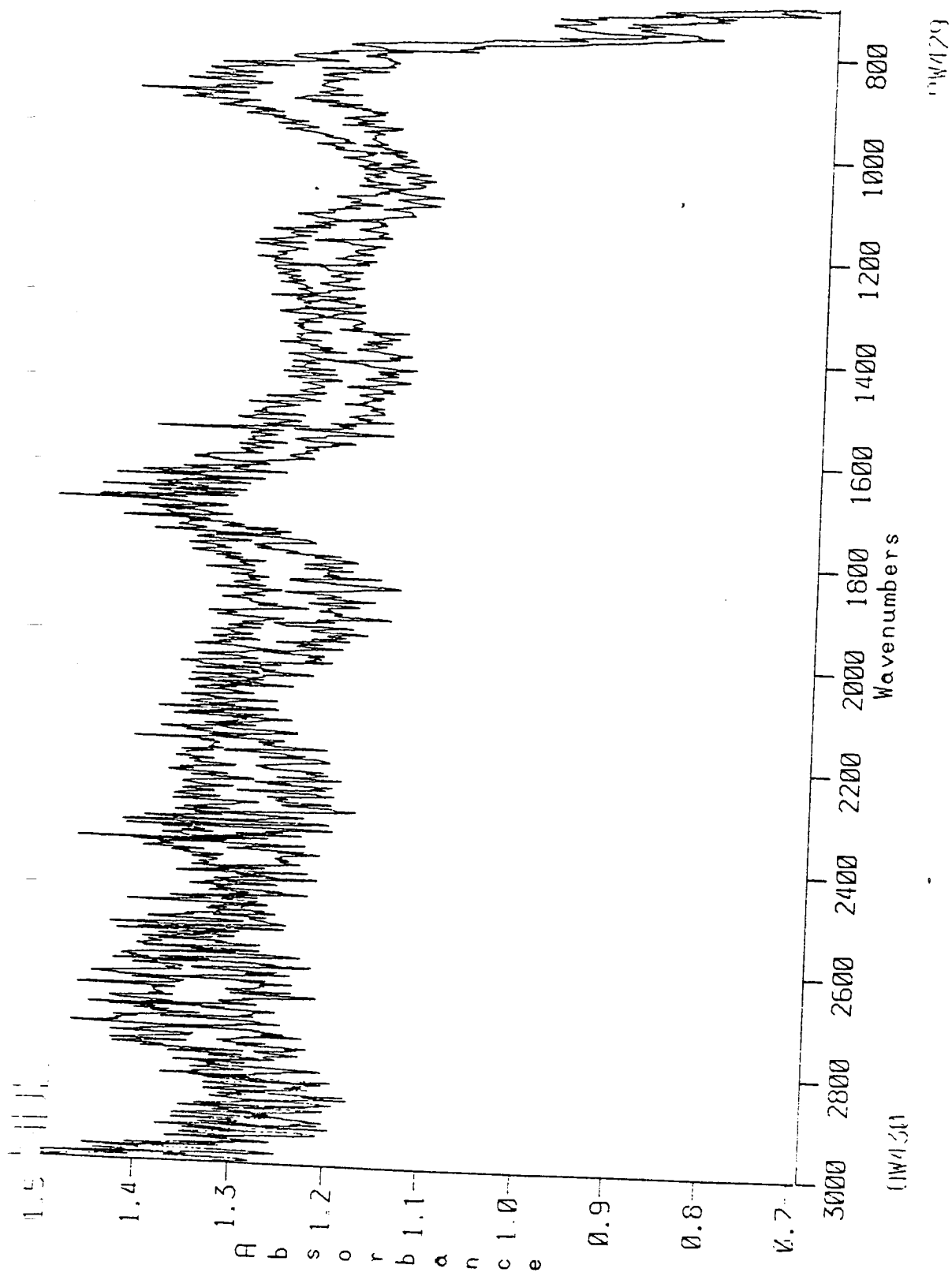


Fig. 3.9a Absorbance Spectra for Sample #890920

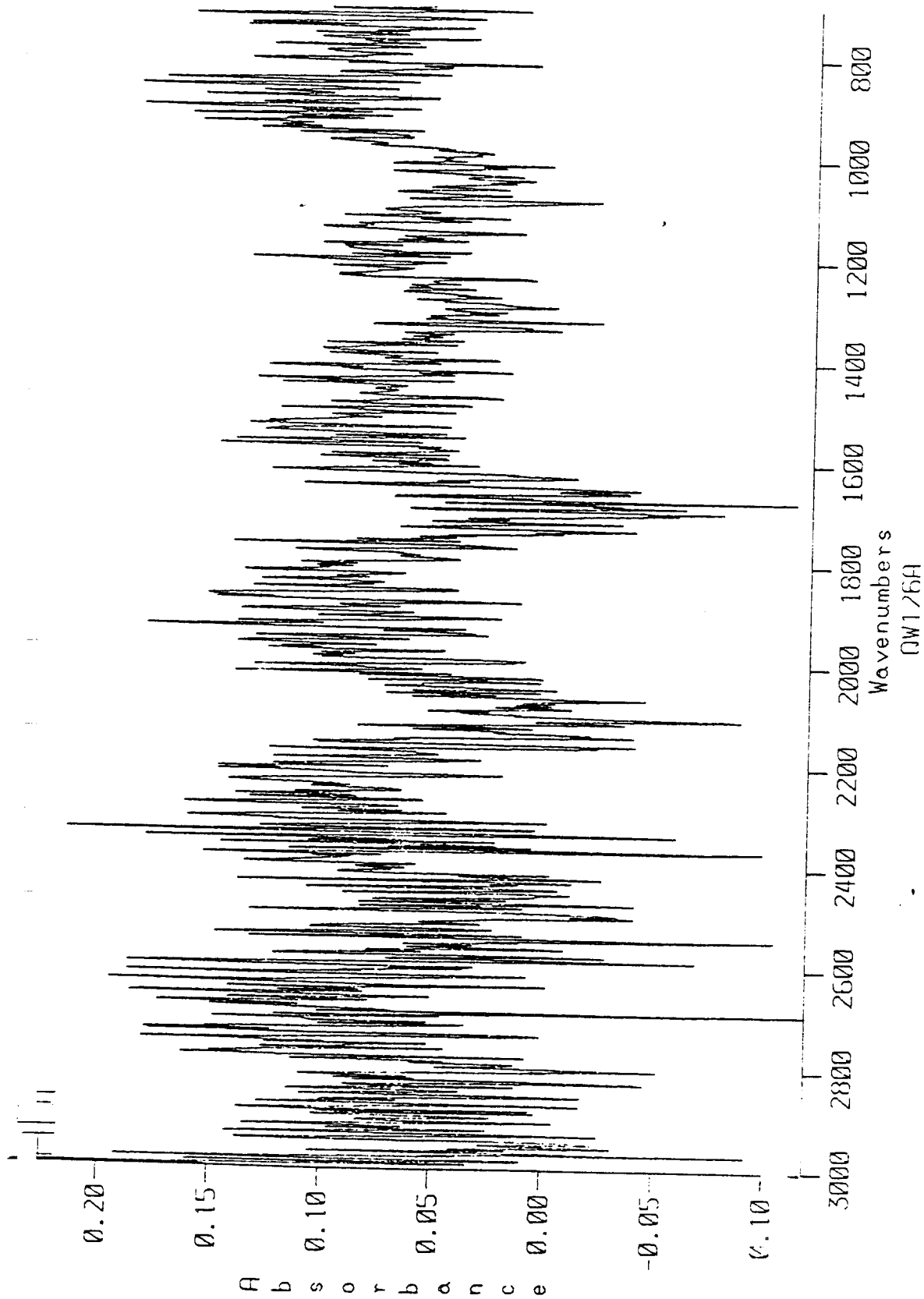


Fig. 3.9b Absorbance Spectra for Sample #890920

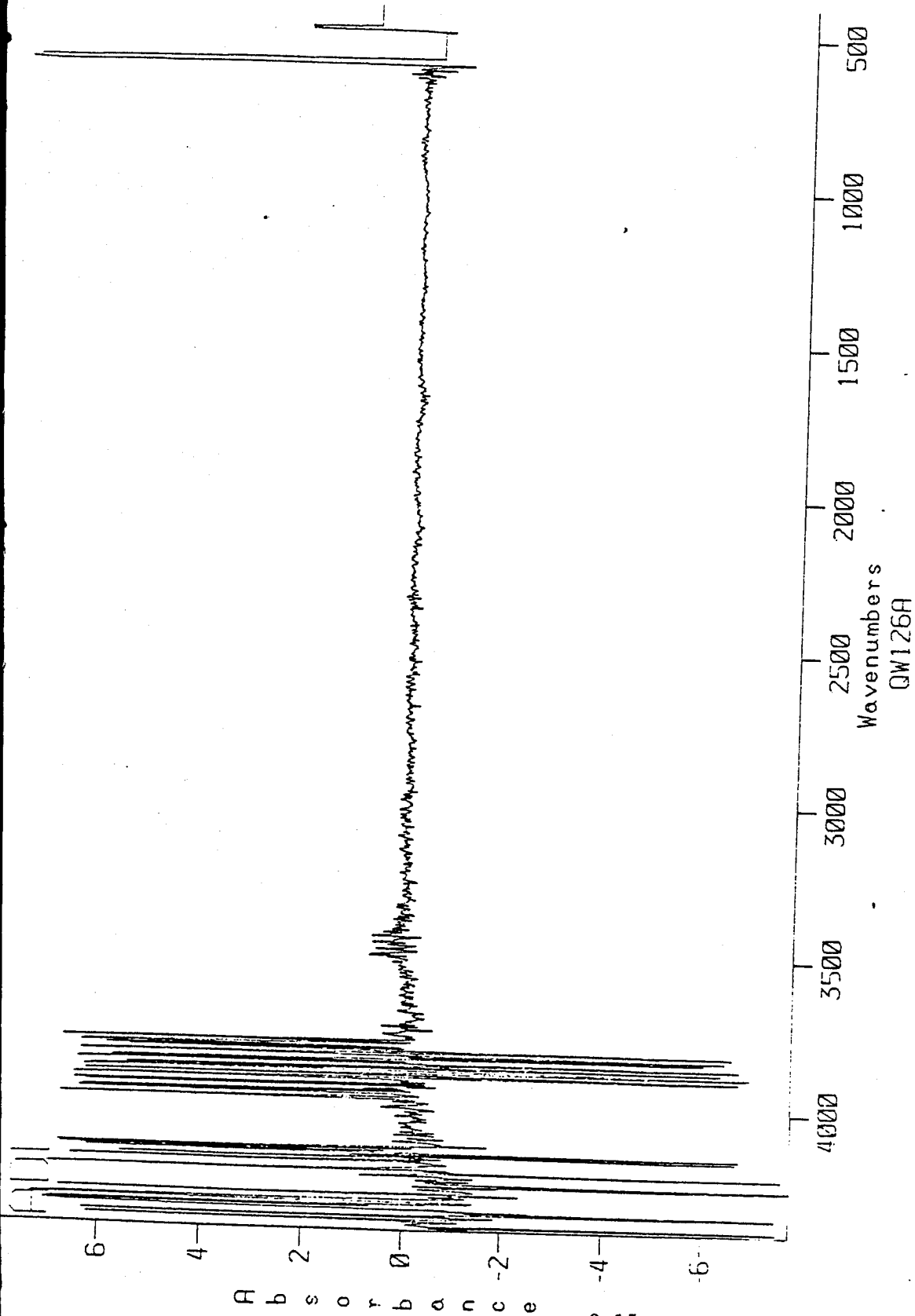


Fig. 3.9c Absorbance Spectra for Sample #890920

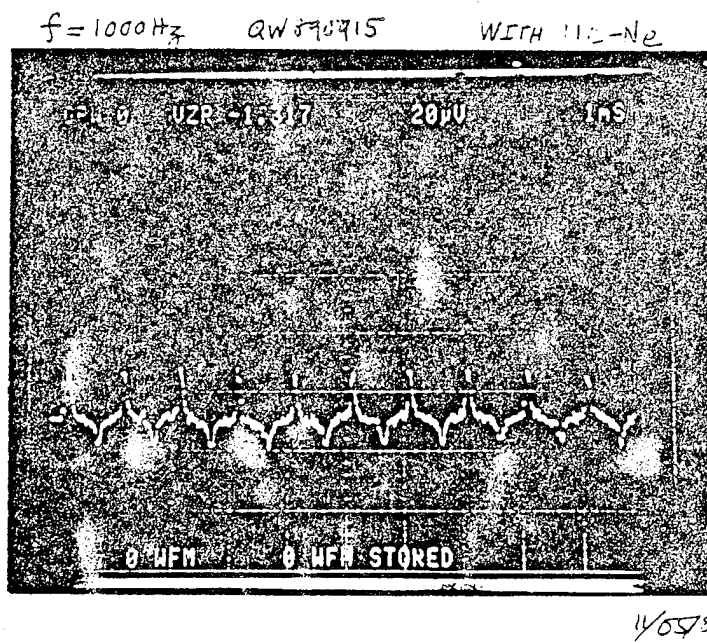
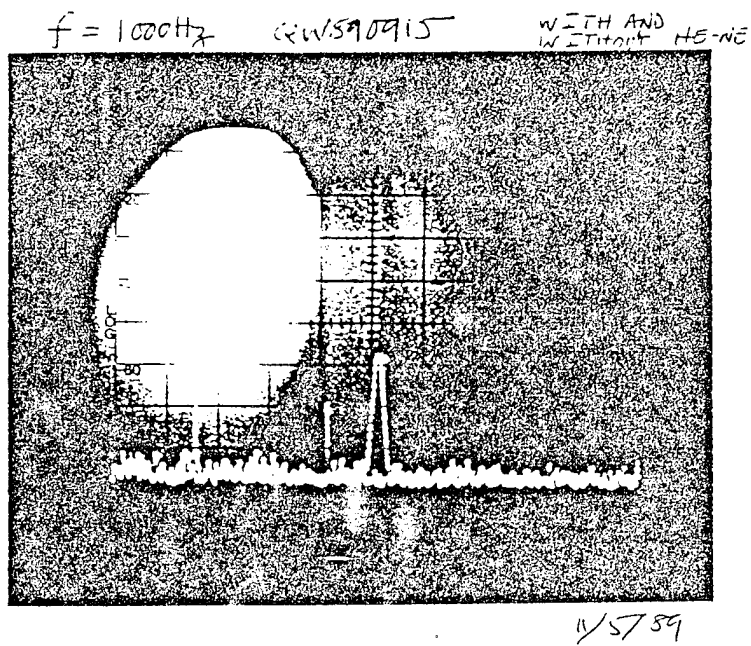


Fig. 3.10 Photoconductivity Observed With HeNe Laser at $f=1000\text{Hz}$ Chopping on #890915

light approximately from 8 μm to 12 μm . An attempt was made to filter the light with single crystal Si which allows light from 1.13 μm to the longer wavelength. Although this filter blocks the light which would create the electron-hole pairs, it does not completely preclude the photoemission of electrons which may be created in the metal side of the device. Indeed this happened to be the case as shown in Figs. 3.11a-c. Obviously, the amplitude of the signal with Si filter is decreased with relative to the one observed with the GaAs filter. When the polarity of the bias supply was reversed, the signal amplitude increased. We concluded that this is due to the same slight rectification effect as seen in Fig. 3.1. A similar experiment was carried out using EG&G PA-100 voltage gain amplifier. The frequency response of the amplifier was measured using a signal generator. The response of the amplifier is pretty flat in the frequency range of our interest. The output voltage as a function of frequency for the PA-100 amplifier is shown in Fig. 3.12. The frequency response of the 890920 sample was measured also measured with the same amplifier. The results are shown in Figs. 3.13a-g. In Fig. 3.14, the modulated output voltage is plotted as a function of chopping frequency. In Fig. 3.14, it seems that the detector has a long true constant which may be due to the unwanted traps existing in the sample. A similar experiment was also done for HgCdTe detector without using any optical filters. The result is shown in Fig. 3.15. Unlike the 890920 detector, HgCdTe detector is fairly independent of frequency. The bias dependent response of the 890920 detector using PA-100 amplifier is shown in Figs. 3.16a-c and in Fig. 3.17, bias current vs. modulated output is plotted. From Fig. 3.17, it seems a suitable bias resistor may increase the signal level substantially from the existing bias condition which is 27 $\text{K}\Omega$. Finally, an attempt was made to see the response of the carriers of the quantum well using IGP-226 polarizer. Unfortunately a signal was observed for both the polarizations and this indicates, i) some transmission of light in the shorter wavelengths through the polarizer and ii) the signal is overwhelmed by the other effects such as across the band gap photoconductivity.

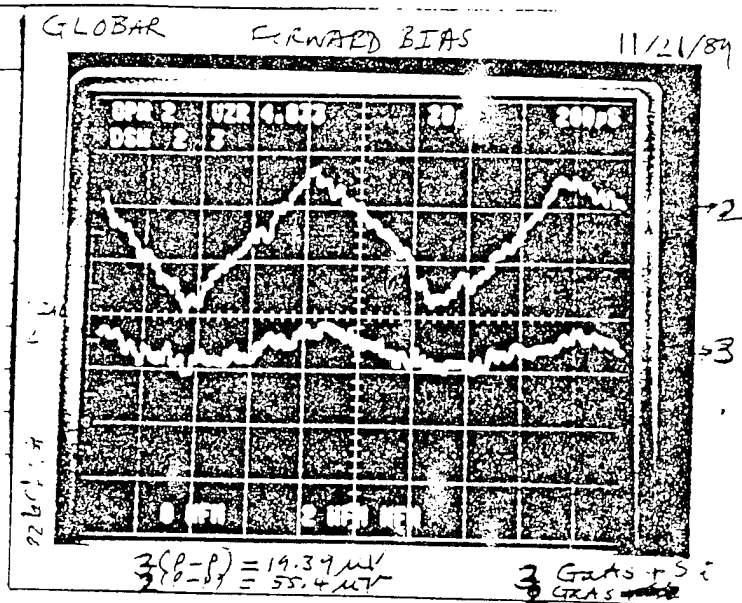
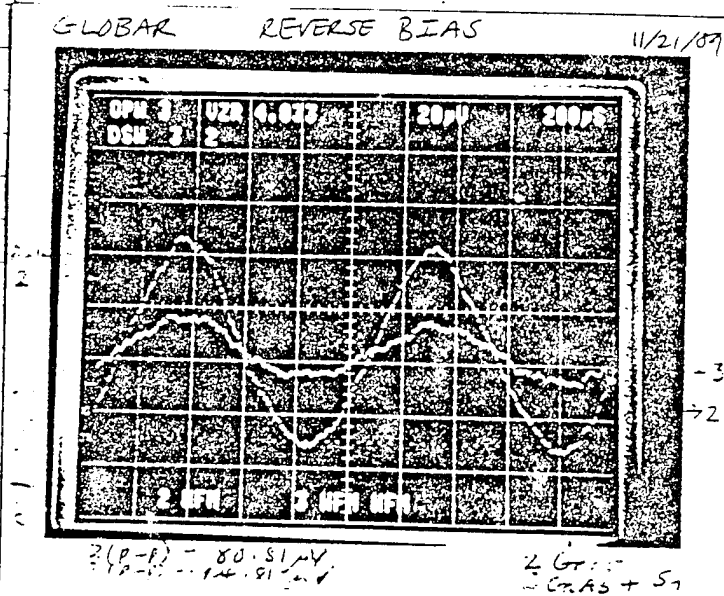
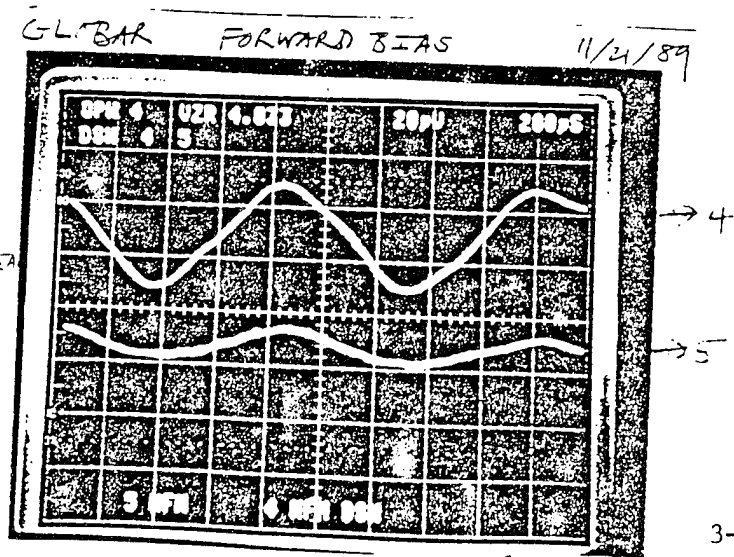


Fig. 11 - a



(b)

Fig. 3.11 Photoconductivity Observed Through a Si Filter Which Rules Out Across the Gap Photoconduction



(c)

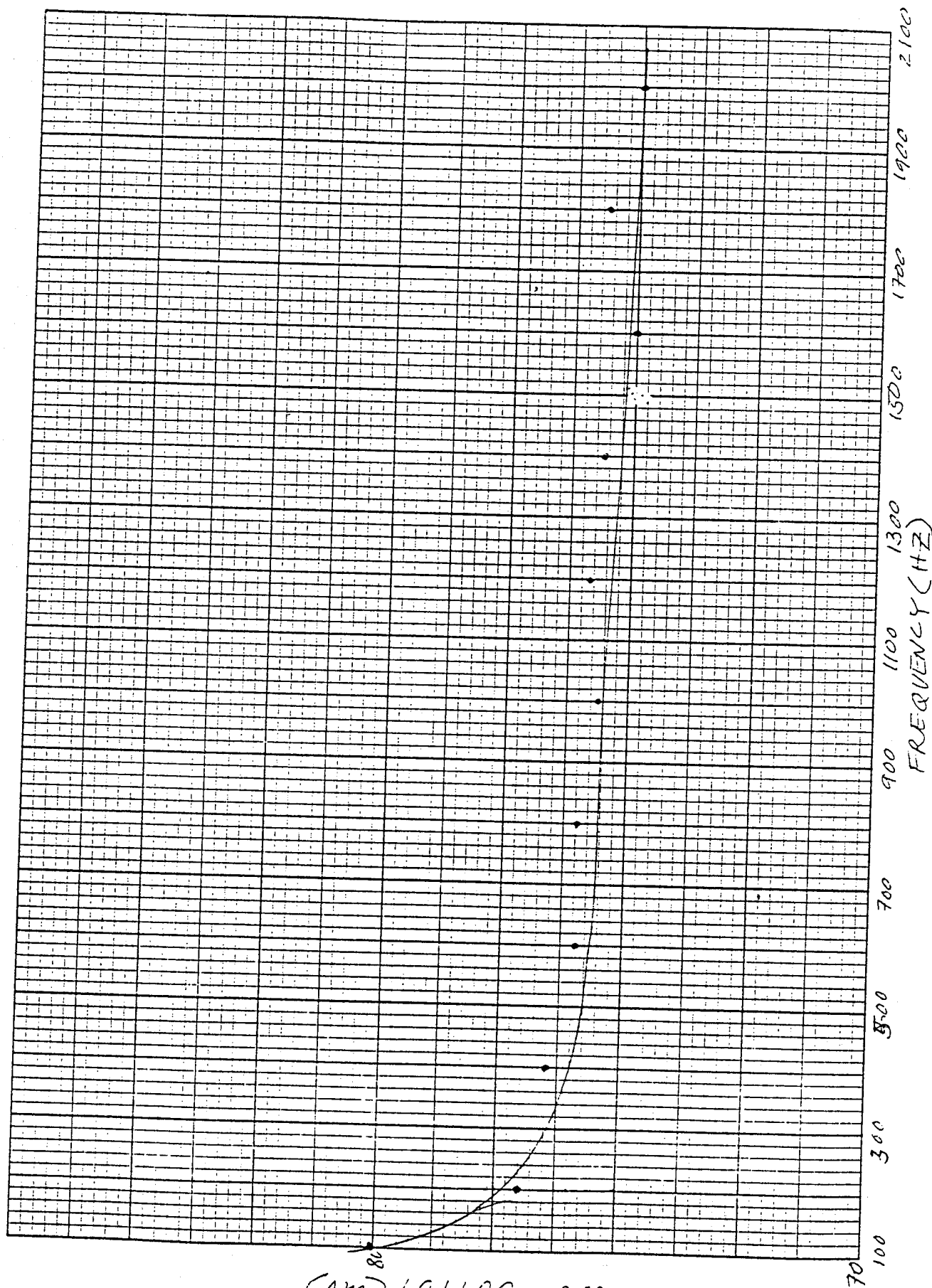
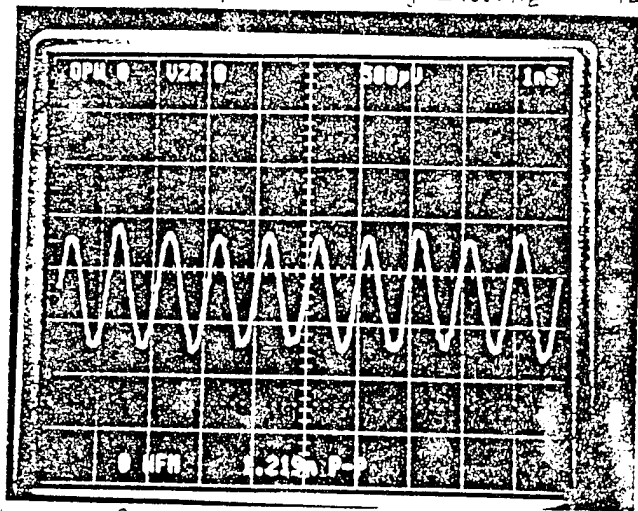


Fig. 3.12 Output on mV versus Chopping Frequency

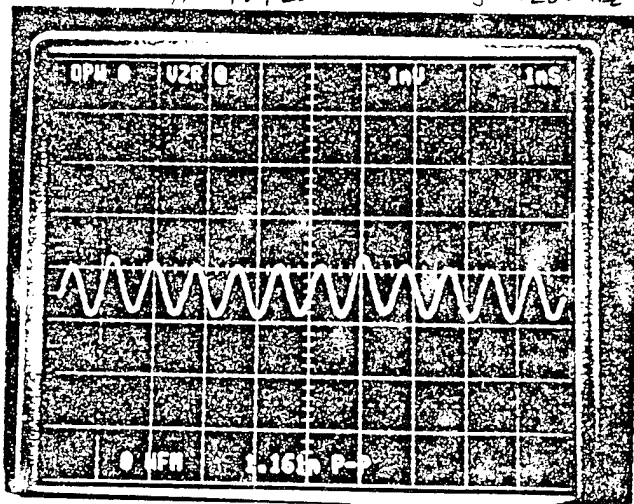
#890920 $f = 1000 \text{ Hz}$ 12/01/8



PA-100 $R_B = 27 \text{ K}\Omega$

Fig. 13-d

#890920 $f = 1200 \text{ Hz}$



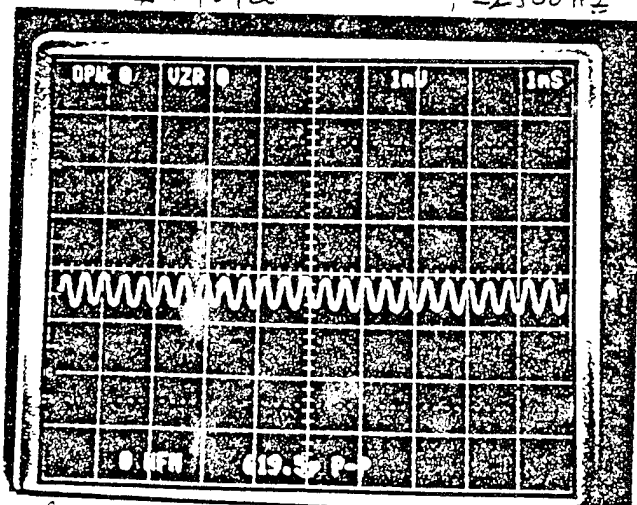
PA-100

$R_B = 27 \text{ K}\Omega$

12/01

Fig. 13-e

#890920 $f = 2500 \text{ Hz}$



PA-100

$R_B = 27 \text{ K}\Omega$

12/01

Fig. 13-f

Fig. 3.13d,e,f Voltage Output versus Frequency Observed on #890920

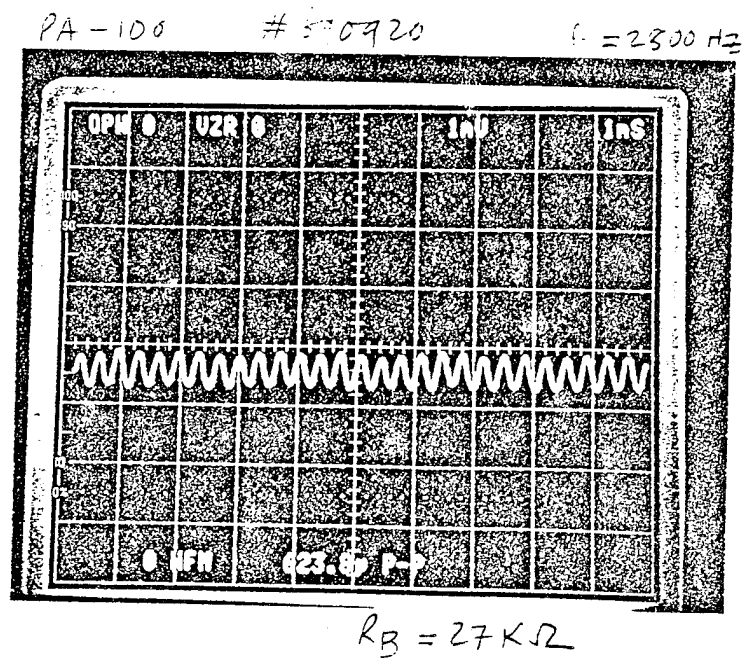


FIG. 13-g

Fig. 3.13g Voltage Output versus Frequency Observed on #890920

SAMPLE # 890720
WITH PA-100

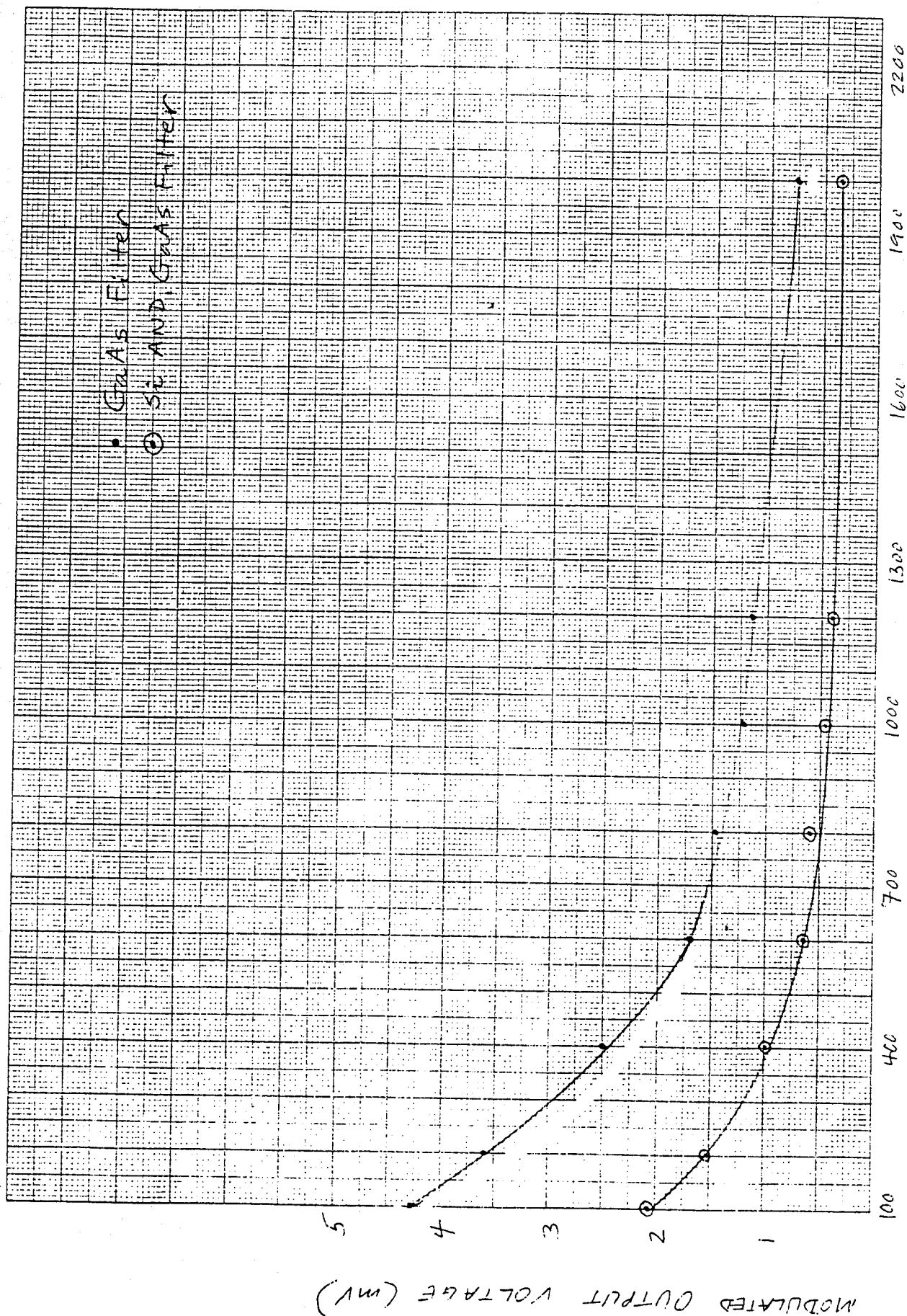


Fig. 3.14 Output in mV versus Chopping Frequency with Different Filters for #890920

With PA-100

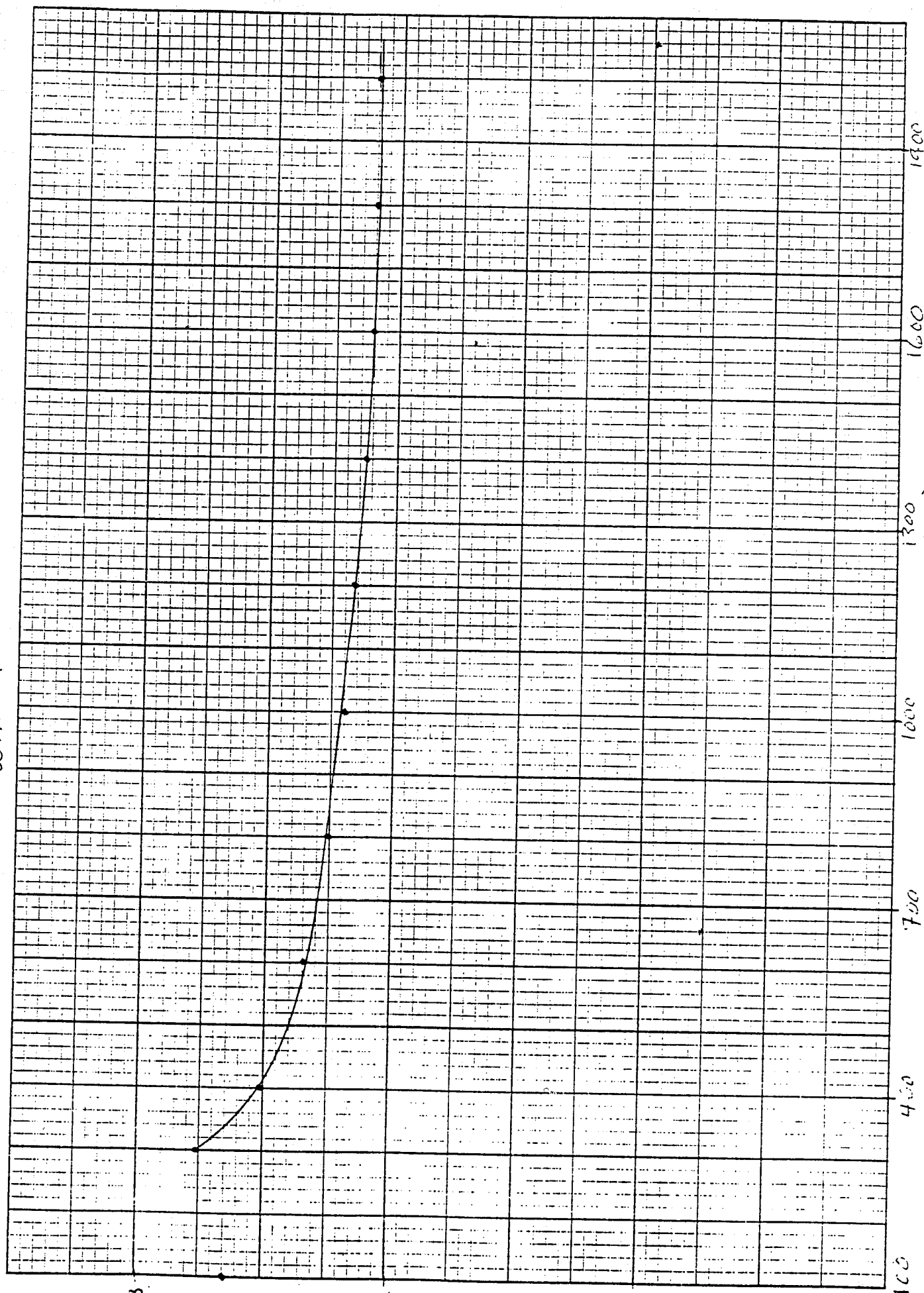


Fig. 3.15 Output in V versus Chopping Frequency for HgCdTe Detector

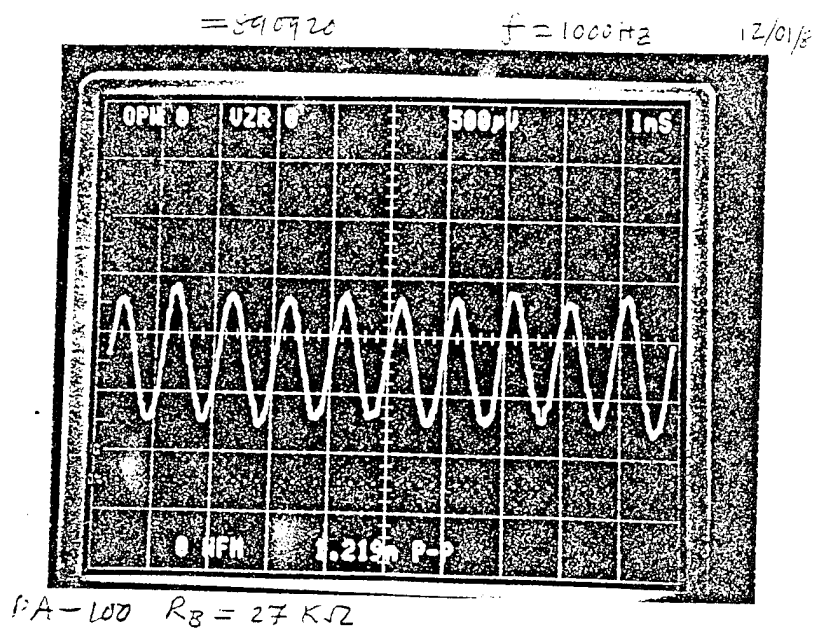


FIG. 16-a

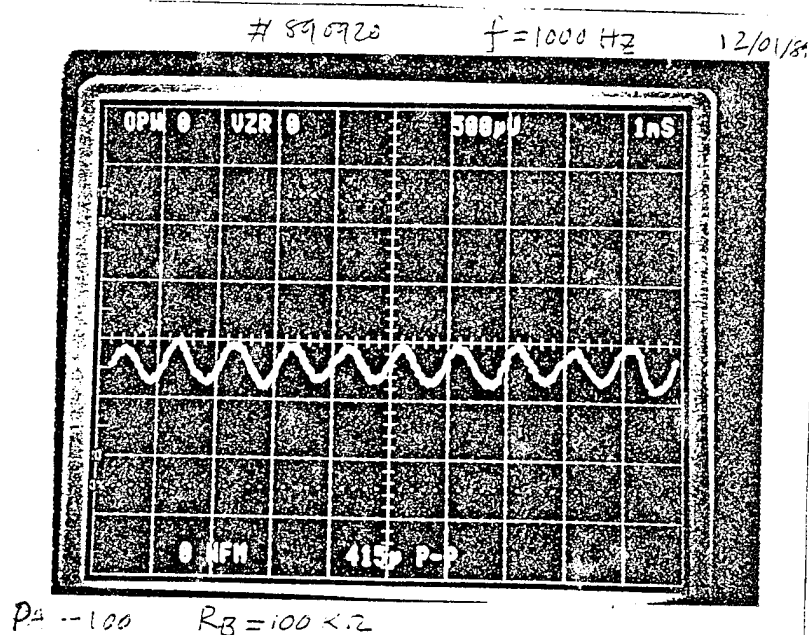


FIG. 16-b

Fig. 3.16a,b Modulated Output versus Bias Current for #890920

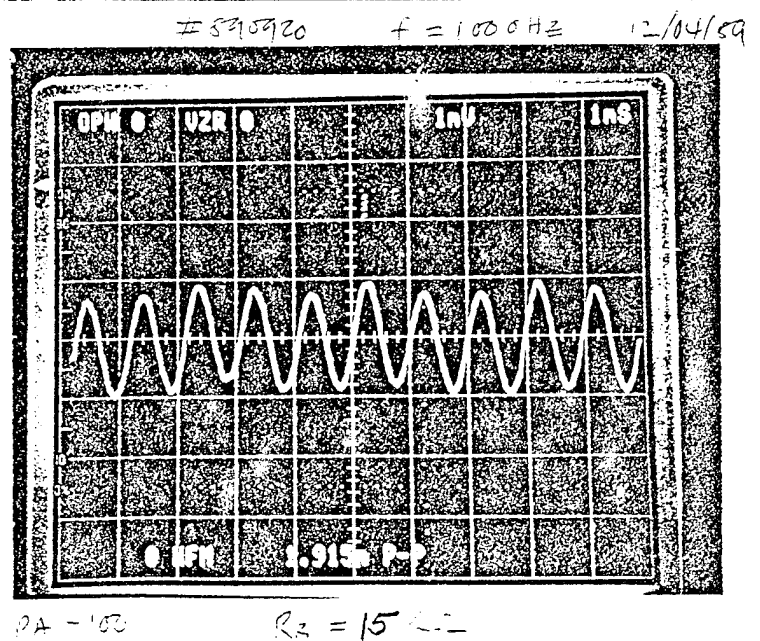


FIG. 16-C

Fig. 3.16c Modulated Output versus Bias Current for #890920

666 PA-100
HOPPING FREQUENCY: 1000 Hz
SAMPLE # 890920

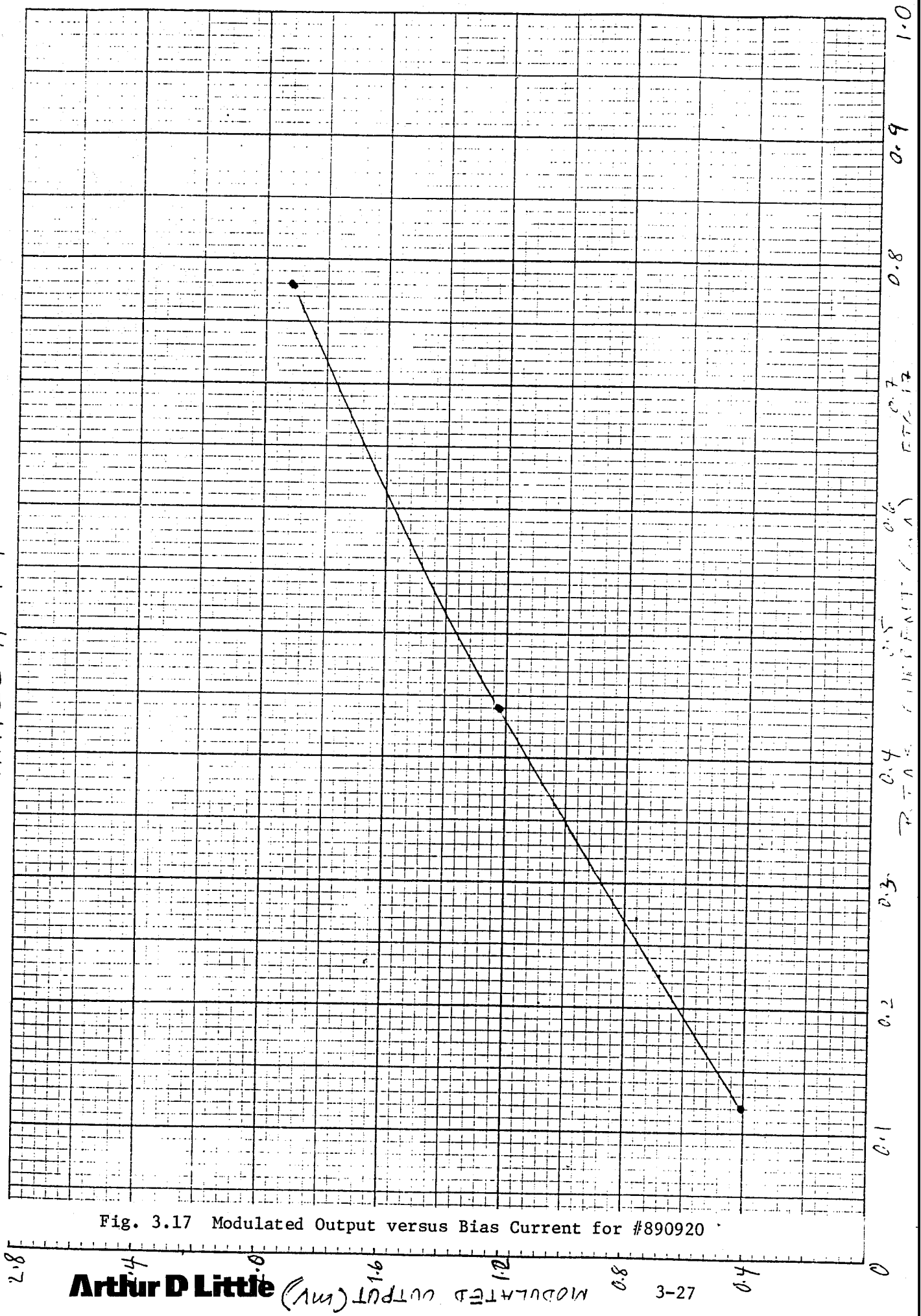


Fig. 3.17 Modulated Output versus Bias Current for #890920

Based on all of the measurement reported so far it was obvious that a high pass optical filter at 8 μm was necessary. The blockage of the shorter wavelengths will ensure that the signal is not coming from the competing effects as mentioned earlier.

A high pass filter of one inch diameter was acquired from "Optical Filter Corp.," Mass. The transmission characteristics of this filter is shown in Fig. 3.18. The specifications of the filter is such that From this figure one can see that the transmission of light is only 0.1% from 6.67 μm to down to visible. With this filter a series of experiments have been conducted on the samples 890915, 890920 and 890921. The very first test experiment was performed on the sample #890920 using broad band Globar light source chopped at the frequency of 100 Hz, keeping the detector at room temperature and no modulation was observed. On the same sample, with same chopping frequency but the detector at 77 K, two experiments were performed, one with cutoff filter and the other without any filter. In both of these experiments modulated signal have been observed. The ratio of these signals is about 854. The results of these experiments are shown in Figs. 3.19a-b. The results of these experiments tells us that the contribution of the signal is mostly from the visible part of the spectrum and this may be due to photovoltaic and internal photoemission effects. A small fraction of the signal which may be contributed from the longer wavelength should show the polarization dependence if the signal is indeed purely due to carriers generated from the quantum wells. In reality no such dependence was observed. The results of these experiments are shown in Fig. 3.20. Also, the power incident on the detector was measured to be the same for both polarizations using thermopile detector.

A similar investigation was made on the sample #890921. The results of this sample show quite different behavior than the samples tested before. The experiments which were conducted on the sample #890921 are summarized as follows:

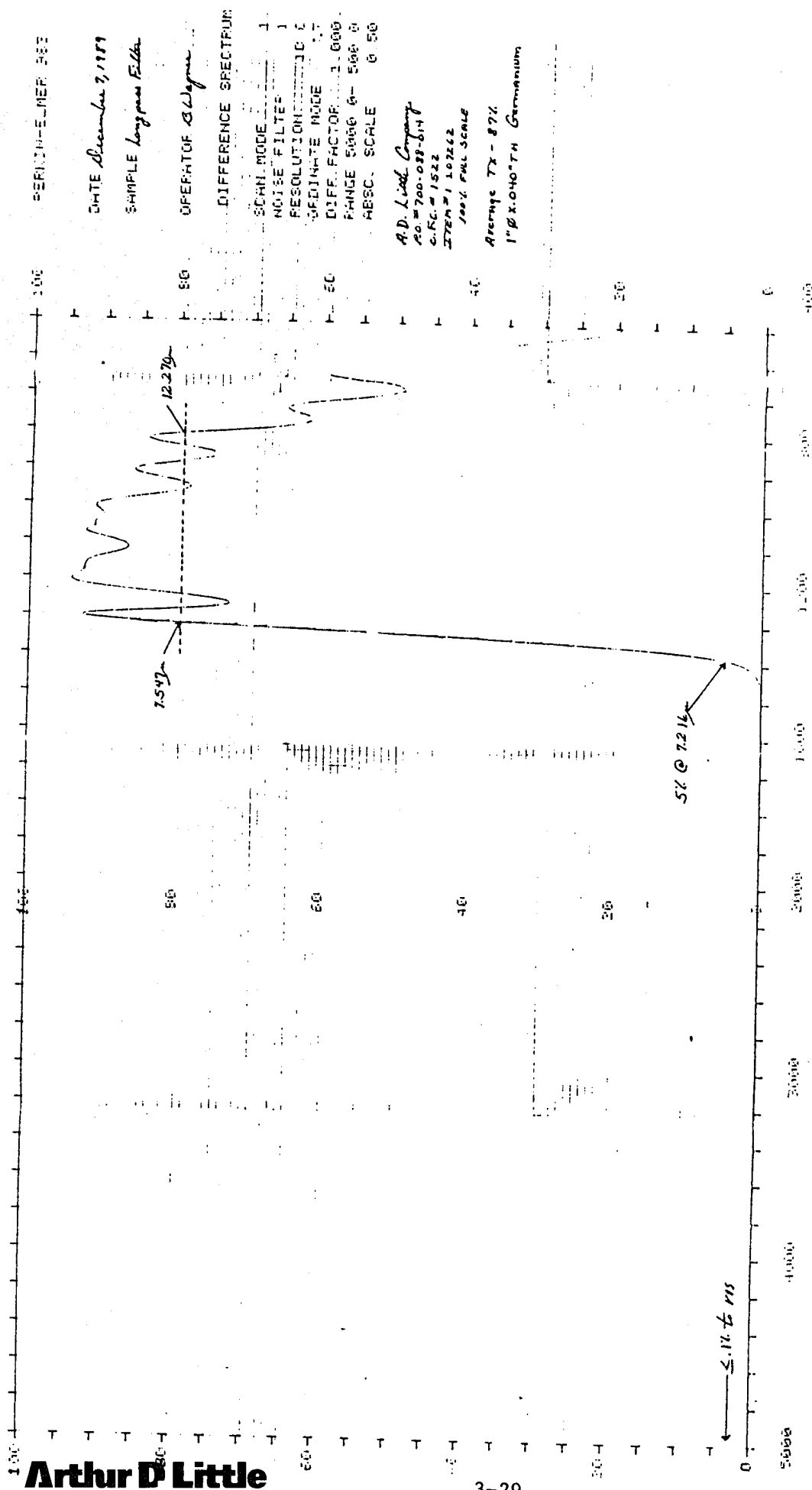


Fig. 3.18 Transmission Characteristics of the High Pass Filter Used in Detectivity Measurement

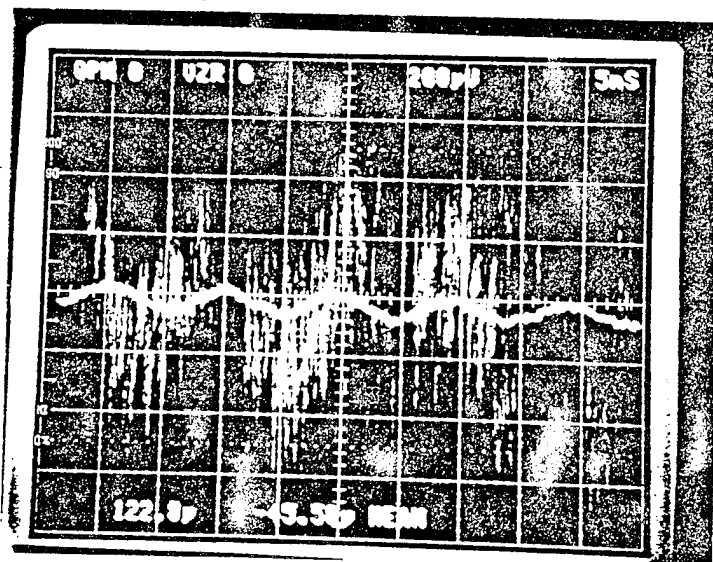
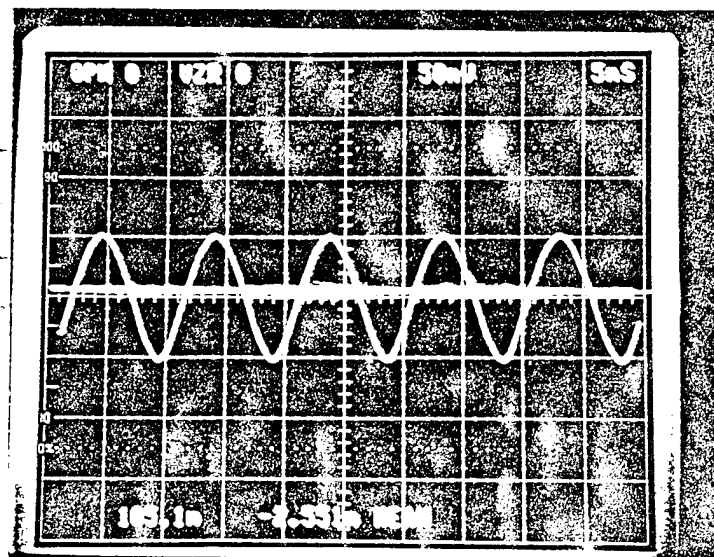


Fig. 3.19 Modulated Output With and Without Filter

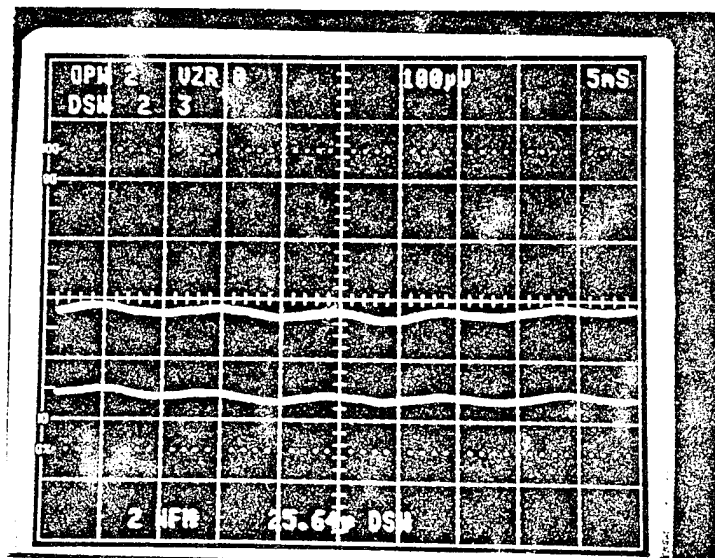


Fig. 3.20 Approximately Equal s and p responses .

TABLE 3.1

Run #	Bias Voltage	Cutoff Filter	Polarizer	Signal (p-p)
1	12.85	No	No	64.77 mV
2	12.85	Yes	No	679.60 μ V
3	5.50	Yes	Yes(p)	128.20 μ V
4	5.50	Yes	Yes(s)	100.70 μ V
5	5.52	No	No	29.20 mV
6	5.52	Yes	No	452.3 mV
11	5.50	Yes	Yes(p)	143.0 μ V
12	5.50	Yes	Yes(s)	97.42 μ V
17	7.55	Yes	Yes(p)	122.40 μ V
18	7.55	Yes	Yes(s)	76.05 μ V

By analyzing the above results one can easily see that the ratio of first two runs is only 95.31, whereas for the sample #890920 it was 854. This drop in ratio definitely indicates that the contribution of the signal is not limited in the region where filter cuts the light to 0.1%. Also, from the runs #5 and #6 one can see that the ratio has even further dropped to 64.56 because of different bias condition. This bias dependent ratio indicates that there are more than one component to this signal.

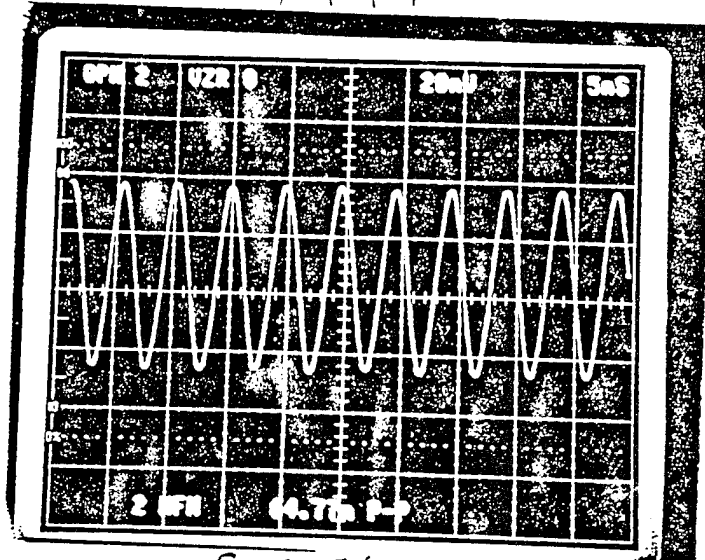
One of the components of this signal is very much dependent on the bias condition and which probable the photovoltaic effect. The other component is less sensitive to bias condition and unless it comes from the spectral region where cutoff filter allows light to pass through, the ratio cannot drop to such a small number. Also, there is clearly a change was observed due to two different polarizations. The difference spectra for runs #17 and #18 show clearly the effects of polarizations. The experimental results of the above mentioned runs are shown in Figs. 21-30. Also, in Figs. 31-32, the difference spectra for runs #17 and #18 are shown.

The detectivity (D^*) was calculated based on the results produced in Fig. 27. The power received by the detector was measured using NBS traceable thermopile detector through the cutoff filter and the polarizer. The voltage output of the thermopile detector for the p-polarized light was 729.7 μV . Sensitivity of the thermopile detector at 10.0 μm wavelength is 7.9 V/W as provided by the manufacturer. Power received by the thermopile detector is then given by

$$P = (729.7 \times 10^{-6}\text{V}) / (7.9 \text{ V/W}) = 92.37 \mu\text{W}$$

Thermopile has the area $1 \times 10^{-2} \text{ cm}^2$ and therefore the power density is $92.37 \times 10^{-8} \text{ W/cm}^2$.

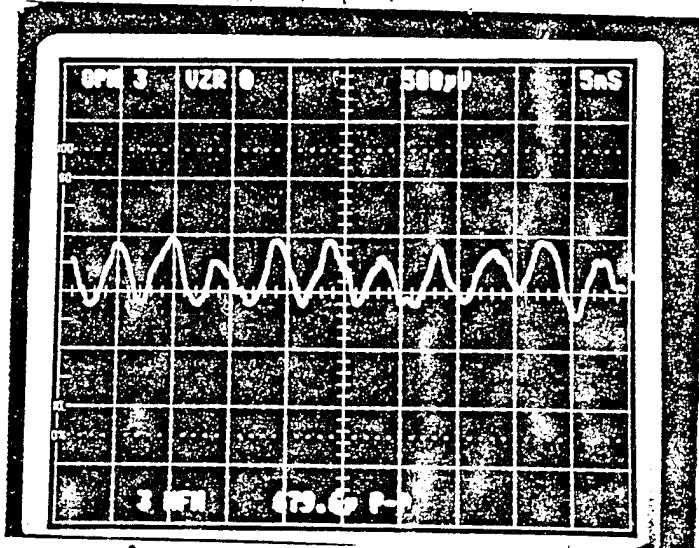
N0.1 #890921



$$f = 205 \text{ Hz}$$

FIG. 21

N0.2 #890921



$$f = 205 \text{ Hz}$$

FIG. 22

N0.3 #890921

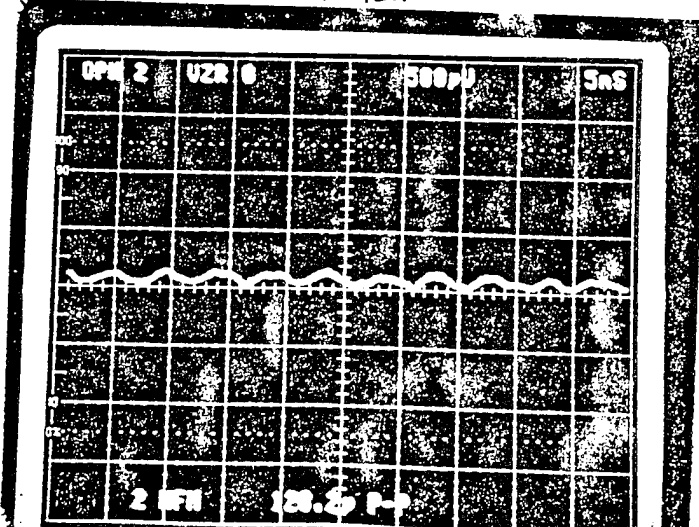
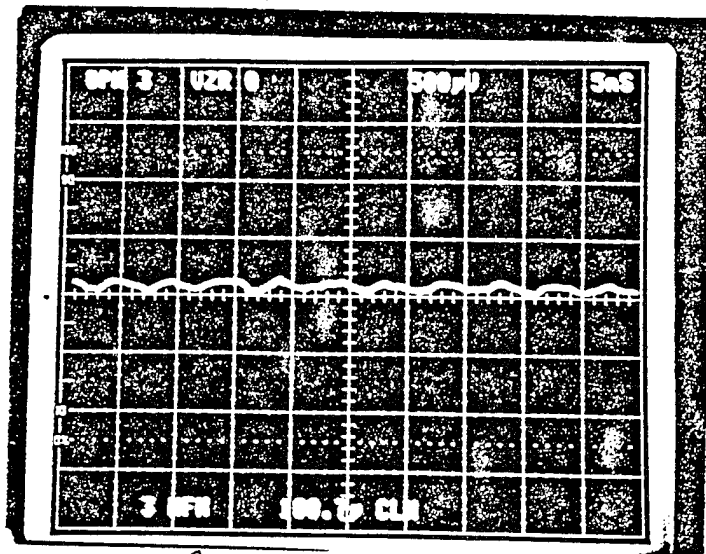


FIG. 23

NO. 4

#890921

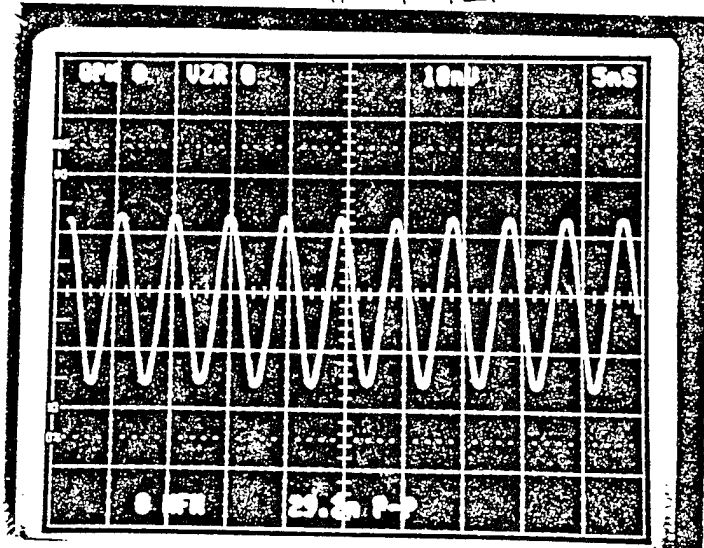


$f = 205 \text{ Hz}$

FIG. 24

NO. 5

#890921



$f = 200 \text{ Hz}$

FIG. 25

NO. 6

#890921

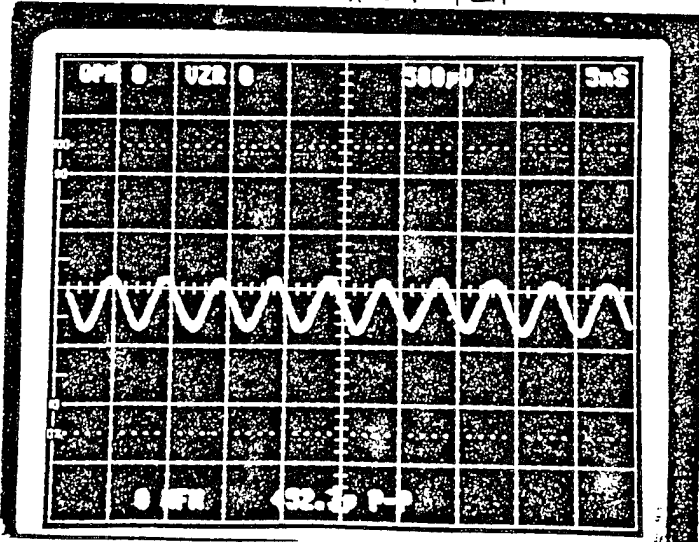


FIG. 26

NO. 11

890921

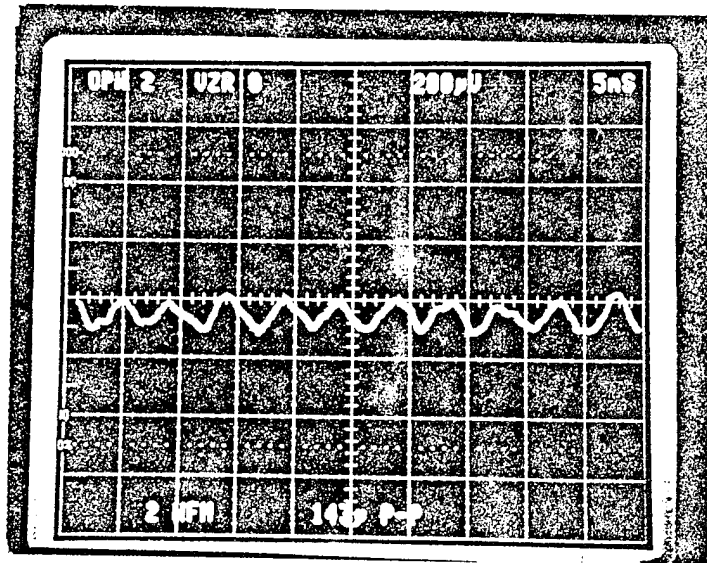


FIG. 27

NO. 12

890921

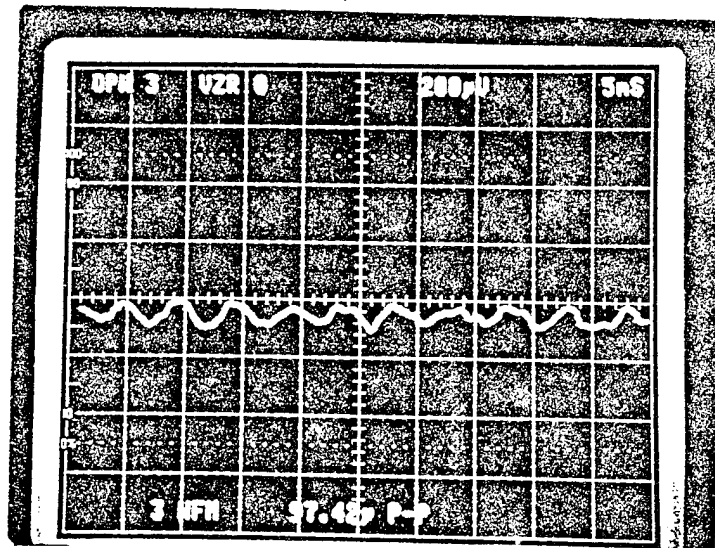


FIG. 28

NO. 11 - NO. 12

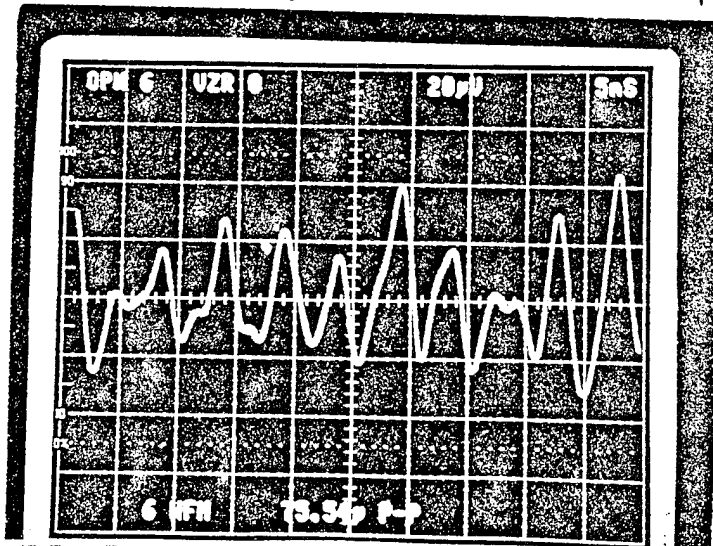


FIG. 31

NO. 17

#890921

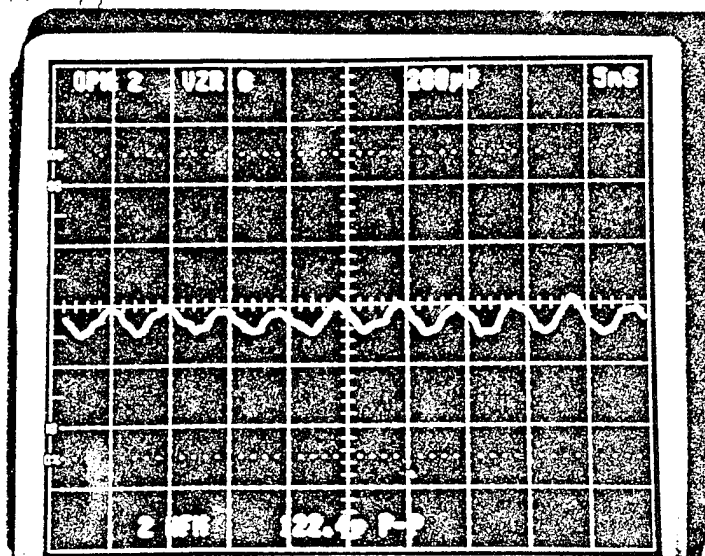


FIG. 29

Fig. 3.29 p-Polarization Response for #890921

NO. 18

#890921

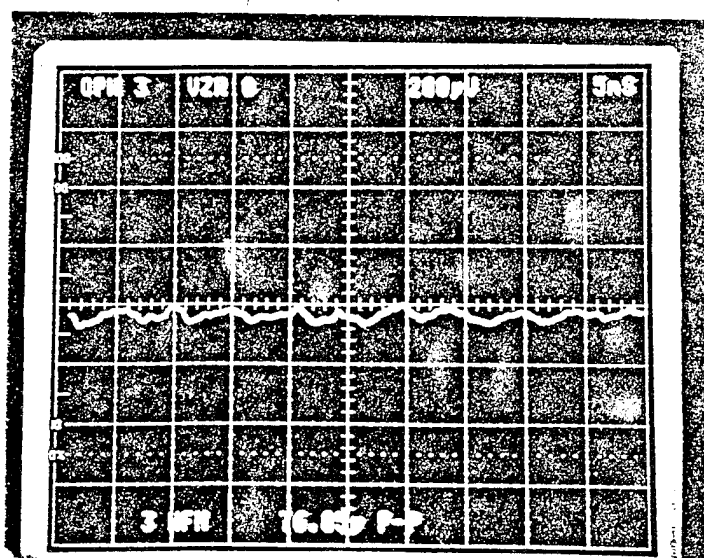
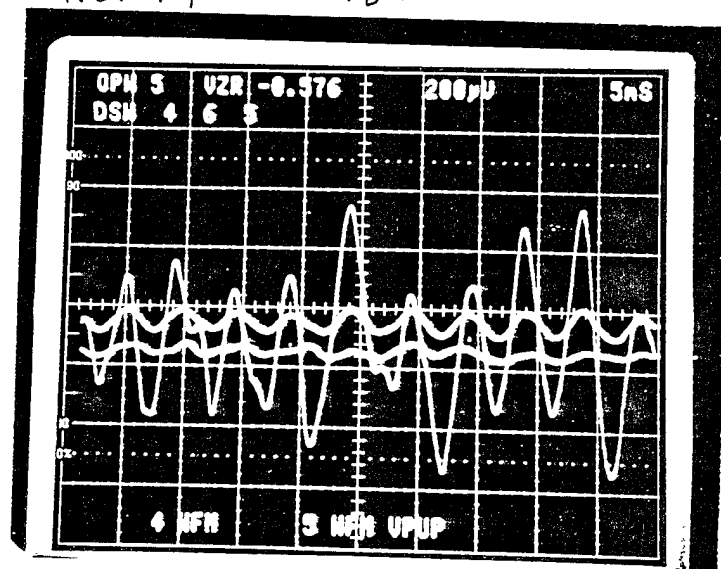


FIG. 30

Fig. 3.30 s-Polarization Response for #890921

NO. 17 - NO. 18



$$f = 20 \text{ Hz}$$

Fig. 3.31 p-s Response Difference for #390921

Power received by the quantum well detector can be calculated, multiplying the power density by the area of the multiquantum well detector and is given by:

$$P = (92.37 \times 10^{-4} \text{ W/cm}^2) (7.62 \times 10^{-5} \text{ cm}^2) = 703.86 \times 10^{-9} \text{ W}.$$

the r.m.s. voltage measured by the quantum well detector from Fig. 27 is given by

$$V_{\text{r.m.s.}} = (63.46 \text{ } \mu\text{V})/10^5/388 = 2.46 \times 10^{-7} \text{ V},$$

where 388 ohm is approximately the resistance of the sample and 10^5 is the V/A gain of the amplifier. The responsivity of the detector is thus,

$$R = (2.46 \times 10^{-7} \text{ V})/(703.86 \times 10^{-9} \text{ W}) = 0.35 \text{ V/W}.$$

D^* can also be estimated using the voltage noise density provided by the EG&G at 1KHz.

Therefore, the D^* of the multiquantum well detector is:

$$D^* = 3.82 \times 10^5 \text{ (cm-Hz}^{1/2}\text{)/W}.$$

This D^* number has to be corrected by considering the finite band width of the filter which is roughly $4.75 \text{ } \mu\text{m}$. The F.W.H.M of the quantum well detector measured on other samples by the FTIR is about 65 cm^{-1} or $0.65 \text{ } \mu\text{m}$ (Figs. 3.9a-9c). The corrected D^* is then calculated to be $2.79 \times 10^6 \text{ (cm-Hz}^{1/2}\text{)/W}$.

Finally, an attempt has been made to measure the spectral signal output at $10 \text{ } \mu\text{m}$ using Perkin-Elmer spectrometer but no signal was observed. The reason is expected to be the signal attenuation through the spectrometer slit. If one compares the performance of this detector with respect to the HgCdTe detector one can find that the responsivity of the quantum well detector has to be improved by three orders of magnitude.